Optical Trapping and Tracking of Nanoparticles Using Plasmonic Nanoapertures and Dielectric Nanoantennas

ZHE XU

(B.Sc. National University of Defense Technology, China)

(M.Sc. National University of Singapore, Singapore)

ORCID: 0000-0002-6688-5011

Submitted in total fulfilment of the requirements of the degree of

Doctor of Philosophy

March 2019

School of Physics

The University of Melbourne

Melbourne, Australia

Abstract

Optical Trapping and Tracking of Nanoparticles Using

Plasmonic Nanoapertures and Dielectric Nanoantennas

Author: ZHE XU

Supervisor: Professor Kenneth B. Crozier

The optical trapping and manipulation of nanoscale objects has found various potential applications in nanotechnology. To overcome the diffraction limit of conventional optical tweezers, several near-field optical trapping approaches have been employed, including plasmonic nanostructures. Optical trapping with plasmonics has proven to be an effective means for the contactless manipulation of nanometre-sized particles under low optical intensities with high precision. Various types of nanoparticles have been successfully trapped, including dielectric beads, gold nanoparticles, proteins, quantum dots and magnetic nanoparticles. However, the problem of Joule heating needs to be treated carefully, arising from the high absorption losses that occur for metals. The need for reduced heating has motivated interest into new nanostructure designs for near-field optical trapping. These designs aim to provide enhanced optical forces with small temperature increases.

This dissertation demonstrates the optical trapping and direct tracking of single nanoparticles using a plasmonic double nanohole aperture in a gold film and an all-silicon nanoantenna on a silicon substrate. For both structures, temperature rises that are modest have been predicted, especially for the all-silicon nanoantenna. Fluorescence microscopy is used to observe the optical trapping process during trap-and-release events and to track the position of, and fluorescent emission from, single trapped

nanoparticles as a function of time. The nanoparticles consist of fluorescent polystyrene nanospheres with diameters of 20 nm and 100 nm and streptavidin-coated CdSe/ZnS quantum dots. By analysing the Brownian motion of the trapped nanoparticles using fluorescence imaging, we present a quantitative analysis of the dynamics of the trapped nanoparticles, determining quantities such as the effective trapping stiffness. Comprehensive simulations are also performed to gain insight into the trapping process, including of the distributions of the near fields, temperature increase, fluid velocity, optical force and potential energy. Optical forces exerted on nanoparticles are determined using the rigorous Maxwell stress tensor method. Langevin equation simulations are performed to model the particle trajectories with Brownian motion. Other experiments reported include the two-photon excitation of fluorescence from trapped nanoparticles, the transport of nanoparticles relative to an array of nanoantennas via software-controlled movement of the chip, and the trapping and transport of multiple nanoparticles simultaneously.

Declaration

This is to certify that

(i) this thesis comprises only my original work towards the degree of Doctor of Philosophy except where indicated in the preface,

(ii) due acknowledgement has been made in the text to all other material used,

(iii) the thesis is less than 100,000 words in length, exclusive of tables, figures, bibliographies and appendices.

ZHE XU

March 2019

Preface

This dissertation is based on three journal publications. The dissertation author is the first author and main contributor of all publications. The average contribution of the dissertation author is about 90% or more in all publications. The dissertation author performed experiments, simulation, data analysis and wrote manuscripts for all publications.

Some of the figures used in this dissertation have been taken from other works and are not my own. In these instances, the appropriate reference has been inserted at the end of the figure caption to acknowledge the source and permission obtained from the publisher for reproduction.

Dr. Gediminas Gervinskas must be recognised for the fabrication of the double nanohole aperture samples that I designed at the Melbourne Centre for Nanofabrication (MCN).

Dr. Wuzhou Song performed silicon nanoantennas design and nanofabrication. Dr. Wuzhou Song designed and constructed the optical trapping experimental setup though I later made modifications to it.

Over the course of this work several publications and presentations were based on the work presented herein. They are listed below for reference.

REFEREED JOURNAL PUBLICATIONS

- **Xu, Z.**, & Crozier, K. B. (2019). All-dielectric nanotweezers for trapping and observation of a single quantum dot. ***Optics Express***, 27, 4034–4045.
- **Xu, Z.**, Song, W., & Crozier, K. B. (2018). Optical Trapping of Nanoparticles Using All-Silicon Nanoantennas. ***ACS Photonics***, 5, 4993–5001.
- **Xu, Z.**, Song, W., & Crozier, K. B. (2018). Direct particle tracking observation and Brownian dynamics simulations of a single nanoparticle optically trapped by a plasmonic nanoaperture. ***ACS Photonics***, 5, 2850–2859.

CONFERENCE PROCEEDINGS

- **Xu, Z.**, & Crozier, K. B. (2018, May). Controlled optical trapping and transport of a single 100 nm particle across an array of silicon nanoantennas. ***In CLEO: Science and Innovations*** (pp. SF3J-3). Optical Society of America. (**Oral** Presentation)
- **Xu, Z.**, Song, W., & Crozier, K. B. (2017, September). Direct observation of optical trapping of a single quantum dot with an all-silicon nanoantenna. ***In Frontiers in Optics*** (pp. FM3B-2). Optical Society of America. (**Oral** Presentation, *selected for promotion to the media*, news releases: ***Getting Hold of Quantum Dot Biosensors***, OSA, 22 August 2017)
- **Xu, Z.**, Song, W., & Crozier, K. B. (2017, May). Optical trapping using all-dielectric silicon nanoantennas with ultra-low heat generation. ***In CLEO: Science and Innovations*** (pp. SF1J-3). Optical Society of America. (**Oral** Presentation)
- **Xu, Z.**, Song, W., & Crozier, K. B. (2016, June). Optical tracking of a nanoparticle trapped by a double nanohole aperture. ***In CLEO:***

QELS_Fundamental Science (pp. FM2B-6). Optical Society of America. (**Oral** Presentation)

CONFERENCE PRESENTATIONS

- **Xu, Z.**, Song, W., & Crozier, K. B. (2018, 29 January–2 February). Dynamics of single 20 nm dielectric nanoparticles optically trapped by a double nanohole aperture. International Conference on Nanoscience and Nanotechnology (***ICONN 2018***), University of Wollongong, Wollongong, NSW, Australia. (**Oral** Presentation)
- **Xu, Z.**, Song, W., & Crozier, K. B. (2017, 10–13 December). Observing optical trapping and two-photon absorption of nanoparticles using all-dielectric nanoantennas. ***SPIE NanoPhotonics Australasia 2017*** (10456-35), Swinburne University of Technology, Melbourne, Australia. (**Oral** Presentation)

Acknowledgements

I *enjoy* doing my Ph.D. study at University of Melbourne because I like all my life here. I think I am a lucky guy to get some results and finish my dissertation. Without the encouragement and help from many friendly people during the last three and a half years, I cannot finish my study. I really thank all of them.

First and foremost, I am deeply grateful to my supervisor, Professor Kenneth B. Crozier, for his guidance and support throughout my Ph.D. study. He introduced me to this promising research field of nano-optics and granted me the intellectual freedom in my investigation of optical trapping. I thank him for his encouragement for my research project. He is a nice supervisor and I feel good to work with him. I thank him for his advice and feedback for improving my writing and presentation skills. I thank him for many opportunities he gave to me, such as Stanford University visiting experience (Professor Jennifer A. Dionne's group), attending international and domestic conferences, and good opportunities of meeting and talking with other professors. These are beneficial for my future professional career. I also thank him for agreeing with my study away plan for some personal difficulties.

I would like to express my sincere gratitude to my thesis advisory committee chair Professor Lloyd C.L. Hollenberg and my co-supervisor Professor Ann Roberts for coming together on short notice and providing constructive comments on my work. I enjoyed the opportunities I have had to talk with them and learn from them. I thank them for giving me the Skype meeting to complete my second-year progress review when I was in China. They have pioneered their respective research fields. I benefited a lot from their comments and suggestions.

I would wish to acknowledge all former and present group members in my group for their cooperation, assistance and valuable discussion: Dr. Wuzhou Song, Dr. Shi-Qiang Li, Dr. Vivek Raj Shrestha, Dr. Yang Gao, Dr. Jasper J. Cadusch, Dr. Dandan Wen, Dr. Jiajie Chen (visiting student), Olga Freydin, Ming Ye, Jiajun Meng, Benjamin Craig, Dounan Du and Nima Azar. In particular, I am grateful to Dr. Wuzhou Song, a professor now at Huazhong University of Science and Technology, for his help of my Ph.D. study. He taught me many experimental skills in our lab, fabricated the silicon nanoantenna samples and gave me many good suggestions to let me think about how to do my research and write my papers. It was an enjoyable experience to cooperate with him when he was a research fellow in our group. I am also grateful to Dr. Shi-Qiang Li for helping me with my COMSOL modelling and insightful discussions. I also thank Dr. Yang Gao for sharing his experience about scientific research and personal life. Outside of work, I enjoyed spending time with my friend Dr. Jiajie Chen in Melbourne during his six months visiting study.

I would like to thank all my friends in School of Physics: Dr. Evgeniy Panchenko, Dr. Stuart K. Earl, Dr. Jingchao Song, Lukas Wesemann, Kaijian Xing and Kalpana Singh. I wish to thank Lukas Wesemann especially for the lunch time and awesome office time we spent together.

I am sincerely grateful to Melbourne International Fee Remission Scholarship (MIFRS) and Melbourne International Research Scholarship (MIRS) programs for the significant role in helping me complete this dissertation. I thank the important financial supports.

Finally, I wish to express a truthful and heartfelt appreciation to my parents and my girlfriend Fangzhou Chen in China on this journey. My mother and my father love me

so much and give me many supports. They help me to solve many difficulty problems in my life. I really thank my girlfriend Fangzhou Chen for her love and company always, especially for the time we shared in Beijing. We have many good memories in Beijing, from winter to summer, from Forbidden City to China Zun.

Due to the limited space, I hereby express my deep appreciation to all people that I do not mention who have contributed to the efforts that made this dissertation possible.

Dedicated to

my parents and my girlfriend

Table of Contents

List of Contributions

The major contributions of this dissertation are summarized here.

(1) We perform direct particle tracking observation of a single polystyrene nanosphere with a diameter of 20 nm trapped by a double nanohole aperture in a gold film. To the best of our knowledge, our results represent the first time that the measured position distribution of a nanoparticle trapped by a plasmonic nanoaperture has been reported. Furthermore, we present Brownian dynamics simulations of particle trajectories, via Langevin equation with force terms that include stochastic Brownian force, gravity with buoyancy, the optical gradient force and Stokes drag. We also account for interactions of the nanoparticle with the nanoaperture morphology. To the best of our knowledge, the results represent the first time that simulated Brownian trajectories of particles in a near-field optical tweezer have been reported in the literature.

(2) We demonstrate the optical trapping and transport of nanoparticles using an all-silicon nanoantenna. All-silicon nanoantennas produce subwavelength field enhancements and enhanced optical forces with ultralow heat generation. We have successfully trapped polystyrene nanospheres with diameters of 20 nm and 100 nm. We use fluorescence microscopy to track the position and fluorescent emission of the trapped nanoparticles as a function of time. We show that multiple nanoparticles can be trapped simultaneously with a single nanoantenna. We also observe that the infrared continuous wave trapping laser produces fluorescent emission from trapped nanoparticles via two-photon excitation. To the best of our knowledge, our results represent the first experimental realization of optical trapping of nanoparticles using all-dielectric nanoantennas.

(3) We experimentally demonstrate, for the first time to the best of our knowledge, the direct observation of optical trapping and tracking of a single quantum dot in the vicinity of an all-dielectric (silicon) nanoantenna. In addition, we demonstrate that single trapped quantum dots can be excited by two-photon absorption from the continuous wave trapping laser, even for relatively low incident intensities.

List of Figures

Figure 1.16. (**a**) Schematic illustration of the induced currents in plasmonic and dielectric nanoparticles. (**b**) Schematic of the hotspot formation in plasmonic and dielectric nanodimers.

Figure 1.17. Scanning electron micrograph image (left) and numerical near-field distribution excited at resonance (right) of a Si nanodimer with a 20 nm gap. Scale bar: 100 nm.

Figure 1.18. (**a**) The three lowest electronic states for the case of $l = 0$. CdSe/ZnS core-shell QDs: CdSe core radius = 5 nm, ZnS shell thickness = 2 nm. Scale bar: 2 nm. (**b**) The corresponding energy diagram of QDs.

Figure 1.19. (**a**) Optical trapping (OT) with CW lasers. (**b**) OT of CdTe QDs with femtosecond lasers. (**c**) OT using Au nanodimers. (**d**) OT using DNH apertures. (**e**) OT of silica-coated QDs using silver bowtie apertures. (**f**) OT of QDs using silicon nitride photonic crystal resonators.

Figure 1.20. Schematic diagrams of degenerate (left) and non-degenerate (right) TPA.

Figure 2.1. (**a**) SEM image of DNH aperture with a 30 nm gap. Circular holes are denoted by orange dashed lines. (**b**) Photograph of Au films with DNH arrays. (**c**) Schematic layout of DNH arrays. (**d**) Optical microscope image of DNH arrays immersed in water. Scale bar: 10 μm.

Figure 2.2. (**a**) SEM image of all-Si nanoantenna with a 50 nm gap. (**b**) Photograph of a Si wafer with nanoantenna arrays. (**c**) Schematic layout of Si nanoantenna arrays in wafer (each blue square indicates an array with 25×25 nanoantennas). (**d**) Microscope image of Si nanoantenna array chip immersed in water. Scale bar: 10 μm.

Figure 2.3. Photograph of (**a**) a microfluidic chamber and (**b**) a Si chip sample package.

Figure 2.4. Photograph of the experimental setup showing two lasers and their optical paths.

Figure 6.1. Optical trapping of single proteins (Alexa Fluor 594-labeled streptavidin, Life Technologies) as sudden discrete jumps in fluorescence counts (I_0 = 12 mW/μm^2, 25×25 pixel cross section). Red arrow: trapping laser is switched off.

List of Abbreviations

OT	optical trapping
NS	nanosphere
NP	nanoparticle
PLOT	plasmonic optical trapping
Au	gold
Si	silicon
DNH	double nanohole
QD	quantum dot
FEM	finite element method
FIB	focused ion beam
EBL	electron beam lithography
CW	continuous wave
NA	numerical aperture
MST	Maxwell stress tensor
NT	nanotweezer
SP	surface plasmon
SPP	surface plasmon polariton
LSP	localized surface plasmon
SIBA	self-induced back-action
ETP	electrothermoplasmonic
PDE	partial differential equation
TPA	two-photon absorption
SEM	scanning electron micrograph
ICP-RIE	inductively coupled plasma reactive ion etching

PBS	phosphate-buffered saline
fps	frames per second
ITO	indium tin oxide
FWHM	full width at half maximum
AC	alternating current
DC	direct current
MD	magnetic dipole
EDL	electric double layer

CHAPTER 1

Introduction

1.1 Overview

It has been shown that optical trapping (OT) using plasmonic nanostructures allows the non-invasive manipulation of nanometre-sized particles, including dielectric nanospheres (NSs) and biological nanoparticles (NPs), to be performed at low optical intensities. The use of surface plasmons supported by metallic nanostructures leads to field distributions in which electric fields are strongly enhanced and are confined on deeply subwavelength scales. This results in enhanced optical forces and associated trapping potential energy. Plasmonic optical trapping (PLOT) has two main advantages over conventional optical tweezers. First, it breaks the diffraction limit, allowing trapped NPs to be localized much more tightly. Second, for the same input laser power, the trapping potential can be much larger for PLOT, enabling the strong Brownian motion of NPs in a fluid to be tamed. Although various geometries have been investigated during recent years, the problem of Joule heating from the high dissipative losses occurring in metals limits practical applications and thus must be treated carefully, especially for the optical trapping and sensing of biological specimens. This issue has been addressed by designing the plasmonic nanostructure to exhibit good thermal conductivity (e.g., to conduct the heat into the substrate) and by tailoring the plasmonic resonances appropriately. PLOT has thus been demonstrated for the optical trapping and manipulation of small hard particles (such as polystyrene and silica beads, gold NPs, nanodiamonds and semiconductor NPs) and biomolecules (such as proteins, viruses and DNA).

It has been reported nanoapertures in metallic films, such as gold (Au), enable the trapping of single proteins and quantum dots at low optical powers. During the past few years, different nanoaperture geometries have been introduced. One of these is the double nanohole aperture, with which it has been reported that the trapping of single bovine serum albumin molecules has been achieved. In the nanoaperture approach, the metallic film itself can serve as a good heat sink because of its good thermal conductivity, thereby reducing the temperature rise by conducting away the heat. In previous reports of nanoaperture tweezers, trapping dynamics were demonstrated via monitoring the optical transmission through the nanoaperture as a function of time, where step-like rises in transmission indicate the trapping of individual NPs. Nanoaperture tweezers present many opportunities for the field of nanoscience, including the measurement of the properties of NPs on the single particle level and the measurement of dynamics in real-time, e.g., of protein binding kinetics. Furthermore, nanoaperture tweezers are well-suited to integration, for example into microfluidic systems or at the ends of optical fibres.

While the heat sink approach can greatly reduce temperature, increases occurring with plasmon excitation, it does not eliminate them. For some applications, further reductions in heating are needed. This suggests a non-plasmonic approach. One candidate is that of the all-dielectric nanoantenna. These structures consist of low-loss high refractive index dielectrics, such as silicon (Si) or germanium. The nanodimer configuration is particularly compelling for optical nanotweezers. In this approach, two dielectric nanoparticles are separated by a small gap. Illumination of the nanodimer with light polarised across the gap results in a strong field enhancement in the gap. Importantly, since dielectric materials exhibit low absorption losses at optical frequencies, heat generation by the nanoantenna is weak, thereby producing very low

light-into-heat conversion and temperature rise. All-dielectric nanoantennas have been employed in a wide range of applications, including for example surface-enhanced spectroscopy (fluorescence and Raman scattering), biological sensing, and nonlinear optics.

This dissertation focuses on the optical trapping and direct tracking of a single nanoparticle using two nanostructures (or nanotweezers) that exhibit low heat generation. The first is a double nanohole (DNH) aperture in a gold film. The second is an all-silicon nanoantenna on a silicon substrate. Two kinds of nanoparticles have been optically trapped, namely fluorescent polystyrene nanospheres (20 nm and 100 nm in diameter) and streptavidin-coated CdSe/ZnS quantum dots (QDs). Using fluorescence microscopy, the trapping-and-release processes are observed directly, and the trapped nanoparticles' location and fluorescence light emission have been tracked as a function of time. The direct imaging observation yields additional information not available in the previous method employed with nanoapertures, that is, monitoring transmission as a function of time. Additionally, we perform the finite element method (FEM; COMSOL Multiphysics) numerical simulations to elucidate the trapping process, including near-field distributions, optical forces, potential energy, thermal effects, and Brownian dynamics simulations of trapped particles trajectories. This dissertation also demonstrates the two-photon excitation of nanoparticle fluorescence, the transport of nanoparticles relative to the array of nanoantennas, and the simultaneous trapping of multiple nanoparticles.

This dissertation is organized as follows:

Chapter 1 reviews key elements of the physics of the trapping process. This Chapter also provides a literature review of the relevant background, including optical trapping

and optical forces, optical heating, previous work on optical trapping with plasmonic nanoapertures, all-dielectric nanoantennas, optical trapping of quantum dots, and two-photon absorption. The theoretical framework for analysis is highlighted. The motivation for the development of new approaches to near-field optical trapping methods is described, with particular emphasis on the issue of heating. This is of particular importance due to the fact that one potential application of near-field optical tweezers is for the trapping of single biological molecules for biosensing.

Chapter 2 presents the details of the nanofabrication, numerical simulation, and experimental methods employed in this dissertation. In this work, the DNH aperture is milled into a 100 nm thick Au film using a focused ion beam (FIB) technique, and the Si nanoantennas are fabricated by electron beam lithography (EBL) and reactive ion etching on a Si wafer. Three-dimensional simulations are performed by the FEM (COMSOL Multiphysics). The numerical simulations include near-field distributions, optical forces and potential energy, photothermal effects, and nanoparticle Brownian dynamics. The most important parameters, optical forces, are determined using the rigorous Maxwell stress tensor method. The photothermal effects correspond with the combination of the temperature rise in nanostructures and the surrounding water, and the heat induced water flow. Experimental methods are also introduced, including the microfluidic chamber preparation and the optical trapping experimental setup.

Chapter 3 fully reproduces my first refereed journal publication in my Ph.D. study entitled "*Direct Particle Tracking Observation and Brownian Dynamics Simulations of a Single Nanoparticle Optically Trapped by a Plasmonic Nanoaperture*". This chapter is originally published in ***ACS Photonics***. My experiments include the direct particle tracking observation on a single nanoparticle optically trapped by a DNH aperture. To the best of our knowledge, these results represent the first time that the position

distribution of a single NP trapped by a nanoaperture has been reported experimentally. My modelling of nanoparticle trapping dynamics with Brownian motion provides further insights into the trapping process by providing information that complements that provided by our experiments.

Chapter 4 reports the first demonstration of the optical trapping, direct tracking and transport of single and multiple dielectric nanospheres with all-dielectric (silicon) nanoantennas. This work is originally published in ***ACS Photonics*** entitled "*Optical Trapping of Nanoparticles Using All-Silicon Nanoantennas*". Our results demonstrate that Si nanoantenna optical tweezers permit single NPs in solution to be immobilized on-demand, enabling them to be observed for extended periods and then released by switching off the trapping beam. Our Si nanoantenna can reconcile the conflicts between near-field enhancements and deleterious thermal effects that can occur for optical trapping with plasmonic nanoantennas.

Chapter 5 focuses on the direct observation of optical trapping of a single streptavidin-coated CdSe/ZnS quantum dot in a microfluidic chamber by our all-Si nanoantennas. This chapter is originally published in ***Optics Express*** entitled "*All-dielectric nanotweezers for trapping and observation of a single quantum dot*". To the best of our knowledge, our results show the first demonstration of optical trapping of quantum dots by optical forces using all-dielectric nanotweezers. Furthermore, we observe the clear fluorescence blinking behaviour from optically trapped QDs. We do not observe any photothermal effects of the QD emission, including quenching and bleaching.

The last chapter of this dissertation, Chapter 6, summarizes the important findings in this dissertation as well as making the suggestions for some future research directions.

1.2 Optical trapping and optical forces

As predicted by Maxwell's equations, light (or electromagnetic) fields have linear and angular momentum and thus can generate optical forces and torques on objects via momentum transfer. Optical trapping, the ability to hold and manipulate small objects with light, has found widespread applications in the physical and life sciences. The existence of forces exerted by light was first demonstrated in 1901.[1] The trapping of micrometre-sized particles with light was reported in 1970 by A. Ashkin.[2] It was demonstrated later that a single tightly focused laser beam, now termed as ***optical tweezers***,[3] can be utilized to trap microscopic particles near the focus of a laser beam in three dimensions, as illustrated in Figure 1.1. In 2018, Arthur Ashkin was awarded the Nobel Prize in Physics for this development. The basic experimental setup is simple. A single continuous wave (CW) laser beam is introduced into an optical microscope and focused by an objective lens with high numerical aperture (NA) to a diffraction-limited spot. Since then, optical tweezers are successfully used to trap and manipulate a wide range of small particles, ranging from dielectric and metallic particles, to atoms, molecules, viruses and living cells.[4-8]

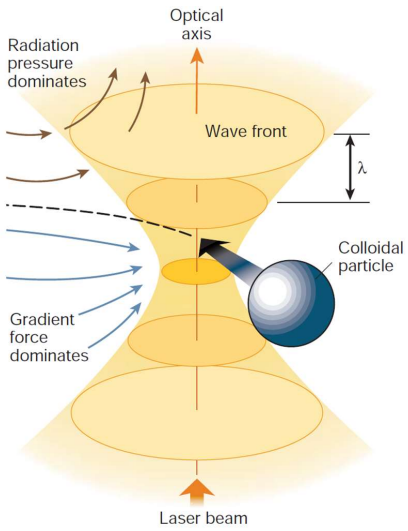

Figure 1.1. Schematic of a single beam optical tweezers (reproduced from ref 7).

Forces in the dipole approximation: Conventional single beam optical tweezers can be well described by the dipole approximation,[9] when the diameter of the trapped particle is much smaller than the wavelength of the trapping laser (Rayleigh particle). In this situation, the Rayleigh scattering conditions are satisfied, and the particle is approximated by an electric point dipole. In conventional optical tweezers, other than acting as an electric point dipole, the presence of the particle does not change the light fields. Two types of *time-averaged* optical forces can be considered.[10, 11]

The first type of the force, the *gradient force* due to dielectrophoresis, is proportional to the gradient of the square of the electric field, and thus pulls the particle towards the maximum light intensity regions. This term is usually called the optical trapping force and is a conservative force.

$$\left\langle \vec{F}_{grad} \right\rangle = \frac{1}{4}\mathrm{Re}(\alpha_p)\nabla\left|\vec{E}\right|^2 \tag{1.1}$$

where α_p is the particle polarizability. It can be seen that the gradient force depends on the real part of the particle polarizability. For a small dielectric particle, the Clausius–Mossotti relation is traditionally used to describe the polarizability and then modified to include radiation damping, thereby yielding:

$$\alpha_p = \frac{\alpha_0}{1 - i\alpha_0 k_0^3 / 6\pi\varepsilon_0} \tag{1.2}$$

where k_0 is the free-space wavenumber of the trapping laser, and

$$\alpha_0 = 4\pi r_p^3 \varepsilon_0 n_f^2 \frac{n_p^2 - n_f^2}{n_p^2 + 2n_f^2} \tag{1.3}$$

To a first order approximation, $\alpha_p \approx \alpha_0$ and we thus have:[11]

$$\left\langle \vec{F}_{grad} \right\rangle = \pi r_p^3 \varepsilon_0 n_f^2 \frac{n_p^2 - n_f^2}{n_p^2 + 2n_f^2} \nabla\left|\vec{E}\right|^2 \tag{1.4}$$

where r_p is the particle radius, ε_0 is the vacuum permittivity, n_f is the refractive index of the surrounding medium and n_p is the refractive index of the particle.

The second type of the force, the non-conservative *scattering force*, proportional to the total cross-section of the particle, can be described by two different contributions: a *radiation pressure force* that acts to push the particle in the direction of the Poynting vector, and a *spin curl force* associated with the nonuniform distribution of the spin density of the light fields. Until recently, the latter was frequently neglected, despite the fact that it can be important for the tightly focused laser beams used in optical tweezers. The scattering force is given by:[11]

$$\left\langle \vec{F}_{scat} \right\rangle = \frac{\sigma(\alpha_p)}{2c}\mathrm{Re}(\vec{E}\times\vec{H}^*) + \sigma(\alpha_p)c\nabla\times(\frac{\varepsilon_0}{4\omega i}\vec{E}\times\vec{E}^*) \tag{1.5}$$

The total cross-section of the particle σ is the sum of the absorption (σ_{abs}) and scattering (σ_{sc}) cross-sections.

$$\sigma(\alpha_p) = \sigma_{abs}(\alpha_p) + \sigma_{sc}(\alpha_p) \tag{1.6}$$

$$\sigma_{abs}(\alpha_p) = \frac{k}{\varepsilon_0}\mathrm{Im}(\alpha_p) \tag{1.7}$$

$$\sigma_{sc}(\alpha_p) = \frac{k^4}{6\pi\varepsilon_0^2}\left|\alpha_p\right|^2 \tag{1.8}$$

where k is the wavenumber of the trapping laser in the surrounding medium.

For a plane wave with intensity I_0 traveling along the direction of $\vec{s}$, the spin curl force is zero. For a small dipolar dielectric particle, $\sigma_{abs} = 0$ and

$$\sigma_{sc} = \frac{128\pi^5 r_p^6}{3\lambda^4}(\frac{n_p^2 - n_f^2}{n_p^2 + 2n_f^2})^2 \tag{1.9}$$

and the scattering force is written as:[11]

$$\left\langle \vec{F}_{scat} \right\rangle = \frac{\sigma_{sc}}{c} I_0 \vec{s} = \frac{128\pi^5 r_p^6}{3\lambda^4 c} \left(\frac{n_p^2 - n_f^2}{n_p^2 + 2n_f^2}\right)^2 I_0 \vec{s} \tag{1.10}$$

where c is the light speed in vacuum, λ is the trapping laser free-space wavelength and $\vec{s}$ is the unit propagation vector. For stable trapping, the gradient force must exceed the scattering force.

Forces beyond the dipole approximation: When a particle cannot be approximated as a point dipole, the optical force exerted on it can be determined by the Maxwell stress tensor (MST) method.[9, 12] This is a rigorous way of computing optical forces acting on an arbitrary particle of a given size, shape and refractive index, and is based on the conservation law for the linear momentum. The total *time-averaged* electromagnetic force (i.e., optical force) exerted on a particle interacting with optical fields is given by:[9]

$$\left\langle \vec{F} \right\rangle = \int_{\partial V} \left\langle \vec{\vec{T}}(\vec{r},t) \right\rangle \bullet \vec{n}(\vec{r}) da \tag{1.11}$$

where $\vec{\vec{T}}(\vec{r},t)$ is the Maxwell stress tensor, $\vec{n}(\vec{r})$ is the unit vector perpendicular to particle surface ∂V, and da is an infinitesimal surface element. In Cartesian components, the MST reads as:[9]

$$\vec{\vec{T}} = [\varepsilon_e \vec{E}\vec{E} + \mu_e \vec{H}\vec{H} - \frac{1}{2}(\varepsilon_e E^2 + \mu_e H^2)\vec{\vec{I}}] = \tag{1.12}$$

$$\begin{bmatrix} \varepsilon_e(E_x^2 - E^2/2) + \mu_e(H_x^2 - H^2/2) & \varepsilon_e E_x E_y + \mu_e H_x H_y & \varepsilon_e E_x E_z + \mu_e H_x H_z \\ \varepsilon_e E_x E_y + \mu_e H_x H_y & \varepsilon_e(E_y^2 - E^2/2) + \mu_e(H_y^2 - H^2/2) & \varepsilon_e E_y E_z + \mu_e H_y H_z \\ \varepsilon_e E_x E_z + \mu_e H_x H_z & \varepsilon_e E_y E_z + \mu_e H_y H_z & \varepsilon_e(E_z^2 - E^2/2) + \mu_e(H_z^2 - H^2/2) \end{bmatrix}$$

where $\vec{n}(\vec{r}) = \begin{bmatrix} n_x \\ n_y \\ n_z \end{bmatrix}$, $\vec{E} = \begin{bmatrix} E_x \\ E_y \\ E_z \end{bmatrix}$, $\vec{H} = \begin{bmatrix} H_x \\ H_y \\ H_z \end{bmatrix}$, $\varepsilon_e = \varepsilon_0 \varepsilon_r$, $\mu_e = \mu_0 \mu_r$ are the permittivity and permeability of the surrounding medium respectively, ε_0 is the vacuum permittivity, μ_0 is the vacuum permeability, ε_r is the relative permittivity and μ_r is the relative permeability of the surrounding medium (e.g., water). The force is entirely determined by the electric and magnetic fields on the particle surface ∂V. Here the fields used in the MST are the self-consistent fields, which means that they are a superposition of the incident and the scattered fields (Figure 1.2). Therefore, the problem of force calculation first reduces to solving the field scattering problem.

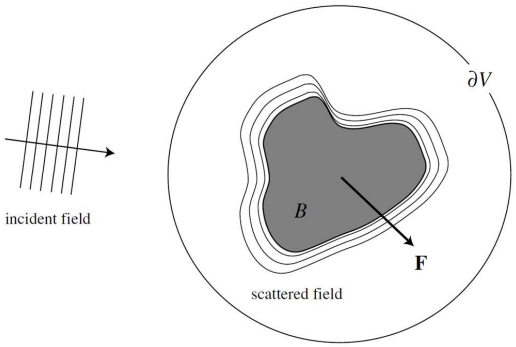

Figure 1.2. MST forces on an object *B* are determined on the object surface ∂V (reproduced from ref 9).

Electromagnetic fields also carry angular momentums and thus can exert mechanical torques on objects. The *time-averaged* torque can be represented as:[9]

$$\left\langle \vec{N} \right\rangle = -\int_{\partial V} \left\langle \vec{\vec{T}}(\vec{r},t) \times \vec{r} \right\rangle \bullet \vec{n}(\vec{r}) da \tag{1.13}$$

Trapping potential energy: Although the optical forces on particles are not strictly conservative, via confining the motion of the particle in one dimension, such as *x*-axis, an *effective* trapping potential energy can be defined as:

$$U(x_0) = -\int_{\infty}^{x_0} \left\langle F_x(x) \right\rangle \bullet dx \tag{1.14}$$

Here when x tends to infinity, U is set to be zero.

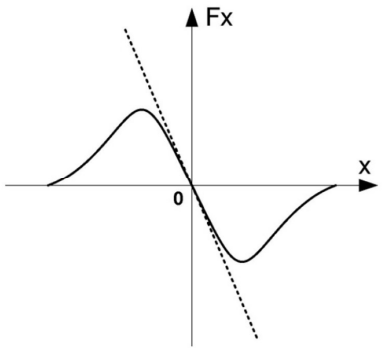

Figure 1.3. Definition of the trapping stiffness from the linear slope.

Trapping stiffness (for small displacements): An important parameter of an optical tweezer is its trapping stiffness. For example, in one dimension, for small displacements x from the equilibrium position (Figure 1.3), the restoring optical force can be approximated to be linearly dependent on x:[9]

$$\langle F_x \rangle = -k_x x \tag{1.15}$$

where k_x is the trapping stiffness along x-direction. A larger stiffness means that the optical force exhibits stronger localization. A consequence of this assumption of the linear dependence of the restoring force is that the trapping potential energy is then approximated by a harmonic function.

In our experiments, we use fluorescence microscopy to track the position of a single trapped NP as a function of time. A camera is used to record the trapping process. Like any camera, it has a finite integration time. Rather than representing instantaneous positions x, the measured positions x_m are the average values of the instantaneous (i.e., true) positions x during a finite integration time (i.e., exposure time) of the camera. We thus use the calibration method introduced by Wong and Halvorsen that accounts for the

video-image motion blur over the camera integration time.[13] Here the particle is assumed to be in an ideal harmonic trapping potential.

$$U(x) = \frac{1}{2} k_x x^2 \tag{1.16}$$

In equilibrium, the true position variance var(x) is expressed as:

$$\mathrm{var}(x) = \frac{k_B T}{k_x} \tag{1.17}$$

and the measured position variance var(x_m) reads as:[13]

$$\mathrm{var}(x_m) = \mathrm{var}(x) S(\alpha) \tag{1.18}$$

where k_B is the Boltzmann constant, T is the temperature and $S(\alpha)$ is the motion blur correction function. The latter is given by:[13]

$$S(\alpha) = \frac{2}{\alpha} - \frac{2}{\alpha^2}(1 - \exp(-\alpha)) \tag{1.19}$$

and

$$\alpha = \frac{W k_x}{6\pi\mu r_p} \tag{1.20}$$

where W is the integration time of the camera, μ is the viscosity of water and r_p is the particle radius. In this way, the "effective" trapping stiffness with motion blur correction can be found by solving eqs 1.17–1.20. Note that we refer to the trapping stiffness as being "effective" to indicate the fact that in our near-field optical tweezers (i.e., DNH and all-Si nanoantenna) the restoring force is not a linear function of the particle displacement (from trap centre). The "effective" trapping stiffness can be thought of as the stiffness that would be possessed by an ideal harmonic trap that produces the same localization (position variance) as our near-field optical tweezers.

1.3 Plasmonic nanoapertures trapping

The trapping and manipulation of micrometre-sized particles and living cells using conventional optical tweezers is well-established. Conventional optical tweezers, however, face challenges for the stable trapping of nanoparticles. NPs are particles with diameters between ~ 1 and 100 nanometres (nm). They include a wide range of interesting structures for nanomaterials-based applications,[11, 14] such as quantum dots, carbon nanotubes and semiconductor nanowires (Figure 1.4). The optical trapping of NPs remains a big challenge for the following two reasons. First, conventional optical tweezers are subject to the diffraction limit, which places a lower bound on the size of focused spot. Second, because the gradient force is roughly proportional to the particle volume (see eq 1.4), NPs experience smaller trapping forces. As a result, the incident optical power must be increased to maintain the trap stability, i.e., to overcome strong Brownian motion. This can lead to undesired photothermal effects. Although some particles can support OT at high power levels, it is not always appropriate for many objects, especially for biomolecules.

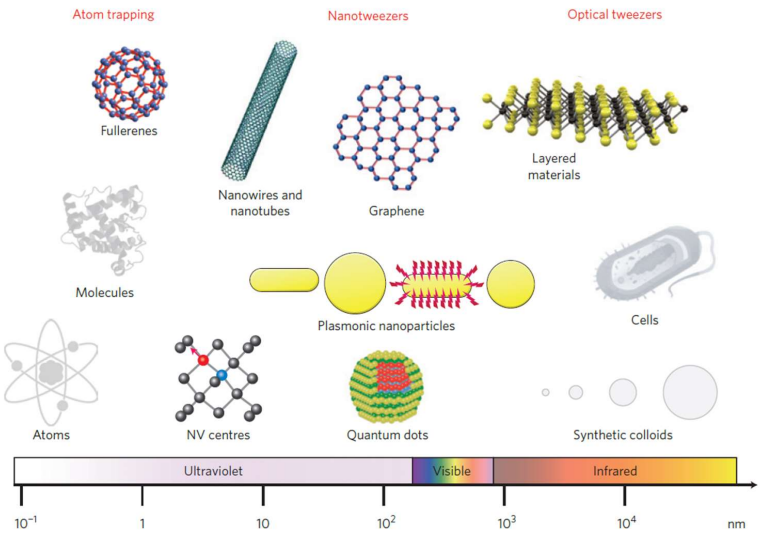

Figure 1.4. The particle size range in OT (reproduced from ref 14).

To overcome these limitations, the use of near-field nanotweezers (NTs) based on plasmonics[15-19] and other techniques, such as sub-wavelength slot waveguides,[20] ring resonators,[21] and photonic crystal resonators,[22] has attracted keen interest (Figure 1.5). Due to subwavelength field confinement and enhancement, plasmonic nanotweezers have shown promise for the optical trapping of NPs, and reports have been made of single molecule trapping.[23] In plasmonic nanotweezers, such as nanoantennas and nanoapertures, surface plasmon resonances are used to concentrate light into the nanoscale. In summary, plasmonic nanotweezers have three key advantages over conventional optical tweezers: (1) the light intensity needed for stable trapping is decreased because of the plasmonic field enhancement; (2) the motion of the trapped NP is localized to a narrower potential well because the diffraction limit is broken; and (3) plasmonic nanotweezers are suitable for integration with other techniques (such as Raman spectroscopy) and other structures (such as optical fibres and microfluidic devices).

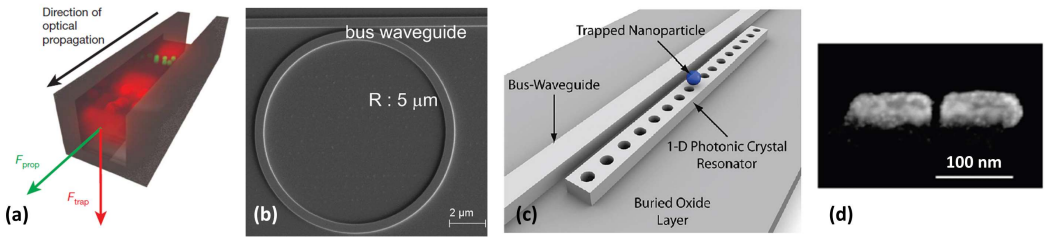

Figure 1.5. Optical trapping with near-field nanotweezers. (a) Si slot waveguides (reproduced from ref 20). (b) Si microring resonators (reproduced from ref 21). (c) Si photonic crystal resonators (reproduced from ref 22). (d) Au dipole nanoantennas (reproduced from ref 17).

Some of the early works in plasmonic nanotweezers are as follows. In 2004, Kwak et al. first reported the OT of 200 nm (in diameter) fluorescent beads using nanoapertures in an Au film.[24] In 2008, Grigorenko et al. reported the OT of polystyrene beads (200 nm diameter) using pairs of Au nanopillars (Figure 1.6).[15] Due to the local

field enhancement, plasmonic double nanopillars can reduce the trapping volume so it is below that given by the diffraction limit, thereby quenching Brownian motion of the optically trapped particles by nearly an order of magnitude as compared with conventional optical tweezers working under the same conditions.[15] In 2009, Quidant's group reported the OT of living *Escherichia coli* bacteria using Au nanoantennas on a glass substrate.[25] Although *E. coli* bacteria can be trapped with conventional optical tweezers, the trapping laser intensities are quite high, and the photodamage is readily observed.[25] In 2010, Zhang et al. reported the OT and sensing of Au NPs (10 nm diameter) using plasmonic Au dipole nanoantennas.[17]

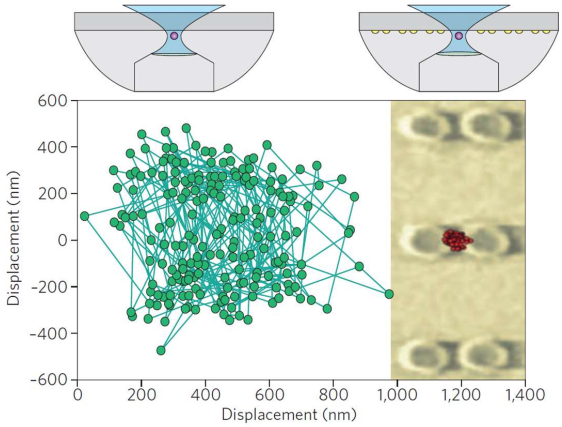

Figure 1.6. Optical trapping and position distributions of 200 nm polystyrene beads using conventional optical tweezers (left) and plasmonic double nanopillars (right) (reproduced from ref 15).

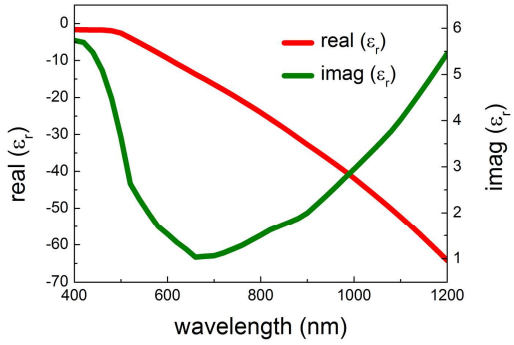

Figure 1.7. The real and imaginary part of the complex relative permittivity of Au (Johnson and Christy data).[26]

Surface plasmons: The ability of plasmonic tweezers to yield field distributions in which electric fields are enhanced (compared to incident field) and confined on a subwavelength scale originates from the excitation of the collective oscillations of free electrons in the metal. These are termed surface plasmons (SPs).[9, 27] The existence of SPs was first predicted in 1957 by R. Ritchie.[28] SPs are supported by metals (e.g., Au, Figure 1.7) and other materials with high free charge densities such as doped semiconductors. The optical properties of metals can be understood classically by the Drude–Sommerfeld model that considers the free electron gas.[9, 29] In response to an applied electric field, the free electrons experience a force and undergo an oscillation described by the following equation of motion:[9]

$$m_e \frac{\partial^2 \vec{r}}{\partial t^2} + m_e \Gamma \frac{\partial \vec{r}}{\partial t} = e\vec{E}_0 e^{-i\omega t} \tag{1.21}$$

where m_e and e are the effective mass and charge of each free electron, Γ is the collisional damping frequency, and $\vec{E}_0$ and ω are the amplitude and angular frequency of the applied electric field. Solving the equation of motion gives the dielectric constant (also known as the relative permittivity):[9]

$$\varepsilon_{Drude}(\omega) = 1 - \frac{\omega_p^2}{\omega^2 + i\Gamma\omega} \tag{1.22}$$

Here $\omega_p = \sqrt{\frac{ne^2}{m_e \varepsilon_0}}$ is the volume plasma frequency, where n is the number density of the electrons. Equation 1.22 can be divided into real and imaginary parts:[9]

$$\varepsilon_{Drude}(\omega) = 1 - \frac{\omega_p^2}{\omega^2 + \Gamma^2} + i\frac{\Gamma\omega_p^2}{\omega(\omega^2 + \Gamma^2)} \tag{1.23}$$

We note that the dielectric constant is negative when $\omega < \omega_p$. This negative dielectric constant is of key importance, being responsible for the surface plasmon resonance phenomena. Two different forms of the SPs are known, depending on the

geometry of the metal (Figure 1.8). They are termed surface plasmon polaritons (SPPs) and localized surface plasmons (LSPs).

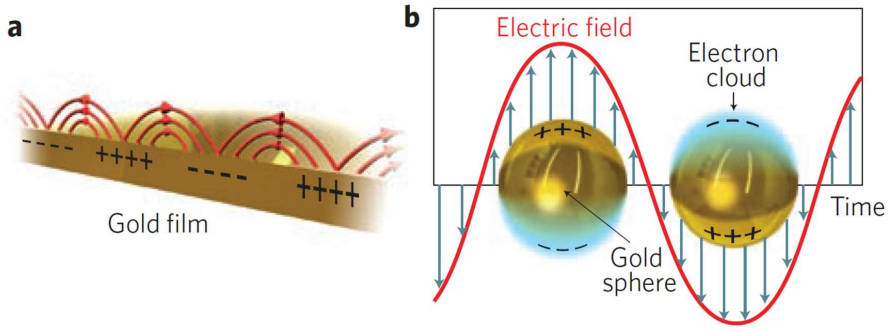

Figure 1.8. Schematic illustration of (a) SPPs and (b) LSPs (reproduced from ref 18).

SPPs refer to propagating electromagnetic surface waves that can exist at flat metal-dielectric or metal-air interfaces (Figure 1.8a). They are also referred to as propagating surface plasmons. SPPs involve both the motion of charges in the metal (surface plasmons) and electromagnetic waves in the dielectric or air (polariton).[30] SPPs are propagating modes. They lose energy to the metal due to absorption and the SPP intensity decays exponentially as a function of distance (into the metal and into the dielectric or air) from the interface.

LSPs generally refer to surface plasmons excited in noble metal nanoparticles (e.g., plasmonic nanoantennas) or at the ends of sharp metallic tips with dimensions comparable to or smaller than the excitation wavelength.[31] In LSPs, the time-dependent light fields exert a force on the electrons gas in the conduction band of the metal and drive the electrons to oscillate collectively. For a specific excitation frequency, this induced oscillatory is in resonance with the applied fields, leading to an increased oscillation amplitude. This is also referred to a localized surface plasmon resonance mode. LSPs have two important features: the electromagnetic fields around the particle

surface are highly enhanced, and the absorption cross-section of the particle reaches a maximum at the resonant frequency.

To illustrate the concept of LSPs, we present some example FEM (COMSOL) simulations. The first is of a single Au nanosphere with a diameter of 60 nm illuminated by a plane wave at a wavelength of 522 nm (Figure 1.9a). The second is of a pair of Au nanospheres with diameters of 60 nm separated by a gap of 5 nm. The incident light for the nanosphere pair is a plane wave at a wavelength of 550 nm (Figure 1.9b). Both are in air (n_{air} = 1) and the illuminating plane wave is x-polarized and propagates in the $+z$ direction. Coupling between the NSs red-shifts the resonant wavelength from 522 nm (for the single NS) to 550 nm (for the pair of NSs). It can be seen from Figure 1.9 that the electric field enhancement ($|E|/|E_0|$) is larger for the pair of nanospheres due the presence of the small gap. Here $|E_0|$ is the amplitude of the incident plane wave.

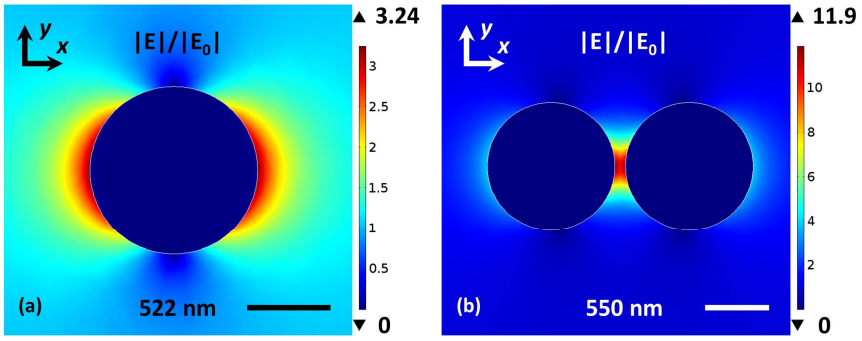

Figure 1.9. Simulated electric field enhancement for (a) a single Au NS and (b) a pair of Au NSs with a 5 nm gap. Scale bar: 30 nm.

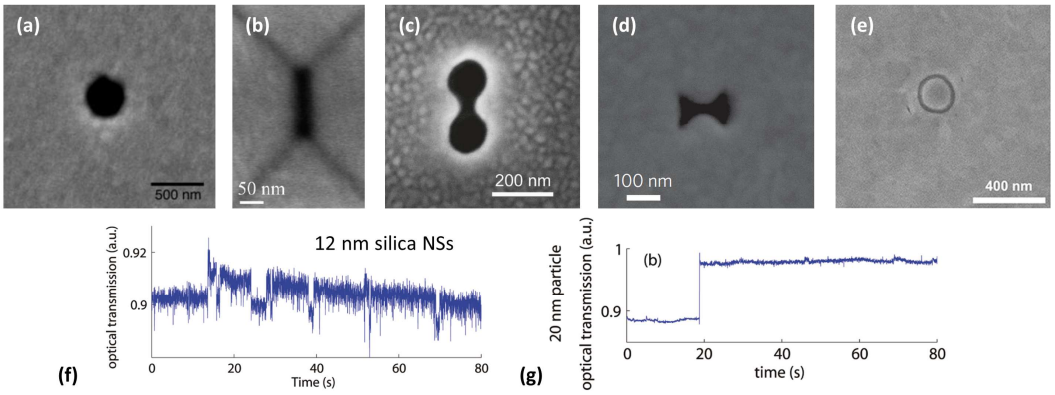

Figure 1.10. Nanoaperture trapping geometries: (a) circular apertures (reproduced from ref 16); (b) rectangular apertures (reproduced from ref 32); (c) DNH apertures (reproduced from ref 33); (d) bowtie apertures (reproduced from ref 34); (e) coaxial apertures (reproduced from ref 35). Optical trapping of (f) 12 nm silica NSs and (g) 20 nm polystyrene NSs using DNH apertures (reproduced from ref 33).

Optical trapping using nanoapertures: Among the various metallic nanostructures that have been employed for PLOT, plasmonic nanoapertures in thin metallic films have generated a considerable amount of interest.[18, 36] Plasmonic nanoapertures allow the OT of NPs at much lower laser intensities than conventional optical tweezers. Followed by the first demonstration of the OT of 200 nm fluorescent beads in water using a nanoaperture in a gold film by Kwak et al. in 2004,[24] a large number of theoretical and experimental works have been done with different nanoaperture geometries (Figure 1.10), such as circular apertures,[16] rectangular apertures,[32] double nanohole (DNH) apertures,[33] bowtie apertures,[34] and coaxial apertures.[35] Some notable trapping works include the demonstration of the optical trapping of dielectric NPs,[33] the trapping and manipulation of NPs using nanoapertures at the ends of optical fibres,[34] the reported monitoring of protein folding,[36] the trapping of single proteins[23] and colloidal QDs,[37] the characterization of magnetic NPs,[38] and fundamental investigations on the trapping performance.[39] Interestingly, nanoapertures exhibit the "self-induced back-action" (SIBA) effects, where the trapped NP plays an active dynamic role in enhancing optical forces to help the trapping.[16] In these previous

publications, the trapping process was monitored by measuring the optical transmission (of the trapping beam or of the fluorescent emission from trapped particles) through the nanoaperture as a function of time, with step-like increases in transmission showing the OT of NPs. While useful, plots of transmission versus time only provide limited information on the trapping process. Prior to this dissertation, the direct observation (i.e., trajectories) of NPs trapped by plasmonic nanoapertures had not been demonstrated. In this dissertation, the nanoapertures considered are DNH structures. These have favourable attributes that include: (1) the small gap between two circular holes provides a high local fields enhancement; (2) the metal film helps reduce heating effects; and (3) the structure is relatively easy to fabricate compared to nanoantennas or bowtie nanoapertures. Since only the gap size is comparable to the particle diameter (i.e., 20 nm in my experiments), the DNH gap size is set to be ~ 30 nm after considering the fabrication tolerance.[33]

1.4 Optical heating

The illumination of plasmonic nanostructures with light leads to Joule heating due to absorption.[40, 41] This generally complicates the trapping process because it can result in convection currents, water boiling (in which the trapping is performed) and to damage of the sample at high laser intensities.[42, 43] Examples of the approaches that have been explored to mitigate this include the introduction of a high thermal conductivity substrate (i.e., heat sink design)[44] or by off-resonance illumination to minimize the light absorption.[45] For example, Wang et al. illustrated that heating can be decreased about 100-fold by introducing a gold-copper-silicon heat sink design with plasmonic nanoantennas (Figure 1.11). In optical trapping with plasmonic nanoapertures, we demonstrate (in Chapter 3) that the metallic film itself works as a good heat sink and

helps diminish local heating.[46] On the other hand, the heating that accompany plasmon resonance can be turned into an advantage. Examples include plasmonic photothermal therapies,[47] the optical trapping and versatile manipulation of NPs and biological cells using thermophoretic nanotweezers,[48] and the long-range and rapid transport of NPs by the electrothermoplasmonic (ETP) flow.[49] However, in many OT applications, heating is detrimental as it can damage both the object being trapped and plasmonic nanotweezer structure, as well as lead to the other issues mentioned above.

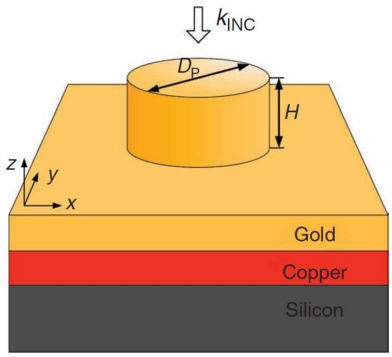

Figure 1.11. Plasmonic nanopillars with an integrated heat sink (D_P = 280 nm, H = 130 nm, reproduced from ref 44).

We next consider the issue of heating in greater detail. As discussed, SP excitation can be accompanied by strong absorption, leading to local temperature increases. This in turn results in a large temperature gradient, causing the thermal convection and thermophoresis[19, 42, 43] or even boiling of the water. Thermal convection, also commonly known as free convection or natural convection of a fluid (usually water), takes place through the net displacement of the fluid that is caused by buoyancy because the fluid density varies with the temperature. Here we consider plasmonic nanotweezers. In optical trapping experiments, since there have no any external sources (like a pump, fan, etc.), the convection is only natural. The water that surrounds a plasmonic nanotweezer structure is heated and thus flows upward due to buoyancy. Then this hot water cools

down via heat (or energy) exchange with the non-heated microfluidic chamber walls, and finally flows back to plasmonic nanotweezer structure, thus establishing a convective flow pattern (Figure 1.12).[41] Here the hotter volume transfers heat towards the cooler volume of the water. Because the induced convection water flow exerts Stokes drag forces on particles, it destabilizes the OT process.[43] Thermophoresis (also known as the Soret effect) moves particles along temperature gradients of the background fluid.[50-52] The direction in which the particles move by thermophoresis depends on the nanoparticle material. Polystyrene NSs, for example, move from hotter to colder areas.[19, 53] But this effect can be reversed for very small particles (e.g., molecules) and at low temperatures (e.g., a few degrees Celsius).[42] The thermophoretic force is defined as:[41]

$$\vec{F}_{tp} = \frac{6\pi d_p \mu^2 C_s (k_f / k_p) \nabla T}{\rho(2(k_f / k_p)+1)T} \tag{1.24}$$

where d_p is the particle diameter, μ is the fluid viscosity, k_f is the thermal conductivity of the fluid, k_p is the thermal conductivity of the particle, T is the fluid temperature, ρ is the fluid density, and C_s is a constant equal to 1.17.

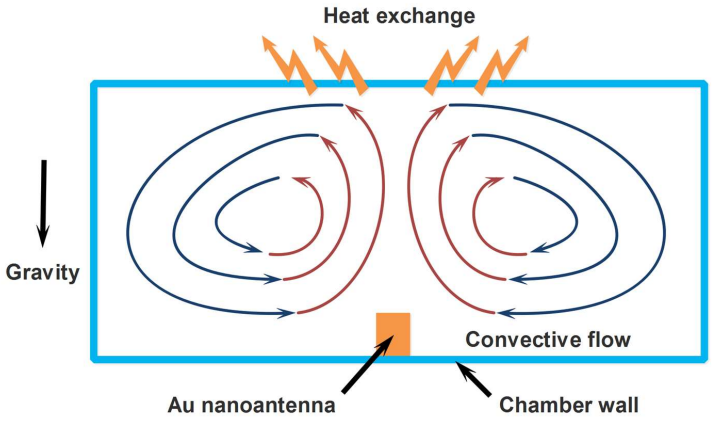

Figure 1.12. Schematic of thermal convection.

Theoretical background: The thermo-induced water flow expected around a plasmonic nanostructure (such as an Au nanoantenna) under illumination arises from dissipative losses in metals. The flow results from the combination of heat transfer (in the solids and fluids of the system) with the resultant buoyancy-driven natural convection. We describe our modelling approach below. In summary, the physics is described by a set of coupled partial differential equations combining optics, thermodynamics and hydrodynamics phenomena,[42, 43, 49, 54] which we numerically solve in the FEM package of COMSOL Multiphysics.

In the first step, we solve the time-independent vector wave equation for a monochromatic electric field around our optical nanotweezer (e.g., Au nanoantenna), that is:[49]

$$\nabla \times (\nabla \times \vec{E}) - k_0^2 \varepsilon(\vec{r}) \vec{E} = 0 \tag{1.25}$$

where $\vec{E}$ is the total electric field (i.e., the incident and scattered field), $k_0 = 2\pi / \lambda$ is the free-space wavenumber with the free-space wavelength λ, and $\varepsilon(\vec{r}) = \varepsilon'(\vec{r}) - i\varepsilon''(\vec{r})$ is the complex and position dependent permittivity. The electric field distribution determined from eq 1.25 is used to calculate the heat source density inside the nanoantenna, which is given by:[40]

$$q(\vec{r}) = \frac{1}{2} \mathrm{Re}[\vec{J}^*(\vec{r}) \bullet \vec{E}(\vec{r})] = \frac{\omega}{2} \mathrm{Im}(\varepsilon_{Au}) \left| \vec{E}(\vec{r}) \right|^2 \tag{1.26}$$

where ω is the angular frequency of the illumination, ε_{Au} is the gold permittivity, $\vec{J}(\vec{r})$ is the complex current density phasor, and $\vec{E}(\vec{r})$ is the complex electric field phasor. The generated heat power can be computed by a volume integral over the nanoantenna:

$$Q = \int_V q(\vec{r}) dV \tag{1.27}$$

The heat density (or heat power) acts as the source term in the heat diffusion equations for determining the temperature distribution on the nanoantenna surface as well as in the surrounding water and the underlying substrate. The heat density inside the nanoantenna is strongly dependent on its geometry and can be highly non-uniform. This produces a temperature distribution in the nanoantenna governed by the following heat diffusion equation:[42]

$$\rho_{Au} C_{Au} \frac{\partial T(\vec{r},t)}{\partial t} - \nabla \bullet (\kappa_{Au} \nabla T(\vec{r},t)) = q(\vec{r}) \tag{1.28}$$

where κ_{Au} is the thermal conductivity of Au, ρ_{Au} is the density of Au, and C_{Au} is the heat capacity of Au. It should be noted that the temperature profile inside the nanoantenna is usually quite uniform in spite of the non-uniformity of the heat source density.[42] This is because the thermal conductivity of Au is much larger than that of water. The solution of eq 1.28 is time-dependent, and after a characteristic time (~ 0.1 μs),[42] it reaches steady state. The characteristic time is short because the Reynolds number in the system is very small. We consider the steady state problem, i.e., the temperature does not change with the time and the first term in eq 1.28 disappears. The heat transfer in Au can thus be expressed as:

$$-\nabla \bullet (\kappa_{Au} \nabla T(\vec{r})) = q(\vec{r}) \tag{1.29}$$

Outside the Au nanoantenna, it is not necessary to consider heat sources because the absorption of light by the water is negligible in comparison to that in the nanoantenna (i.e., $q_{water}(\vec{r}) = 0$). Thermal-induced convection may occur, however. The steady state temperature distribution in the surrounding water is determined by the following equation:[43]

$$\rho_f C_f \vec{u}(\vec{r}) \bullet \nabla T(\vec{r}) - \nabla \bullet (\kappa_f \nabla T(\vec{r})) = 0 \tag{1.30}$$

where $\vec{u}(\vec{r})$ is the velocity field of water, κ_f is the thermal conductivity of water, ρ_f is the density of water, and C_f is the heat capacity of water. The first term in eq 1.30 is the convection term depending on the velocity field of the water, while the second term is the heat conduction term.

Because the water around the nanoantenna increases in temperature, it will experience some reduction in its mass density, which generates an upward convection of water. When temperature variations in a flow are small, it can often be assumed incompressible, that is, the water density ρ_f is constant or nearly constant. For an incompressible flow, the general equation governing this stable water convection velocity is the incompressible Navier–Stokes equation:[43]

$$\begin{cases} \rho_0(\vec{u}(\vec{r})\bullet\nabla)\vec{u}(\vec{r}) = -\nabla p(\vec{r}) + \mu\nabla^2\vec{u}(\vec{r}) + \vec{f} \\ \rho_0\nabla\bullet\vec{u}(\vec{r}) = 0 \end{cases} \tag{1.31}$$

where the temperature-dependent and pressure-dependent water density ρ_f has been replaced by a constant density ρ_0 (i.e., the reference water density), μ is the viscosity of water, p is the pressure, and $\vec{f}$ is the body force per unit volume because of the temperature non-uniformity. This thermal force term can be estimated with the Boussinesq approximation, which is a popular way to solve the non-isothermal flow and is accurate when the density variations are small (incompressible flow). It assumes that the density variations have little influence on the water velocity field, except they are only significant in buoyancy. This approximation elucidates the density dependence by introducing an external buoyancy force due to the temperature increase:[54]

$$\vec{f}_{buoy} = -\rho_0\beta(T(\vec{r}) - T_0)\vec{g} \tag{1.32}$$

where $\vec{g}$ is the acceleration due to gravity, T_0 is the initial temperature, and β is the thermal expansion coefficient of water. In the modelling, we furthermore assume that

the heat power is uniformly distributed throughout the nanoantenna volume due to the high thermal conductivity of the material, and $\vec{q}(r)$ reduces to a scalar:

$$q = \frac{\int_V q(\vec{r})dV}{V} \tag{1.33}$$

By combining eqs 1.29–1.32 and solving numerically, the temperature distributions in the nanoantenna and water and the convection velocity fields can be obtained. From the above discussion, it can be understood that, to achieve a low temperature rise, two main approaches can be employed. First, fabricate nanostructures with materials having the low imaginary part of the permittivity, such as dielectric materials, to reduce the heat power. Second, use a heat sink approach or other designs with employing materials with high thermal conductivity to dissipate the generated heat. This dissertation explores both methods, including plasmonic nanoapertures and all-dielectric (Si) nanoantennas.

1.5 All-dielectric nanoantennas

Plasmonic nanoantennas present a means to confine light to a deeply subwavelength scale, which is advantageous not only for optical nanotweezers but for other applications such as surface enhanced spectroscopy. This subwavelength field confinement is accompanied by high absorption in the metal (from which the plasmonic nanoantenna) is formed, and thus to heating. The need for reduced local heating has been emphasized for a lot of practical applications of nanoantennas (and not just nanotweezers), prompting recent theoretical and experimental interests into all-dielectric nanoantennas (or nanostructures, Figure 1.13)[55-57] that are made from dielectric materials rather than metals. It should be noted that “dielectric” is used in this context to refer to materials that are not metals and includes semiconductors such as

silicon. One example of this approach is the all-dielectric optical Yagi-Uda nanoantenna (Figure 1.14a).[55] Unlike plasmonic nanoantennas fabricated from metals, all-dielectric nanoantennas are made of low-loss high refractive index materials (Figure 1.15), such as Si, germanium or gallium phosphide (i.e., non-plasmonic materials).[58, 59]

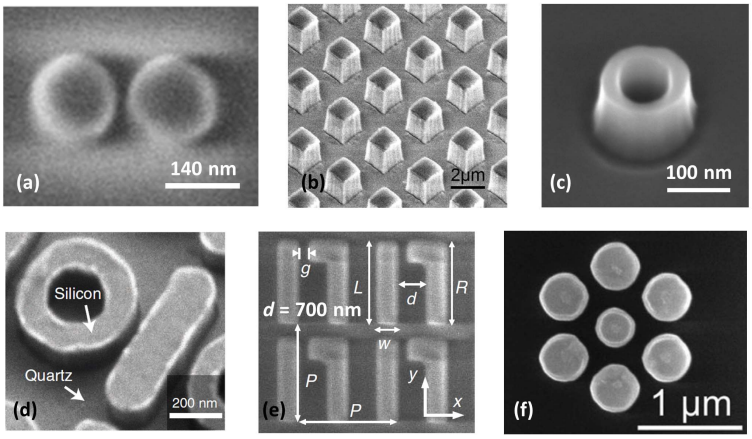

Figure 1.13. Examples of all-dielectric nanostructures. (a) Si nanodimers (reproduced from ref 60). (b) Cubic tellurium resonators (reproduced from ref 61). (c) Hollow Si nanocylinders (reproduced from ref 62). (d) Si rectangular bar and ring resonators (reproduced from ref 63). (e) Si-based chiral metasurfaces (reproduced from ref 64). (f) Si heptamer oligomers (reproduced from ref 65).

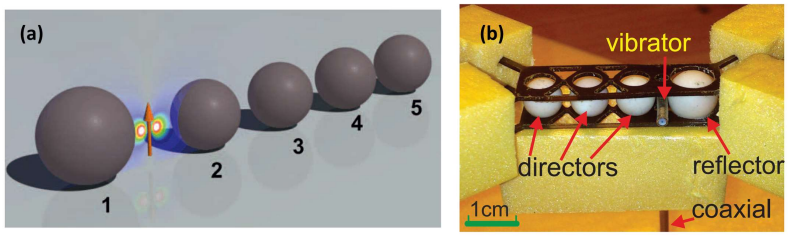

Figure 1.14. (a) Schematic view of an all-dielectric optical Yagi-Uda nanoantenna (reproduced from ref 55). (b) Photograph of the all-dielectric Yagi-Uda microwave antenna (reproduced from ref 66).

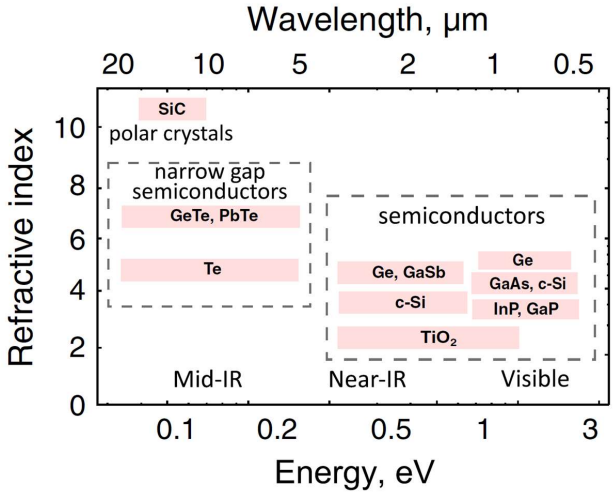

Figure 1.15. High refractive index materials (reproduced from ref 58).

The differences between the optical responses of dielectric and plasmonic nanoantennas can be understood by examining the solution to Maxwell's equations calculated for each configuration. For physical interpretation, however, it is helpful to consider the effect of the material (metal or dielectric) in determining the optical response. The main difference between the optical response of dielectric and plasmonic nanoantennas is the nature of the currents induced by an incident light field (Figure 1.16a). In plasmonic (metallic) nanoantennas, the free electrons in the conduction band dominate the optical response as they are driven into oscillations by the external electric field. In other words, the nanoantenna effects are based on the oscillations of the free electron plasma. These oscillations are accompanied by strong dissipative losses of an ohmic nature. In contrast, optical resonances of dielectric nanoantennas originate from circular displacement currents owing to the oscillations of bound electrons. These currents do not have the strong ohmic damping displayed by the plasmonic nanoantennas, and dielectric nanoantennas thus have lower heat generation. Based on the different physical mechanism, all-dielectric nanoantennas show different resonance properties. Two of the key benefits they have over plasmonic nanoantennas are as

follows. First, as discussed, because of low dissipative losses, heat generation by dielectric nanoantennas is small, and the temperature rises that occur can be much smaller than what would occur for a comparable plasmonic nanoantenna. Second, all-dielectric nanoantennas feature both strong electric and magnetic resonant modes at the nanoscale ("hotspots"). For example, Bakker et al. demonstrated that for an isolated silicon nanodimer (i.e., a pair of nanoparticles separated by a small gap), the hotspot in the gap area can have either an electric or a magnetic character, depending on the polarization of the incident field (Figure 1.16b).[60]

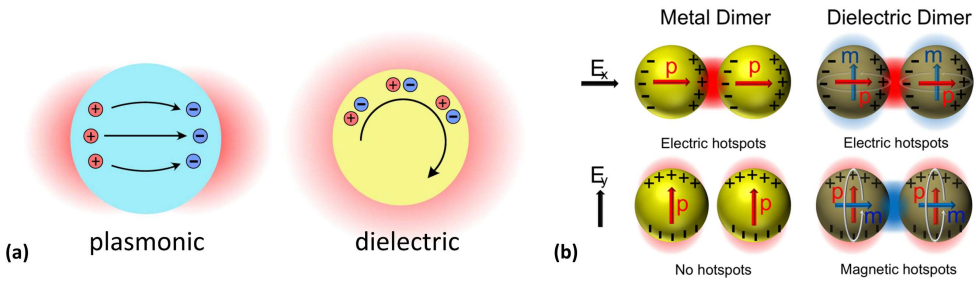

Figure 1.16. (a) Schematic illustration of the induced currents in plasmonic and dielectric nanoparticles (reproduced from ref 58). (b) Schematic of the hotspot formation in plasmonic and dielectric nanodimers (reproduced from ref 60).

All-dielectric nanoantennas can be an attractive alternative to their plasmonic counterparts to manipulate light at the nanoscale. They not only provide a low-loss platform, but they offer several additional opportunities based on the strong electric and magnetic responses that they can support. The near-field enhancements they provide are generally lower than those provided by plasmonic nanostructures, but are large enough for many applications. For example, Si dimer nanoantennas on glass substrates have been employed to enhance fluorescence and Raman scattering from a dense layer of dye molecules covering them, with negligible temperature rise.[67] In that work, simulations predicted an electric field enhancement of 5.5 for a 20 nm gap width (Figure 1.17). One can expect that even greater enhancements would be achieved for smaller gap widths. It

was also shown that silicon dimer nanoantennas can enhance the fluorescence from single molecules.[68] Another demonstration on this theme involved the use of silicon nanoresonators for biosensing, with Yavas et al. demonstrating the detection of protein cancer markers in human serum.[69] In the field of nonlinear optics, Shcherbakov et al. observed the enhanced third-harmonic generation from Si nanodisks which exhibit both electric and magnetic dipolar resonances.[70]

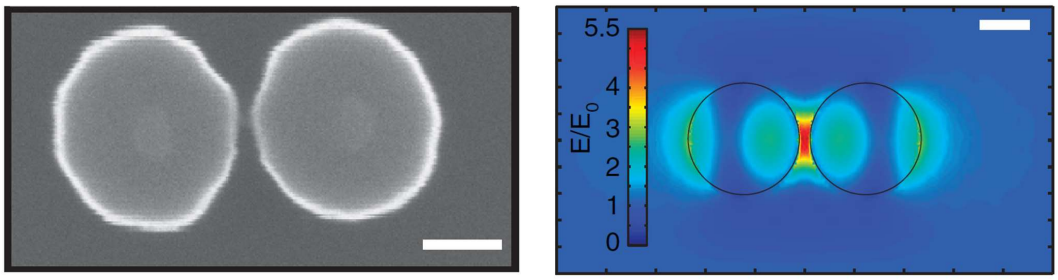

Figure 1.17. Scanning electron micrograph image (left) and numerical near-field distribution excited at resonance (right) of a Si nanodimer with a 20 nm gap (reproduced from ref 67). Scale bar: 100 nm.

1.6 Optical trapping of quantum dots

Colloidal quantum dots (QDs), also known as semiconductor nanoparticles, are three-dimensional nanoscale crystals in which free electrons are confined in a semiconductor matrix. Semiconductor QDs were first discovered by Rossetti et al. at Bell Labs in 1983[71] and termed "quantum dots" by Reed et al. at Yale University.[72] The sizes and shapes of QDs can be accurately controlled by the use of advanced nanofabrication technology.[73] The potential barrier in a QD results in a series of discrete, atomic-like energy levels for the valence band hole and conduction band electron states of semiconductors. These energy levels are strongly dependent on the size of the QD.[74] The properties of QDs can be thought of as being between those of the discrete molecules and bulk semiconductors. Generally, larger QDs (diameters of 5–6 nm, for

example) emit longer wavelength light (e.g., red or orange) and smaller QDs (diameters of 2–3 nm, for example) emit shorter wavelength light (e.g., blue or green). Because of wave–particle duality in quantum mechanics, the state of a particle is described by a wave function. The energy levels and wave functions of a single carrier (i.e., electrons and holes) correspond to the eigenvalues and eigenfunctions of the Schrödinger equation:[75]

$$-\nabla \bullet (\frac{h^2}{8\pi^2 m_e}\nabla\Psi) + V\Psi = E\Psi \tag{1.34}$$

where h is the Planck's constant, Ψ is the wave function, E is the eigenvalue, V is the potential energy and m_e is the effective carrier mass. As an example, we show three lowest electron eigenwave functions of a CdSe/ZnS core-shell QD for the principal quantum number l = 0 (Figure 1.18), simulated with COMSOL PDE Module (partial differential equation). A large number of applications for QDs have been explored over the last decade, including infrared detection, lasers, second-harmonic generation, ultrafast all-optical switches, quantum computing, and as fluorescent markers for biological labelling. For the latter, QDs offer many favourable attributes,[76] such as size-dependent emission, large linear and nonlinear absorption cross-sections, high brightness, high quantum yield and excellent photostability.

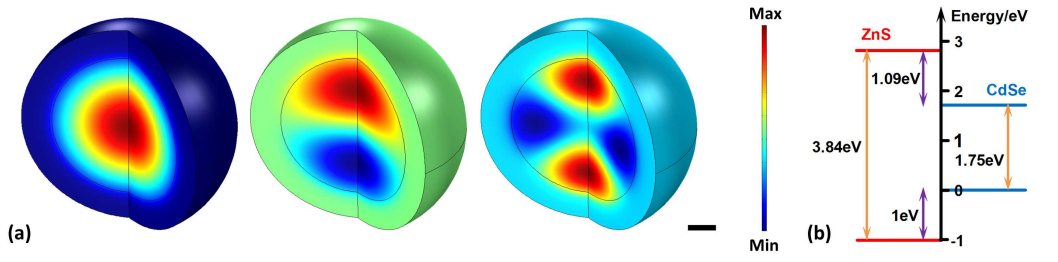

Figure 1.18. (a) The three lowest electronic states for the case of l = 0. CdSe/ZnS core-shell QDs: CdSe core radius = 5 nm, ZnS shell thickness = 2 nm. Scale bar: 2 nm. (For electrons: V = 0 for CdSe and V = 1.09 eV for ZnS; $m_e = 0.11m_0$ for CdSe and $m_e = 0.27m_0$ for ZnS; data from ref 77) (b) The corresponding energy diagram of QDs.

Optical trapping of QDs: In nanotechnology, QDs are very attractive candidates for nanomaterial-based applications.[14, 78] In recent years, there has been much interest in using optical tweezers to trap nanomaterials for a variety of reasons, including to localize these materials to facilitate their characterization via spectroscopy with biological applications.[79] QDs can be optically trapped by conventional optical tweezers and by near-field nanotweezers (Figure 1.19). In 2008, Jauffred et al. first demonstrated that individual QDs can be optically trapped and manipulated in free space by conventional optical tweezers with an infrared continuous wave (CW) laser.[80] The same group later reported that individual QDs can be not only trapped by the trapping laser, but also excited simultaneously by two-photon absorption with the same CW infrared trapping beam.[81] Observations of optical trapping and two-photon excitation of QDs have also been reported using picosecond[82] and femtosecond[83] pulsed lasers, respectively, by conventional optical tweezers. The OT of single QDs has also been explored using various near-field trapping techniques. In particular, Erickson's group showed that QDs can be trapped and released on-demand in the close vicinity of the silicon nitride photonic crystal resonators, but it is difficult to clearly resolve the individual QDs from the fluorescence microscope images they provided.[84] Plasmonic nanoantennas and nanoapertures can also trap QDs with relatively weak illuminations. The former was demonstrated by Tsuboi et al. in 2010, with the nanoantennas comprising gold nanodimer arrays.[85] Experimental demonstration of the trapping of individual QDs was achieved using a bowtie nanoaperture in a silver film by Jensen et al. (for silica-coated QDs)[37] and using a DNH aperture in a gold film from Reuven Gordon's group.[86]

At this point we note three interesting phenomena concerning the optical trapping of QDs that have been reported in the literature. First, Jauffred and Oddershede trapped

QDs with different sizes, but found little dependence of the optical force with size, which runs counter to the (approximately) cubic dependence (force versus diameter) that would be expected.[81] Second, Chiang et al. demonstrated that the efficient two-photon absorption process enhances the trapping ability of QDs by analysing Rayleigh scattering image.[83] Third, using plasmonic nanoantennas, single QDs can be particularly trapped with weak light illumination, where the trapping potential energy is smaller than the thermal energy, as experimentally demonstrated by Tsuboi et al.[85] We anticipate that the complete description of trapping behaviour could be a powerful means for the better understanding of optical tweezers and nanotweezers.

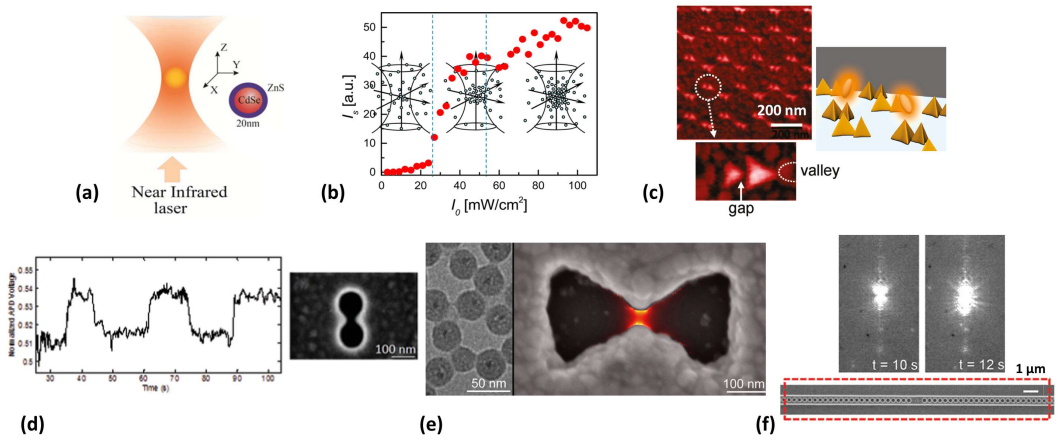

Figure 1.19. (a) Optical trapping (OT) with CW lasers (reproduced from ref 78). (b) OT of CdTe QDs with femtosecond lasers (reproduced from ref 83). (c) OT using Au nanodimers (reproduced from ref 85). (d) OT using DNH apertures (reproduced from ref 86). (e) OT of silica-coated QDs using silver bowtie apertures (reproduced from ref 37). (f) OT of QDs using silicon nitride photonic crystal resonators (reproduced from ref 84).

1.7 Two-photon absorption

Nonlinear optics refers to the field of study concerned with the fact the induced electric polarization in a material can have a nonlinear dependence on the external light field (electric field).[87] One of the important phenomena in nonlinear optics is the optical Kerr

effect. At low intensities, the refractive index of a material is fairly independent of the light intensity. However, when the intensity is high, the refractive index starts to depend on the external intensity. This is the optical Kerr effect. The intensity-dependent nonlinear refractive index can be written as:[88]

$$n = n_0 + \Delta n(I) = n_0 + I\gamma \tag{1.35}$$

where n is the total refractive index, n_0 is the linear (constant) refractive index, γ (in units of m^2/W) is the nonlinear refractive index coefficient and I is the light intensity. It can be seen that the total refractive index is a linear function of the light intensity. For CdSe at 1064 nm, we have coefficient $\gamma = -1.47 \times 10^{-18}$ m^2/W.[88]

Two-photon absorption: Two-photon absorption (TPA) is a third-order nonlinear optical process involving the simultaneous absorption of two low-energy photons having identical or different energies. This excites a molecule or NP (or some other material) from the ground state to an excited state via an intermediate (or virtual) state (Figure 1.20).[87-90] The energy difference between these two states is equal to the sum of the energies of the two photons. As this process concerns the simultaneous absorption of two photons, the emitted fluorescent intensity is proportional to the square of the incident light intensity. It is thus advantageous to use a pulsed laser, to achieve a greater instantaneous optical intensity. This fluorescence is known as the two-photon-excited fluorescence. Materials exhibiting TPA are often characterized by their TPA cross-sections (σ_{TPA}). By contrast, in a linear excitation process, the energy of each photon is large enough to promote an electron to the excited state. Therefore, only one photon is absorbed at a time. In this case, the fluorescent intensity is linearly dependent on the incident light intensity.

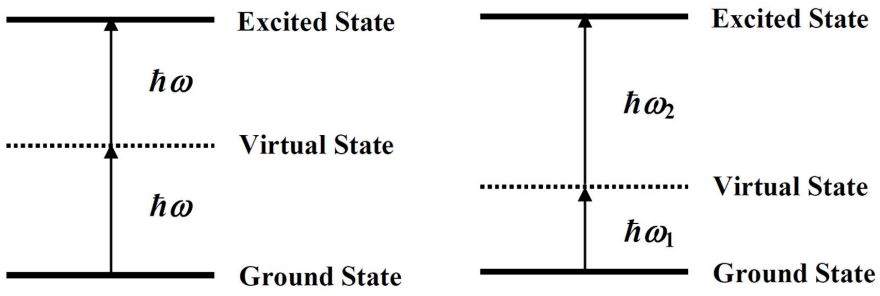

Figure 1.20. Schematic diagrams of degenerate (left) and non-degenerate (right) TPA.

In this dissertation, we present results in which single fluorescent NSs and individual CdSe/ZnS QDs are excited from the ground states to the excited states via both linear and nonlinear absorption processes. In the linear absorption experiments (one-photon excitation), a green laser (wavelength 532 nm) is used to excite fluorescence from the NSs or QDs. In the nonlinear absorption experiments (two-photon excitation), the illumination source is the infrared laser (wavelength 1064 nm) also used for the trapping. The fluorescence emission that follows occurs in the same manner after both excitation processes.

References

1. Nichols, E. F.; Hull, G. A preliminary communication on the pressure of heat and light radiation. *Physical Review (Series I)* 1901, 13, 307.

2. Ashkin, A. Acceleration and trapping of particles by radiation pressure. *Physical Review Letters* 1970, 24, 156-159.

3. Ashkin, A.; Dziedzic, J. M.; Bjorkholm, J.; Chu, S. Observation of a single-beam gradient force optical trap for dielectric particles. *Optics Letters* 1986, 11, 288-290.

4. Chu, S.; Bjorkholm, J.; Ashkin, A.; Cable, A. Experimental observation of optically trapped atoms. *Physical Review Letters* 1986, 57, 314.

5. Ashkin, A.; Dziedzic, J. M. Optical trapping and manipulation of viruses and bacteria. *Science* 1987, 235, 1517-1520.

6. Ashkin, A. History of optical trapping and manipulation of small-neutral particle, atoms, and molecules. *IEEE Journal of Selected Topics in Quantum Electronics* 2000, 6, 841-856.

7. Grier, D. G. A revolution in optical manipulation. *Nature* 2003, 424, 810-816.

8. Neuman, K. C.; Block, S. M. Optical trapping. *Review of Scientific Instruments* 2004, 75, 2787-2809.

9. Novotny, L.; Hecht, B. *Principles of Nano-Optics*. Cambridge University Press: 2012.

10. Albaladejo, S.; Marqués, M. I.; Laroche, M.; Sáenz, J. J. Scattering forces from the curl of the spin angular momentum of a light field. *Physical Review Letters* 2009, 102, 113602.

11. Spesyvtseva, S. E. S.; Dholakia, K. Trapping in a material world. *ACS Photonics* 2016, 3, 719-736.

12. Jackson, J. D. *Classical Electrodynamics*. New York: Wiley and Sons: 1975.

13. Wong, W. P.; Halvorsen, K. The effect of integration time on fluctuation measurements: calibrating an optical trap in the presence of motion blur. *Optics Express* 2006, 14, 12517-12531.

14. Maragò, O. M.; Jones, P. H.; Gucciardi, P. G.; Volpe, G.; Ferrari, A. C. Optical trapping and manipulation of nanostructures. *Nature Nanotechnology* 2013, 8, 807.

15. Grigorenko, A.; Roberts, N.; Dickinson, M.; Zhang, Y. Nanometric optical tweezers based on nanostructured substrates. *Nature Photonics* 2008, 2, 365-370.

16. Juan, M. L.; Gordon, R.; Pang, Y.; Eftekhari, F.; Quidant, R. Self-induced back-action optical trapping of dielectric nanoparticles. *Nature Physics* 2009, 5, 915-919.

17. Zhang, W.; Huang, L.; Santschi, C.; Martin, O. J. Trapping and sensing 10 nm metal nanoparticles using plasmonic dipole antennas. *Nano Letters* 2010, 10, 1006-1011.

18. Juan, M. L.; Righini, M.; Quidant, R. Plasmon nano-optical tweezers. *Nature Photonics* 2011, 5, 349-356.

19. Shoji, T.; Tsuboi, Y. Plasmonic optical tweezers toward molecular manipulation: tailoring plasmonic nanostructure, light source, and resonant trapping. *The Journal of Physical Chemistry Letters* 2014, 5, 2957-2967.

20. Yang, A. H.; Moore, S. D.; Schmidt, B. S.; Klug, M.; Lipson, M.; Erickson, D. Optical manipulation of nanoparticles and biomolecules in sub-wavelength slot waveguides. *Nature* 2009, 457, 71-75.

21. Lin, S.; Schonbrun, E.; Crozier, K. B. Optical manipulation with planar silicon microring resonators. *Nano Letters* 2010, 10, 2408-2411.

22. Mandal, S.; Serey, X.; Erickson, D. Nanomanipulation using silicon photonic crystal resonators. *Nano Letters* 2010, 10, 99-104.

23. Pang, Y.; Gordon, R. Optical trapping of a single protein. *Nano Letters* 2011, 12, 402-406.

24. Kwak, E. S.; Onuta, T. D.; Amarie, D.; Potyrailo, R.; Stein, B.; Jacobson, S. C.; Schaich, W.; Dragnea, B. Optical trapping with integrated near-field apertures. *The Journal of Physical Chemistry B* 2004, 108, 13607-13612.

25. Righini, M.; Ghenuche, P.; Cherukulappurath, S.; Myroshnychenko, V.; García de Abajo, F.; Quidant, R. Nano-optical trapping of Rayleigh particles and Escherichia coli bacteria with resonant optical antennas. *Nano Letters* 2009, 9, 3387-3391.

26. Johnson, P. B.; Christy, R. W. Optical constants of the noble metals. *Physical Review B* 1972, 6, 4370-4379.

27. Barnes, W. L.; Dereux, A.; Ebbesen, T. W. Surface plasmon subwavelength optics. *Nature* 2003, 424, 824.

28. Ritchie, R. Plasma losses by fast electrons in thin films. *Physical Review* 1957, 106, 874.

29. Bohren, C. F.; Huffman, D. R. *Absorption and Scattering of Light by Small Particles*. John Wiley & Sons: 2008.

30. Zeng, S.; Baillargeat, D.; Ho, H. P.; Yong, K. T. Nanomaterials enhanced surface plasmon resonance for biological and chemical sensing applications. *Chemical Society Reviews* 2014, 43, 3426-3452.

31. Rycenga, M.; Cobley, C. M.; Zeng, J.; Li, W.; Moran, C. H.; Zhang, Q.; Qin, D.; Xia, Y. Controlling the synthesis and assembly of silver nanostructures for plasmonic applications. *Chemical Reviews* 2011, 111, 3669-3712.

32. Chen, C.; Juan, M. L.; Li, Y.; Maes, G.; Borghs, G.; Van Dorpe, P.; Quidant, R. Enhanced optical trapping and arrangement of nano-objects in a plasmonic nanocavity. *Nano Letters* 2012, 12, 125-132.

33. Pang, Y.; Gordon, R. Optical trapping of 12 nm dielectric spheres using double-nanoholes in a gold film. *Nano Letters* 2011, 11, 3763-3767.

34. Berthelot, J.; Aćimović, S.; Juan, M.; Kreuzer, M.; Renger, J.; Quidant, R. Three-dimensional manipulation with scanning near-field optical nanotweezers. *Nature Nanotechnology* 2014, 9, 295-299.

35. Yoo, D.; Kargal laxminarayana, G.; Choi, H. K.; Mohr, D. A.; Ertsgaard, C. T.; Gordon, R.; Oh, S. H. Low-Power Optical Trapping of Nanoparticles and Proteins with Resonant Coaxial Nanoaperture using 10 nm gap. *Nano Letters* 2018, 18, 3637-3642.

36. Al Balushi, A. A.; Kotnala, A.; Wheaton, S.; Gelfand, R. M.; Rajashekara, Y.; Gordon, R. Label-free free-solution nanoaperture optical tweezers for single molecule protein studies. *Analyst* 2015, 140, 4760-4778.

37. Jensen, R. A.; Huang, I. C.; Chen, O.; Choy, J. T.; Bischof, T. S.; Lončar, M.; Bawendi, M. G. Optical trapping and two-photon excitation of colloidal quantum dots using bowtie apertures. *ACS Photonics* 2016, 3, 423-427.

38. Xu, H.; Jones, S.; Choi, B. C.; Gordon, R. Characterization of individual magnetic nanoparticles in solution by double nanohole optical tweezers. *Nano Letters* 2016, 16, 2639-2643.

39. Mestres, P.; Berthelot, J.; Aćimović, S. S.; Quidant, R. Unraveling the optomechanical nature of plasmonic trapping. *Light: Science & Applications* 2016, 5, 1-14.

40. Baffou, G.; Quidant, R. Thermo-plasmonics: using metallic nanostructures as nano-sources of heat. *Laser & Photonics Reviews* 2013, 7, 171-187.

41. Bergman, T. L.; Incropera, F. P.; Lavine, A. S.; DeWitt, D. P. *Introduction to Heat Transfer*. John Wiley & Sons: 2011.

42. Donner, J. S.; Baffou, G.; McCloskey, D.; Quidant, R. Plasmon-assisted optofluidics. *ACS Nano* 2011, 5, 5457-5462.

43. Wang, K.; Crozier, K. B. Plasmonic trapping with a gold nanopillar. *Chemphyschem : a European journal of chemical physics and physical chemistry* 2012, 13, 2639-2648.

44. Wang, K.; Schonbrun, E.; Steinvurzel, P.; Crozier, K. B. Trapping and rotating nanoparticles using a plasmonic nano-tweezer with an integrated heat sink. *Nature Communications* 2011, 2, 469.

45. Roxworthy, B. J.; Ko, K. D.; Kumar, A.; Fung, K. H.; Chow, E. K.; Liu, G. L.; Fang, N. X.; Toussaint Jr, K. C. Application of plasmonic bowtie nanoantenna arrays for optical trapping, stacking, and sorting. *Nano Letters* 2012, 12, 796-801.

46. Xu, Z.; Song, W.; Crozier, K. B. Direct particle tracking observation and Brownian dynamics simulations of a single nanoparticle optically trapped by a plasmonic nanoaperture. *ACS Photonics* 2018, 5, 2850-2859.

47. Huang, X.; El-Sayed, I. H.; Qian, W.; El-Sayed, M. A. Cancer cell imaging and photothermal therapy in the near-infrared region by using gold nanorods. *Journal of the American Chemical Society* 2006, 128, 2115-2120.

48. Lin, L.; Wang, M.; Peng, X.; Lissek, E. N.; Mao, Z.; Scarabelli, L.; Adkins, E.; Coskun, S.; Unalan, H. E.; Korgel, B. A.; Liz-Marzán, L. M.; Florin, E. L.; Zheng, Y. Opto-thermoelectric nanotweezers. *Nature Photonics* 2018, 12, 195-201.

49. Ndukaife, J. C.; Kildishev, A. V.; Nnanna, A. G.; Shalaev, V. M.; Wereley, S. T.; Boltasseva, A. Long-range and rapid transport of individual nano-objects by a hybrid electrothermoplasmonic nanotweezer. *Nature Nanotechnology* 2016, 11, 53-60.

50. Duhr, S.; Braun, D. Why molecules move along a temperature gradient. *Proceedings of the National Academy of Sciences* 2006, 103, 19678-19682.

51. Piazza, R.; Parola, A. Thermophoresis in colloidal suspensions. *Journal of Physics: Condensed Matter* 2008, 20, 153102.

52. Jiang, H.; Wada, H.; Yoshinaga, N.; Sano, M. Manipulation of colloids by a nonequilibrium depletion force in a temperature gradient. *Physical Review Letters* 2009, 102, 208301.

53. Braibanti, M.; Vigolo, D.; Piazza, R. Does thermophoretic mobility depend on particle size? *Physical Review Letters* 2008, 100, 108303.

54. Roxworthy, B. J.; Bhuiya, A. M.; Vanka, S. P.; Toussaint, K. C., Jr. Understanding and controlling plasmon-induced convection. *Nature Communications* 2014, 5, 3173.

55. Krasnok, A. E.; Miroshnichenko, A. E.; Belov, P. A.; Kivshar, Y. S. All-dielectric optical nanoantennas. *Optics Express* 2012, 20, 20599-20604.

56. Krasnok, A. E.; Maksymov, I. S.; Denisyuk, A. I.; Belov, P. A.; Miroshnichenko, A. E.; Simovski, C. R.; Kivshar, Y. S. Optical nanoantennas. *Physics-Uspekhi* 2013, 56, 539.

57. Kuznetsov, A. I.; Miroshnichenko, A. E.; Brongersma, M. L.; Kivshar, Y. S.; Luk'yanchuk, B. Optically resonant dielectric nanostructures. *Science* 2016, 354, aag2472.

58. Baranov, D. G.; Zuev, D. A.; Lepeshov, S. I.; Kotov, O. V.; Krasnok, A. E.; Evlyukhin, A. B.; Chichkov, B. N. All-dielectric nanophotonics: the quest for better materials and fabrication techniques. *Optica* 2017, 4, 814-825.

59. Jahani, S.; Jacob, Z. All-dielectric metamaterials. *Nature Nanotechnology* 2016, 11, 23.

60. Bakker, R. M.; Permyakov, D.; Yu, Y. F.; Markovich, D.; Paniagua-Domínguez, R.; Gonzaga, L.; Samusev, A.; Kivshar, Y.; Luk'yanchuk, B.; Kuznetsov, A. I. Magnetic and electric hotspots with silicon nanodimers. *Nano Letters* 2015, 15, 2137-2142.

61. Ginn, J. C.; Brener, I.; Peters, D. W.; Wendt, J. R.; Stevens, J. O.; Hines, P. F.; Basilio, L. I.; Warne, L. K.; Ihlefeld, J. F.; Clem, P. G. Realizing optical magnetism from dielectric metamaterials. *Physical Review Letters* 2012, 108, 097402.

62. van de Haar, M. A.; van de Groep, J.; Brenny, B. J.; Polman, A. Controlling magnetic and electric dipole modes in hollow silicon nanocylinders. *Optics Express* 2016, 24, 2047-2064.

63. Yang, Y.; Kravchenko, I. I.; Briggs, D. P.; Valentine, J. All-dielectric metasurface analogue of electromagnetically induced transparency. *Nature Communications* 2014, 5, 5753.

64. Wu, C.; Arju, N.; Kelp, G.; Fan, J. A.; Dominguez, J.; Gonzales, E.; Tutuc, E.; Brener, I.; Shvets, G. Spectrally selective chiral silicon metasurfaces based on infrared Fano resonances. *Nature Communications* 2014, 5, 3892.

65. Chong, K. E.; Hopkins, B.; Staude, I.; Miroshnichenko, A. E.; Dominguez, J.; Decker, M.; Neshev, D. N.; Brener, I.; Kivshar, Y. S. Observation of Fano resonances in all-dielectric nanoparticle oligomers. *Small* 2014, 10, 1985-1990.

66. Filonov, D. S.; Krasnok, A. E.; Slobozhanyuk, A. P.; Kapitanova, P. V.; Nenasheva, E. A.; Kivshar, Y. S.; Belov, P. A. Experimental verification of the concept of all-dielectric nanoantennas. *Applied Physics Letters* 2012, 100, 201113.

67. Caldarola, M.; Albella, P.; Cortés, E.; Rahmani, M.; Roschuk, T.; Grinblat, G.; Oulton, R. F.; Bragas, A. V.; Maier, S. A. Non-plasmonic nanoantennas for surface enhanced spectroscopies with ultra-low heat conversion. *Nature Communications* 2015, 6, 7915.

68. Regmi, R.; Berthelot, J.; Winkler, P. M.; Mivelle, M.; Proust, J.; Bedu, F. d. r.; Ozerov, I.; Begou, T.; Lumeau, J.; Rigneault, H. All-dielectric silicon nanogap antennas to enhance the fluorescence of single molecules. *Nano Letters* 2016, 16, 5143-5151.

69. Yavas, O.; Svedendahl, M.; Dobosz, P.; Sanz, V.; Quidant, R. On-a-chip biosensing based on all-dielectric nanoresonators. *Nano Letters* 2017, 17, 4421-4426.

70. Shcherbakov, M. R.; Neshev, D. N.; Hopkins, B.; Shorokhov, A. S.; Staude, I.; Melik-Gaykazyan, E. V.; Decker, M.; Ezhov, A. A.; Miroshnichenko, A. E.; Brener, I. Enhanced third-harmonic generation in silicon nanoparticles driven by magnetic response. *Nano Letters* 2014, 14, 6488-6492.

71. Rossetti, R.; Nakahara, S.; Brus, L. E. Quantum size effects in the redox potentials, resonance Raman spectra, and electronic spectra of CdS crystallites in aqueous solution. *The Journal of Chemical Physics* 1983, 79, 1086-1088.

72. Reed, M.; Bate, R.; Bradshaw, K.; Duncan, W.; Frensley, W.; Lee, J.; Shih, H. Spatial quantization in GaAs–AlGaAs multiple quantum dots. *Journal of Vacuum Science & Technology B: Microelectronics Processing and Phenomena* 1986, 4, 358-360.

73. Kouwenhoven, L.; Marcus, C. Quantum dots. *Physics World* 1998, 11, 35.

74. Alivisatos, A. P. Semiconductor clusters, nanocrystals, and quantum dots. *Science* 1996, 271, 933-937.

75. Griffiths, D. J.; Schroeter, D. F. *Introduction to quantum mechanics*. Cambridge University Press: 2018.

76. Medintz, I. L.; Uyeda, H. T.; Goldman, E. R.; Mattoussi, H. Quantum dot bioconjugates for imaging, labelling and sensing. *Nature Materials* 2005, 4, 435.

77. Trager-Cowan, C.; Parbrook, P.; Henderson, B.; O'Donnell, K. Band alignments in Zn (Cd) S (Se) strained layer superlattices. *Semiconductor Science and Technology* 1992, 7, 536.

78. Bendix, P. M.; Jauffred, L.; Norregaard, K.; Oddershede, L. B. Optical trapping of nanoparticles and quantum dots. *IEEE Journal of Selected Topics in Quantum Electronics* 2014, 20, 15-26.

79. Norregaard, K.; Metzler, R.; Ritter, C. M.; Berg-Sørensen, K.; Oddershede, L. B. Manipulation and motion of organelles and single molecules in living cells. *Chemical Reviews* 2017, 117, 4342-4375.

80. Jauffred, L.; Richardson, A. C.; Oddershede, L. B. Three-dimensional optical control of individual quantum dots. *Nano Letters* 2008, 8, 3376-3380.

81. Jauffred, L.; Oddershede, L. B. Two-photon quantum dot excitation during optical trapping. *Nano Letters* 2010, 10, 1927-1930.

82. Pan, L.; Ishikawa, A.; Tamai, N. Detection of optical trapping of CdTe quantum dots by two-photon-induced luminescence. *Physical Review B* 2007, 75, 161305.

83. Chiang, W. Y.; Okuhata, T.; Usman, A.; Tamai, N.; Masuhara, H. Efficient optical trapping of CdTe quantum dots by femtosecond laser pulses. *The Journal of Physical Chemistry B* 2014, 118, 14010-14016.

84. Chen, Y. F.; Serey, X.; Sarkar, R.; Chen, P.; Erickson, D. Controlled photonic manipulation of proteins and other nanomaterials. *Nano Letters* 2012, 12, 1633-1637.

85. Tsuboi, Y.; Shoji, T.; Kitamura, N.; Takase, M.; Murakoshi, K.; Mizumoto, Y.; Ishihara, H. Optical trapping of quantum dots based on gap-mode-excitation of localized surface plasmon. *The Journal of Physical Chemistry Letters* 2010, 1, 2327-2333.

86. Zehtabi-Oskuie, A.; Jiang, H.; Cyr, B. R.; Rennehan, D. W.; Al-Balushi, A. A.; Gordon, R. Double nanohole optical trapping: dynamics and protein-antibody co-trapping. *Lab on a Chip* 2013, 13, 2563-2568.

87. Boyd, R. W. *Nonlinear Optics*. Academic Press: 2003.

88. Sheik-Bahae, M.; Hutchings, D. C.; Hagan, D. J.; Van Stryland, E. W. Dispersion of bound electron nonlinear refraction in solids. *IEEE Journal of Quantum Electronics* 1991, 27, 1296-1309.

89. Sutherland, R. L. *Handbook of nonlinear optics*. CRC Press: 2003.

90. Rumi, M.; Perry, J. W. Two-photon absorption: an overview of measurements and principles. *Advances in Optics and Photonics* 2010, 2, 451-518.

CHAPTER 2

Methods

This chapter describes both experimental and simulation methods employed in this dissertation. We begin by describing the nanofabrication techniques. We next describe our simulation methods. After that, we describe other aspects of experiments related to the optical microscope system in which the trapping is performed.

2.1 Nanofabrication

Two types of nanostructures are investigated in this dissertation: a double nanohole (DNH) aperture in a gold film, and an all-dielectric (silicon) nanoantenna on a silicon substrate. The DNH aperture devices are fabricated by Dr. Gediminas Gervinskas at the Melbourne Centre for Nanofabrication (MCN). The Si nanoantenna devices are fabricated by Dr. Wuzhou Song, a research fellow from Crozier's group.

A scanning electron micrograph (SEM) top-view image of a representative DNH aperture is shown in Figure 2.1a.[1] The DNH is milled into a 100 nm thick Au film on a 1 mm thick glass substrate with a 5 nm thick titanium adhesion layer (EMF Corp., TA134) using a focused ion beam (FIB) milling technique (FEI Helios Nanolab 600 Dual Beam FIB-SEM), with a ±10 nm fabrication tolerance. FIB milling provides a simple but accurate method for the fabrication of nanoapertures in metallic films and requires neither mask nor resist. A photograph of two samples is shown as Figure 2.1b. Our sample consists of a 10×10 array of DNH structures (Figure 2.1c). Each array consists of four 5×5 sub-arrays ("Q1"–"Q4"), between which there are gaps of 20 μm.

In each sub-array, DNH structures are formed in a square lattice (10 μm spacing, Figure 2.1c,d). Each DNH structure (Figure 2.1a) has two circular holes with diameters of ~ 100 nm, and a ~ 30 nm gap in between. The two circular holes are separated by ~ 140 nm for the centre-to-centre distance.

A number of different approaches have been explored for all-dielectric nanoantenna fabrication, including lithography technique, chemical vapor deposition technique, thin film dewetting technique, and laser-assisted methods (e.g., laser ablation and laser printing).[2] The most straightforward technique is lithography, with which many complex shapes have been demonstrated. The Si nanoantennas employed in this dissertation (see Figure 2.2a)[3, 4] are fabricated by standard electron beam lithography (EBL) and inductively coupled plasma reactive ion etching (ICP-RIE) on a Si wafer (Virginia Semiconductor Inc.). The resist used is ZEP520 (Zeon Chemicals). A photograph of a sample is provided as Figure 2.2b. After etching, the residual resist is removed, resulting in the silicon nanoantenna arrays (Figure 2.2c,d). EBL allows the writing of nanopatterns with very high resolution. Each sample consists of 3×3 arrays separated by gaps of 0.6 mm. Each array has an overall extent of ~ 50 μm, consisting of Si nanoantennas made in a square lattice (25×25 nanoantennas) with period 2 μm. Each nanoantenna (see SEM image in Figure 2.2a) consists of two identical Si cylinders separated by a gap of 50 nm. The cylinders have diameters of 200 nm and heights of 200 nm. They are surrounded by a Si ring and are situated on a Si substrate. The ring has inner and outer radii of 525 nm and 725 nm, respectively, and a height of 200 nm.

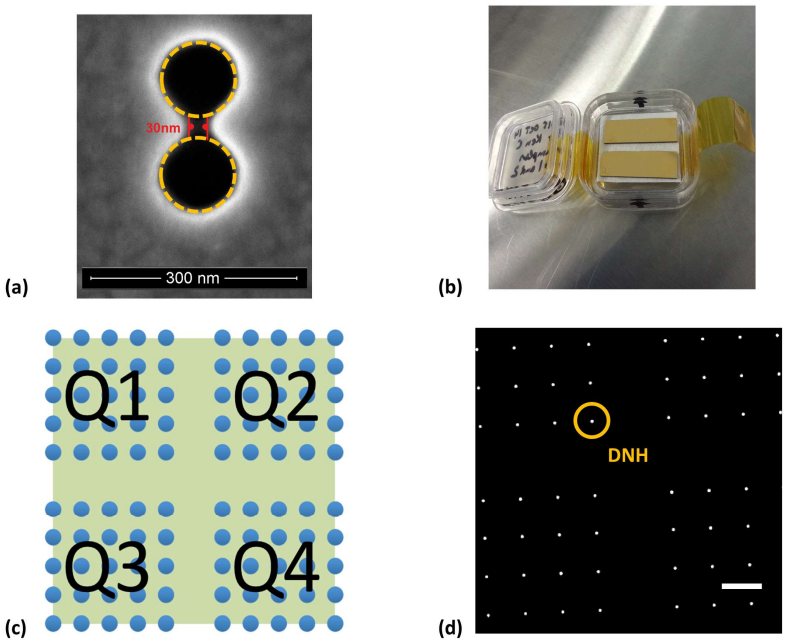

Figure 2.1. (a) SEM image of DNH aperture with a 30 nm gap. Circular holes are denoted by orange dashed lines. (b) Photograph of Au films with DNH arrays. (c) Schematic layout of DNH arrays. (d) Optical microscope image of DNH arrays immersed in water. Scale bar: 10 μm.

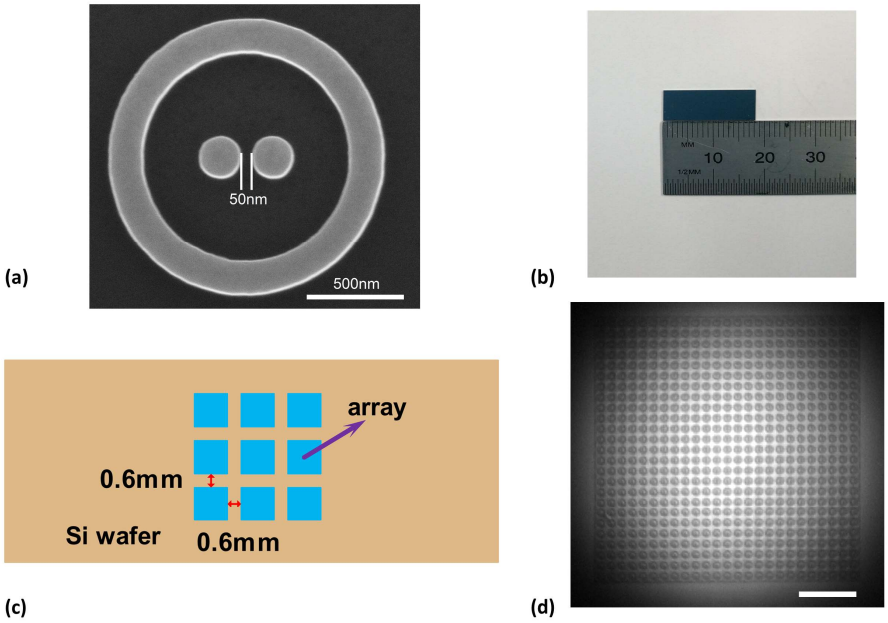

Figure 2.2. (a) SEM image of all-Si nanoantenna with a 50 nm gap. (b) Photograph of a Si wafer with nanoantenna arrays. (c) Schematic layout of Si nanoantenna arrays in wafer (each blue square indicates an array with 25×25 nanoantennas). (d) Microscope image of Si nanoantenna array chip immersed in water. Scale bar: 10 μm.

2.2 COMSOL simulation

Optical trapping processes involve not only the generation of near fields and optical forces, but also heat transfer from nanostructures to the surrounding environment. In this dissertation, comprehensive simulations are performed by the finite element method (FEM; COMSOL Multiphysics). COMSOL Multiphysics provides a powerful interaction environment for modelling many kinds of engineering and science problems. The key advantage is that COMSOL can be used to model a variety of physical phenomena in a coupled manner. The simulation procedure can be briefly described as follows: (1) select the study environment; (2) build or load geometrical objects; (3) specify material properties; (4) determine physics and boundary conditions; (5) create the mesh; (6) run the simulation; (7) postprocess results. In the simulation, creating the mesh is an important step. Normally, the smaller the mesh elements, the better the numerical accuracy, but the more the computational memory and simulation time needed. I performed all COMSOL simulations. In my study, different modules are selected for different purposes. I use the "Wave Optics Module" to determine the electromagnetic scattering (including nanostructures and nanoparticles), optical forces and the heat source power coming from light dissipation. Optical forces acting on the nanoparticle surface are determined using the Maxwell stress tensor method. I use the "PDE Module" (partial differential equation) to determine the trapping potential energy by solving the equation $-\nabla U = \vec{F}$. I use the "Conjugate Heat Transfer Module" to simulate the thermal coupling problem concerning the heat transfer and water flow (in steady states) in the microfluidic chamber. I use the "Particle Tracing Module" to simulate particle trajectories under the influence of different forces with very small solver time steps by performing Langevin equation simulations. More modelling details

are given in Chapter 3 for the DNH trapping work and in Chapters 4 and 5 for the Si nanoantenna trapping work.

2.3 Experimental methods

Microfluidic chamber preparation: The microfluidic chamber (4 mm × 16 mm area, width 1 mm) is formed from photoresist on a 150 μm thick microscope glass coverslip (Figure 2.3a) using standard photolithography methods. The process starts with the glass coverslip (VWR, Square, No.1) being sonicated in water, baked on a hot plate to dry it, and cleaned in an oxygen plasma cleaner (Diener electronic) to remove particles etc. from its surface. This is followed by photoresist (AZ 9260) coating, photolithography (Quintel Mask Aligner Q4000-6) and development (AZ 400K Developer 1:4). The photoresist thickness is determined by the rotation speed of the spin coater and measured with an optical profilometer. The photoresist is first applied to the cleaned coverslip while the latter is rotating at 500 rpm over a time interval of 10 s to allow it to spread. The coverslip is then spun at a designated speed for 60 s to obtain the required photoresist thickness. For the DNH work, the designated speed is 600 rpm, which yields a photoresist thickness of ~ 20 μm. For the Si nanoantenna work, the speed is 1000 rpm, yielding a thickness of ~ 15 μm. That the chamber is relatively shallow facilitates the fluorescence observations performed in this dissertation. Two holes are drilled into the sample (Au film on glass or Si chip) to allow tubing to be added later. The sample (Au film on glass or Si chip) is then washed with acetone and rinsed with isopropanol and water. It is then glued to the glass coverslip containing the microfluidic chamber using UV-cured optical adhesive (Thorlabs, Inc., NOA63), resulting in the chamber being closed (Figure 2.3b). Polyethylene tubing (Fisher Scientific, BD 427406) is used to deliver fluids into the channel.

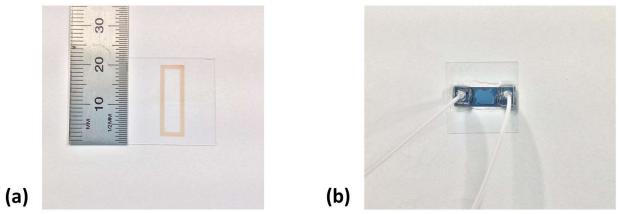

Figure 2.3. Photograph of (a) a microfluidic chamber and (b) a Si chip sample package.

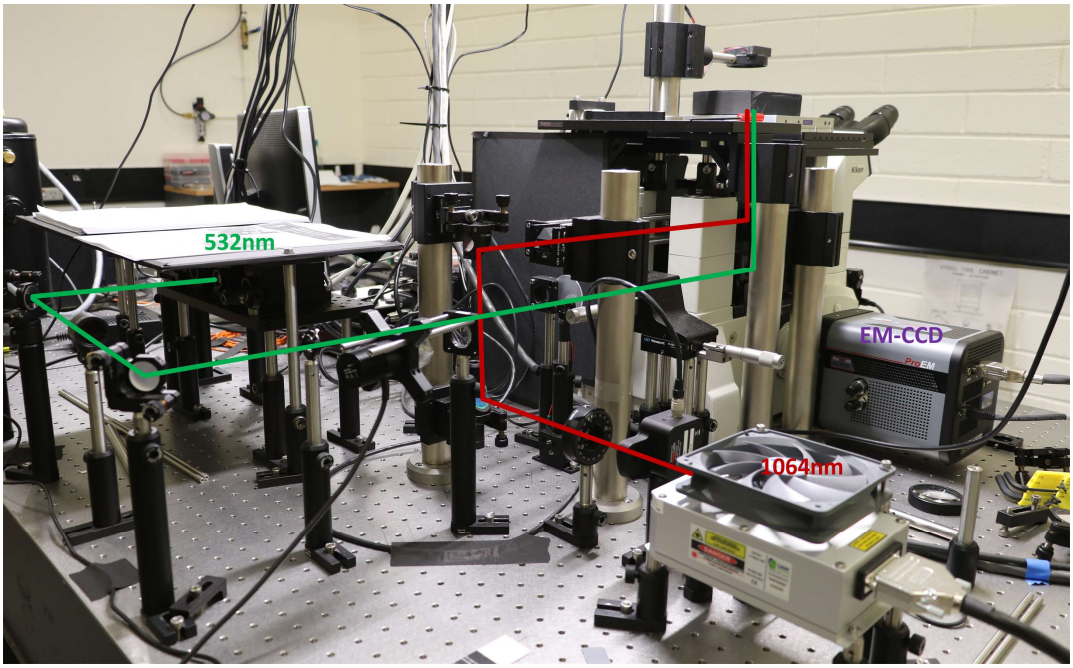

Figure 2.4. Photograph of the experimental setup showing two lasers and their optical paths.

Optical trapping setup: Our experimental setup (Figure 2.4) includes a series of components: a continuous wave near-infrared trapping laser (CW, Laser Quantum Ventus 1064); a green laser for fluorescence excitation (DPSS Laser, LSR532NL-500); an oil immersion microscope objective (Nikon Plan Fluorite Oil Immersion Objective, 100×, NA = 1.3); nanostructures in microfluidic systems (4 mm × 16 mm, ~ 20 μm or 15 μm); a sensitive electron multiplying camera (EM-CCD, ProEM-HS: 512×512, Princeton Instruments); a grating spectrometer (SpectraPro 2300i, Acton). The setup was originally built by Dr. Wuzhou Song, a research fellow in Crozier's group, though I made modifications to it. The wavelength of the trapping laser (1064 nm) is a very

common choice for optical tweezers, as it results in low photodamage. The nanoparticles (fluorescent polystyrene NSs: F8784 and F8800, carboxylate-modified; QDs: Q10121MP, streptavidin-coated) are purchased from Life Technologies. The polystyrene NSs are suspended in distilled water, and the QDs are suspended in phosphate-buffered saline solution (1X PBS, pH 7.4). A trace amount of the surfactant Tween 20 (Life Technologies) is added to the solution to prevent aggregation. We use a low autofluorescence immersion oil with a refractive index of n = 1.518 (Olympus Type F). The experimental setup is based on an inverted optical microscope (Nikon Eclipse TE2000). The optical trapping process is monitored by observing the wide-field fluorescence imaging after a set of filters (dichroic mirrors and two 750 nm shortpass filters). The EM-CCD camera is used to track the position of the nanoparticles (and light emission) as a function of time. The EM-CCD camera is operated at 30 frames per second (fps) with an exposure time of ~ 30 ms. Each pixel on the EM-CCD sensor array is 16 μm × 16 μm, which translates to around 160 nm × 160 nm at the sample plane with the 100× magnification objective. Our setup also includes an optical shutter (Thorlabs, Inc.), a half-wave plate (wavelength 1064 nm, Thorlabs, Inc.), optical diffusers, and a piezoelectric stage. Schematic diagrams of the setup are also provided in later chapters of this dissertation.

The input trapping laser power P_0 is measured before the objective (i.e., removing the objective) using a power meter (Thorlabs, Inc., S121C). The diffraction-limited beam spot diameter (i.e., $1/e^2$ intensity diameter) is a function of the wavelength (λ) and the numerical aperture (NA) of the objective lens and is approximately given by:

$$d_{diffraction} = \frac{1.22\lambda}{NA} \tag{2.1}$$

In the experiments, we assume that the laser is nearly diffraction limited and has a spot diameter d of ~ 1.2 μm, which is larger than the diffraction-limited spot (~ 1 μm). The trapping laser intensity at the sample is then calculated as:

$$I_0 = \frac{4P_0 \bullet T_{obj}}{\pi d^2} \tag{2.2}$$

where T_{obj} is the transmission of the objective at a wavelength of 1064 nm.

References

1. Xu, Z.; Song, W.; Crozier, K. B. Direct particle tracking observation and Brownian dynamics simulations of a single nanoparticle optically trapped by a plasmonic nanoaperture. *ACS Photonics* 2018, 5, 2850-2859.

2. Baranov, D. G.; Zuev, D. A.; Lepeshov, S. I.; Kotov, O. V.; Krasnok, A. E.; Evlyukhin, A. B.; Chichkov, B. N. All-dielectric nanophotonics: the quest for better materials and fabrication techniques. *Optica* 2017, 4, 814-825.

3. Xu, Z.; Song, W.; Crozier, K. B. Optical Trapping of Nanoparticles Using All-Silicon Nanoantennas. *ACS Photonics* 2018, 5, 4993-5001.

4. Xu, Z.; Crozier, K. B. All-dielectric nanotweezers for trapping and observation of a single quantum dot. *Optics Express* 2019, 27, 4034-4045.

CHAPTER 3

Direct particle tracking observation and Brownian dynamics simulations of a single nanoparticle optically trapped by a plasmonic nanoaperture

This chapter is originally published in ACS Photonics:

Zhe Xu, Wuzhou Song, and Kenneth B. Crozier. Direct particle tracking observation and Brownian dynamics simulations of a single nanoparticle optically trapped by a plasmonic nanoaperture. ***ACS Photonics*** **2018**, 5, 2850–2859.

ACS Photonics

Article

Cite This: ACS Photonics 2018, 5, 2850−2859

Direct Particle Tracking Observation and Brownian Dynamics Simulations of a Single Nanoparticle Optically Trapped by a Plasmonic Nanoaperture

Zhe Xu,[†] Wuzhou Song,[†,‡] and Kenneth B. Crozier*[,†,§]

[†]School of Physics, University of Melbourne, Victoria 3010, Australia

[‡]School of Materials Science and Engineering, Huazhong University of Science and Technology, Wuhan 430074, People's Republic of China

[§]Department of Electrical and Electronic Engineering, University of Melbourne, Victoria 3010, Australia

Supporting Information

ABSTRACT: Optical trapping using plasmonic nanoapertures has proven to be an effective means for the contactless manipulation of nanometer-sized particles under low optical intensities. These particles have included polystyrene and silica nanospheres, proteins, coated quantum dots and magnetic nanoparticles. Here we employ fluorescence microscopy to directly observe the optical trapping process, tracking the position of a polystyrene nanosphere (20 nm diameter) trapped in water by a double nanohole (DNH) aperture in a gold film. We show that position distribution in the plane of the film has an elliptical shape. Comprehensive simulations are performed to gain insight into the trapping process, including of the distributions of the electric field, temperature, fluid velocity, optical force, and potential energy. These simulations are combined with stochastic Brownian diffusion to directly model the dynamics of the trapping process, that is, particle trajectories. We anticipate that the combination of direct particle tracking experiments with Brownian motion simulations will be valuable tool for the better understanding of fundamental mechanisms underlying nanostructure-based trapping. It could thus be helpful in the development of the future novel optical trapping devices.

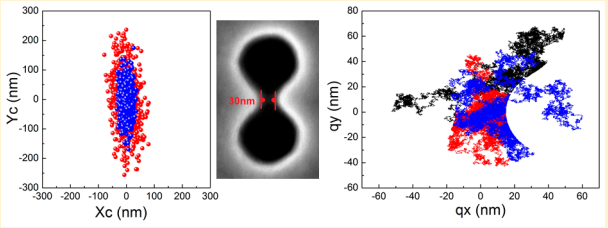

KEYWORDS: *optical trapping, particle tracking, double nanohole, fluorescence microscopy, Brownian motion*

The use of optical forces for the acceleration and trapping of micrometer-sized particles was first demonstrated by Arthur Ashkin in 1970.[1] It was later shown that a single tightly focused laser beam, termed optical tweezers, could be used to trap, transport, and manipulate particles, and many applications in the biological and physical sciences have been introduced.[2−5] In conventional optical tweezers, particles are trapped using the gradient forces exerted by laser beams focused with lenses. For the trapping of very small particles (tens of nanometers), however, these face challenges, because the forces are roughly proportional to particle volume.[6] A consequence is that the field intensity must be increased to maintain trap stability to overcome the strong Brownian motion, but this can result in undesired thermal effects. Furthermore, in conventional optical tweezers, a lower bound on the focal spot size is set by the diffraction limit. This determines the precision with which an object can be trapped.

To circumvent the limitations for trapping smaller objects with conventional optical tweezers, the use of nanotweezers based on plasmonics[7−20] and other approaches, such as waveguides,[21,22] ring resonators,[23,24] and photonic crystal resonators,[25,26] has recently attracted keen interest. Plasmon-based optical nanotweezers can provide nanoscale local field enhancement and strong optical forces, and plasmonic nanoapertures have been of particular interest. Kwak et al. demonstrated the trapping of fluorescent nanospheres (200 nm diameter) using a nanoaperture in a gold film.[7] The trapping process was monitored by recording the transmission through the nanoaperture of the fluorescent emission from the nanosphere as a function of time.[7] Juan et al. demonstrated the trapping of 50 nm polystyrene beads with a nanoaperture.[10] The trapping process was monitored by recording the transmission of the infrared trapping laser through the nanoaperture as a function of time.[10] Other notable nanoaperture works include reports of the trapping of beads with diameters of 12 nm,[14] trapping using rectangular nanopore apertures,[15] trapping using nanoapertures at the ends of optical fibers,[16] the trapping of proteins and other biomolecules,[17] and fundamental studies on the trapping process,[18] namely on the role played by the nanoparticle being trapped in modifying the cavity resonance and thus the optical forces. We argue, however, that the direct observation of the dynamics of trapped nanoparticles (NPs), that is, position as a function of time, could greatly assist the understanding and further development of optical nanotweezers. To the best of our knowledge,

Received: February 8, 2018
Published: May 30, 2018

DOI: 10.1021/acsphotonics.8b00176
ACS Photonics 2018, 5, 2850−2859

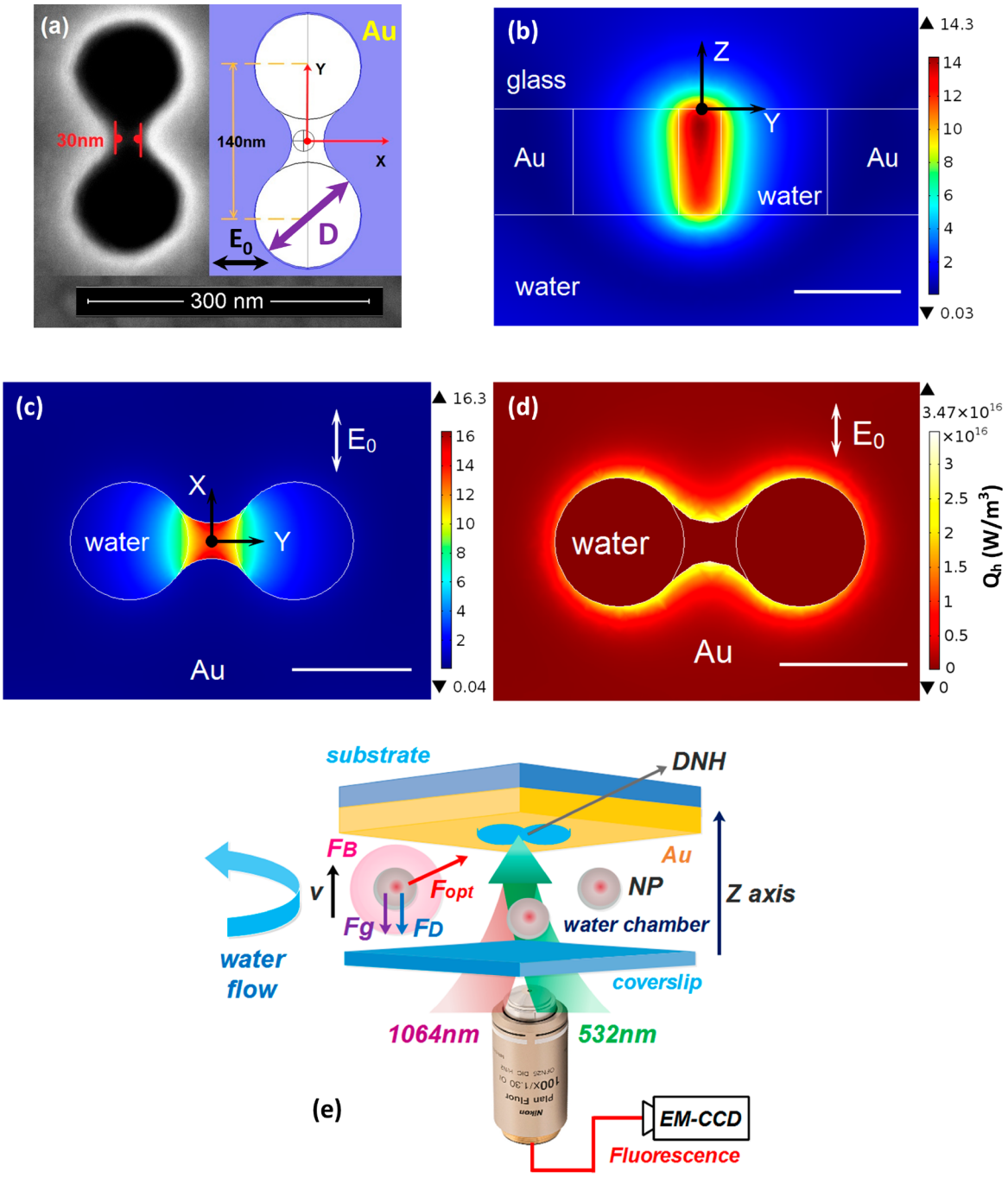

Figure 1. (a) DNH aperture in Au film: LEFT-top-view image of scanning electron micrograph (SEM), RIGHT-simulated structure, comprising two circular holes (diameter D = 100 nm) separated by 140 nm (center-to-center) with 30 nm gap. (b, c) Electric field enhancement ($|E|/|E_0|$) distribution, for plane wave illumination from water side (x-polarized, λ = 1064 nm, traveling in +z direction). Black dot indicates coordinate system origin. (b) x = 0 cross section; (c) z = −50 nm cross section. (d) Heat power dissipation density (Q_h) in the center plane (z = −50 nm) for I_0 = 6.67 mW/μm^2. Scale bar is 100 nm in (b)−(d). (e) Schematic illustration of 20 nm NPs optically trapped in the near fields of a DNH in water chamber. Fluorescence is recorded by EM-CCD camera. Sketch is not to scale. Definitions of symbols are as follows. v: NP velocity; F_B: Brownian force; F_g: gravity with buoyancy; F_D: drag force; F_{opt}: optical trapping force. Note that the directions of the forces as depicted in this figure are examples for illustration purposes.

however, this has not been demonstrated in previous reports of the nanoaperture trapping (e.g., refs 7, 10, and 14−18). Rather, the trapping process in these reports was monitored by measuring the optical transmission (of trapping laser or of fluorescence from the trapped object) through the nanoaperture as a function of time. Step-like increases in transmission were observed, with each step interpreted as being due to the trapping of an individual nanoparticle. However, the information on trapping dynamics that experimental data sets comprising transmission vs time can provide is limited compared to what can be obtained with direct imaging.

In this work, we employ fluorescence microscopy to track the position of a polystyrene nanosphere (20 nm diameter) trapped

DOI: 10.1021/acsphotonics.8b00176
ACS Photonics 2018, 5, 2850−2859

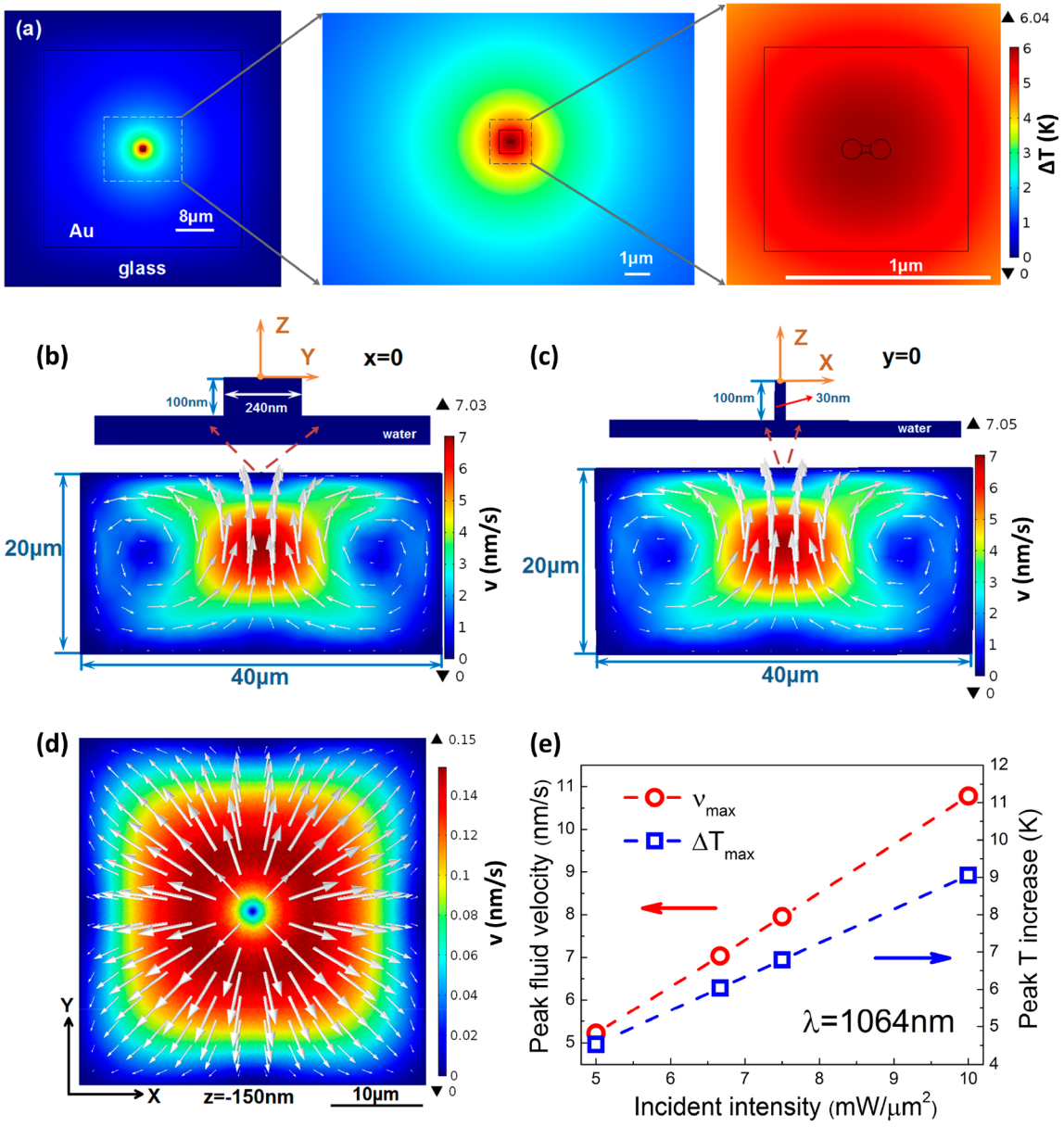

Figure 2. (a) FEM simulation of steady-state temperature increase (ΔT) profile around DNH for illumination intensity I_0 = 6.67 mW/μm^2, plotted in a cross-section through the DNH center (z = −50 nm). (b–d) FEM simulations of water convection velocity field for I_0 = 6.67 mW/μm^2, plotted in both magnitude (color map: nm/s) and direction (white arrows, magnitude proportionally scaled). (b) x = 0 cross section; (c) y = 0 cross section; (d) z = −150 nm cross section (i.e., at distance of 50 nm below gold film surface). (e) Peak temperature increase (ΔT_{max}: K, blue squares) and maximum convection velocity (ν_{max}: nm/s, red circles) as a function of trapping laser intensity.

by a double nanohole (DNH) aperture in a gold (Au) film. This allows us to determine the spatial confinement of the trapped particle, that is, its position distribution, which was not possible with previous reports of nanoaperture trapping, in which transmission versus time was monitored.[7,10,14−18] Our results show that the measured position distributions have elliptical shapes and that tighter spatial confinement occurs at the higher laser intensity. We present comprehensive three-dimensional finite-element method (FEM; COMSOL Multiphysics) simulations of the dynamics of the trapping process that combine optical modeling with Brownian motion, gravity, and fluid dynamics (Stokes drag). The simulations emphasize the important role of the morphology of the DNH structure in the trapping process. The simulations furthermore provide information inaccessible with our experiments, predicting nanoparticle trajectories in three dimensions and on subnanosecond time scales. Our simulations also indicate that the DNH yields enhanced optical forces and potential energy, but with only modest temperature increases from Joule heating due to the good thermal conductivity provided by the gold film.[19,20,27] We anticipate that the combination of the direct experimental observation of the dynamics of trapped particles with comprehensive multiphysics simulations will be a powerful means for better understanding optical trapping with plasmonic and photonic nanostructures.

Figure 1a shows a scanning electron micrograph (SEM) top-view image of the DNH. The DNH is milled into a 100 nm thick Au film on a 1 mm thick glass substrate with a 5 nm titanium adhesion layer (EMF Corp., TA134) using a focused ion beam tool (FEI Helios Nanolab 600 Dual Beam FIB-SEM).

DOI: 10.1021/acsphotonics.8b00176
ACS Photonics 2018, 5, 2850−2859

Each circular hole in the DNH has a diameter of ∼100 nm. The circular holes are separated by ∼140 nm (center-to-center). We refer to the pointed features of the narrowest constriction of the DNH as the "tips". These are separated by ∼30 nm. The simulated structure is chosen with the goal of matching the geometrical parameters measured from the SEM. The region of the gold film between the holes is open, and is defined by two arcs (also referred to as tips, as discussed above) whose closest separation is 30 nm. Further details on the simulations are provided in the Supporting Information. The glass substrate on which the gold film (containing the DNH) is formed is taken as having a refractive index of $n_{glass} = 1.45$. The superstrate is water ($n_{water} = 1.33$). The complex-valued relative permittivity of the gold is taken as $\varepsilon_r = -48.45 - i3.6$, which is appropriate for the wavelength of the trapping laser.[28] Plane wave illumination (x-polarized, $\lambda = 1064$ nm) is incident from the water side, traveling in $+z$ direction. This results in highly confined electric fields in the DNH through the excitation of surface plasmon polaritons (SPPs). Indeed, as shown in Figure 1b,c, for which no NPs are present, the electric field enhancement ($|E|/|E_0|$) is as large as ∼16.3×, which is defined by comparing the electric field amplitude with ($|E|$) and without ($|E_0|$) the gold film (containing the DNH). The field enhancement is largest within the gap between the tips and around the bottom of the DNH (i.e., at the glass side) when the incident field is polarized across the gap (x-axis). In Figure 1d, we plot the power dissipation density (Q_h) in a plane halfway through the DNH at the illumination intensity we use in experiments ($I_0 = 6.67$ mW/μm^2). Due to the large imaginary part of the relative permittivity of gold, most of the power dissipation is concentrated in the gold near the surface of the DNH, and is small elsewhere. The power dissipation density profile also strongly depends on the DNH geometry and is highly nonuniform. Figure 1e schematically illustrates our experimental setup, with further details provided in the Supporting Information. The sample is mounted upside-down and aligned using a piezoelectric stage with a subnanometer position resolution. The trapping is monitored by observing the NP fluorescence. An x-polarized laser beam ($\lambda = 1064$ nm) is focused by an oil immersion objective (100×, NA = 1.3) into a ∼20 μm thick perfusion chamber containing distilled water (UltraPure DNase/RNase-Free), polystyrene NPs ($n_{NP} = 1.6$, FluoSpheres, 20 nm diameter, carboxylate-modified, Nile Red, Life Technologies) and a trace amount of surfactant (Tween 20, 0.05% v/v). The spot size is ∼1.2 μm. A loosely focused green laser beam ($\lambda = 532$ nm) is projected along the same optical path to excite fluorescence, which is imaged onto a sensitive electron multiplying camera (EM-CCD, ProEM-HS: 512 × 512, Princeton Instruments) operated at a frame rate of 30 frames per second (fps). The input intensity of the green laser is significantly weaker than that of the trapping laser and is therefore expected to produce negligible optical forces. Each pixel on the EM-CCD sensor array is 16 μm × 16 μm, which translates to 160 nm × 160 nm in the sample plane with the 100× magnification objective.

Joule heating can have a substantial effect in plasmonic trapping, resulting in often undesired temperature increases of the plasmonic nanostructure, the trapped object (e.g., NP) and the water.[29,30] The temperature rise can furthermore result in substantial thermophoresis and thermal-induced fluid convection.[31−33] When a DNH is illuminated by a trapping laser, heat is generated in response to the absorbed power (Figure 1d) and released to the surroundings. Since thermal processes in metals are fast,[33] a steady state is rapidly reached, producing a temperature gradient and buoyancy-driven natural convection in the chamber.[20,27,33] We carry out numerical simulations of the temperature distribution and convection velocity field of the surrounding water for a DNH on glass substrate illuminated at a wavelength of 1064 nm. These simulations combine optics with thermodynamics and hydrodynamics,[33] and further details are provided in the Supporting Information. Key results are provided as Figure 2. As shown in Figure 2a, a maximum temperature rise (ΔT) of ∼6 K is predicted for illumination at the intensity used in experiments ($I_0 = 6.67$ mW/μm^2). The temperature distribution is very uniform around the DNH. Near the DNH, the strong heat source density leads to the temperature being high, while far from the DNH, the heat source is weaker, and the Au film is close to its initial temperature (i.e., without illumination, prescribed $T_0 = 293.15$ K). Since gold has much higher thermal conductivity than glass and water ($\kappa_{Au} \sim 317$ W K^{-1} m^{-1}, $\kappa_{glass} \sim 1$ W K^{-1} m^{-1}, $\kappa_{water} \sim 0.58$ W K^{-1} m^{-1}),[34] the heat generated by optical absorption near the DNH surface is readily conducted into the surrounding gold film, rather than into the water or the substrate. In other words, the gold film acts as a heat-sink[19,20] and helps reduce localized heating. This contrasts with isolated nanoantennas, for which strong illumination can result in reshaping and melting.[19,27,29,33] In Figure 2b−d, the simulated thermal-induced convection flow distributions are plotted on various cross sections. Both magnitude (color map: nm/s) and direction (white arrows, magnitude proportionally scaled) are shown. It can be seen that the water circulates upward and outward in a radially symmetric pattern and the fluid velocity near DNH surface is zero (see top panels of Figure 2b,c). This buoyancy-driven natural convection pattern is known as Rayleigh-Benard-like fluid convection.[32,33] The simulations predict a maximum velocity of ∼7 nm/s in the 20 μm thick water-filled chamber, for illumination of the single DNH at an intensity of $I_0 = 6.67$ mW/μm^2. This velocity is very small. We thus conclude that thermal-induced fluid convection is weak and has negligible contribution[33] to the DNH trapping process in these experiments. At the start of a trapping experiment when the trapping laser is turned on, only NPs that are very close to the DNH can be trapped, due to the optical forces being short-range in nature. Before this, the motion of the NPs is mainly driven by stochastic Brownian diffusion. Our simulations predict that the fluid velocities resulting from heating due to optical power absorbed by the DNH structure will be very small. On the other hand, in some applications, high fluid velocities are desired and several recent works have demonstrated methods for increasing it substantially. Specifically, it was shown that by introducing an optically absorptive and thermally conductive indium−tin-oxide (ITO) substrate[35] or a photothermal induced electrothermoplasmonic (ETP) flow,[36,37] high fluid velocities of ∼μm/s can be achieved. In Figure 2e, the peak temperature increase and maximum convection velocity are plotted as a function of the trapping laser intensity.

If a NP moves close to an illuminated DNH, for example, by Brownian motion, it will experience optical forces and can be trapped. To gain insight into the three-dimensional distribution of these optical trapping produced by a DNH, we perform FEM simulations to find the fields and use the Maxwell stress tensor (MST) method to find the forces.[38−40] We introduce a polystyrene NP ($n_{NP} = 1.6$) at a certain point (x, y, z), compute the electric and magnetic fields on its surface, and determine

DOI: 10.1021/acsphotonics.8b00176
ACS Photonics 2018, 5, 2850−2859

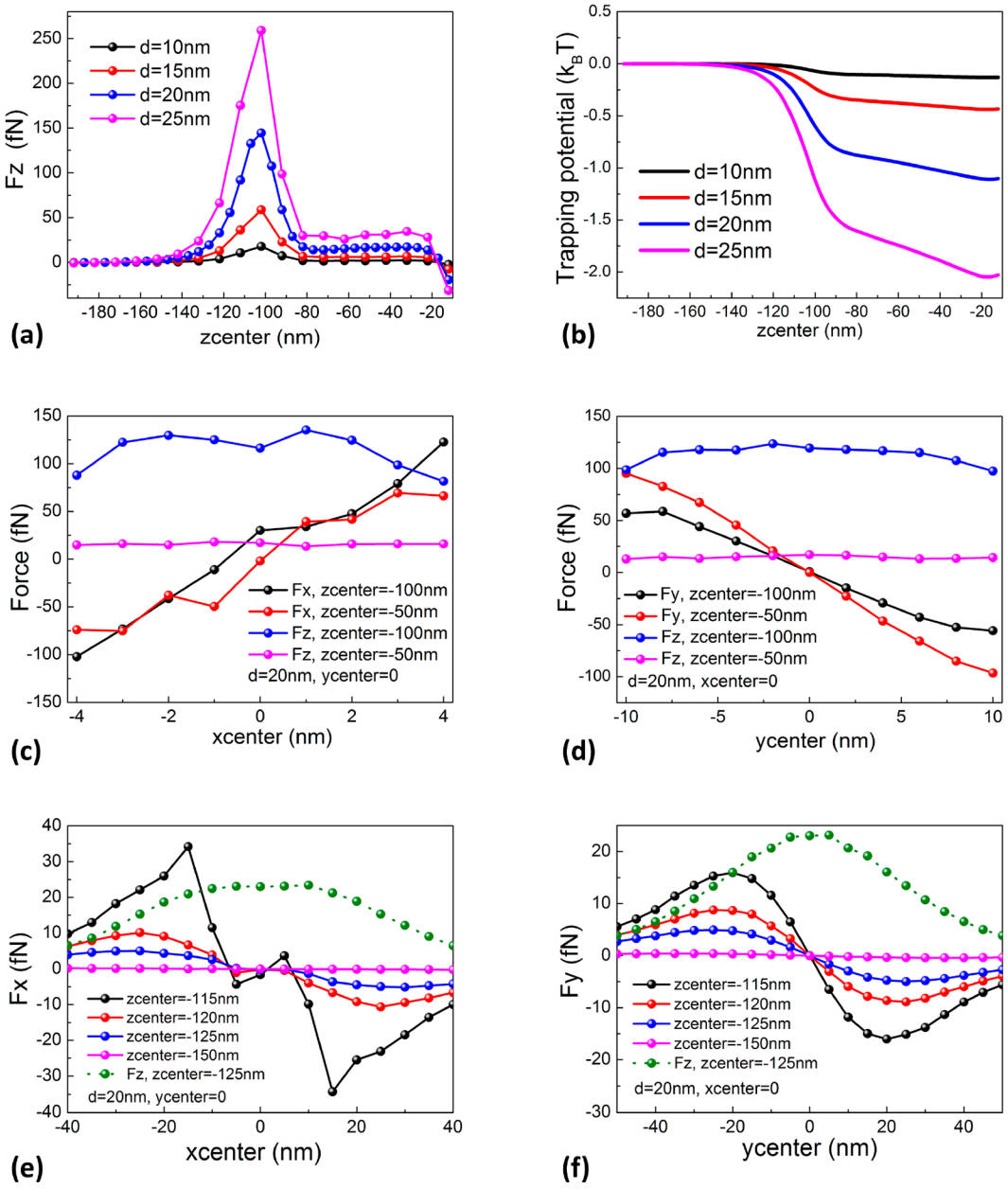

Figure 3. Map of optical forces exerted on a single polystyrene nanoparticle (n = 1.6) near DNH for I_0 = 6.67 mW/μm^2, calculated with Maxwell stress tensor (MST) method. (a) Vertical force F_z and (b) trapping potential energy U_z as functions of particle diameter d and position (x_{center} = y_{center} = 0). (c–f) Force map exerted on d = 20 nm NP. (c, e) y_{center} = 0; (d, f) x_{center} = 0.

the three components (x, y, and z) of the time-averaged force with the MST[41] (see Supporting Information). This process is repeated over a grid of coordinates for the sphere center position to obtain the force field map. In Figure 3a, we plot vertical force F_z as a function of NP center position along the z-axis, for (x_{center}, y_{center}) = (0, 0). It can be seen that the NP is pulled into the DNH (F_z is positive) except when very close to glass surface (F_z < 0) and that force increases with the NP diameter d. Although the three-dimensional optical force field on the particle is not necessarily strictly conservative, by constraining the motion of the particle to one dimension, an effective trapping potential energy can be introduced.[40,42] This quantity U_z is plotted as Figure 3b, and is found from Figure 3a by path integration along the z-axis, from outside of the hole (z_{center} = −192 nm, U_z = 0) to inside of the hole (z_{center} = −12 nm). While multiphysics simulations that combine optics with thermodynamics and hydrodynamics are needed for a detailed understanding of the trapping process (and are presented later), the effective trapping potential energy calculated in this way provides useful physics insight. Namely, it can be seen from Figure 3b that one should expect the force provided by the DNH trap should be sufficient to trap NPs against Brownian motion at the illumination intensity used (I_0 = 6.67 mW/μm^2). This conclusion is reached by the observation that the calculated trapping potential energy near substrate surface (i.e., glass/water interface) is larger than thermal energy ($1k_BT$ = 4.1 × 10^{-21} J, where k_B is Boltzmann constant and T = 300 K is temperature). In Figure 3c, we plot F_x and F_z as functions of NP position along the x-axis, with y_{center} = 0 nm, and z_{center} = −50 or −100 nm. The positive values of F_z confirm that the NP is pulled into the DNH. It can also be seen that F_x is positive (negative) when x_{center} is positive (negative). While F_x = 0 at

DOI: 10.1021/acsphotonics.8b00176
ACS Photonics 2018, 5, 2850–2859

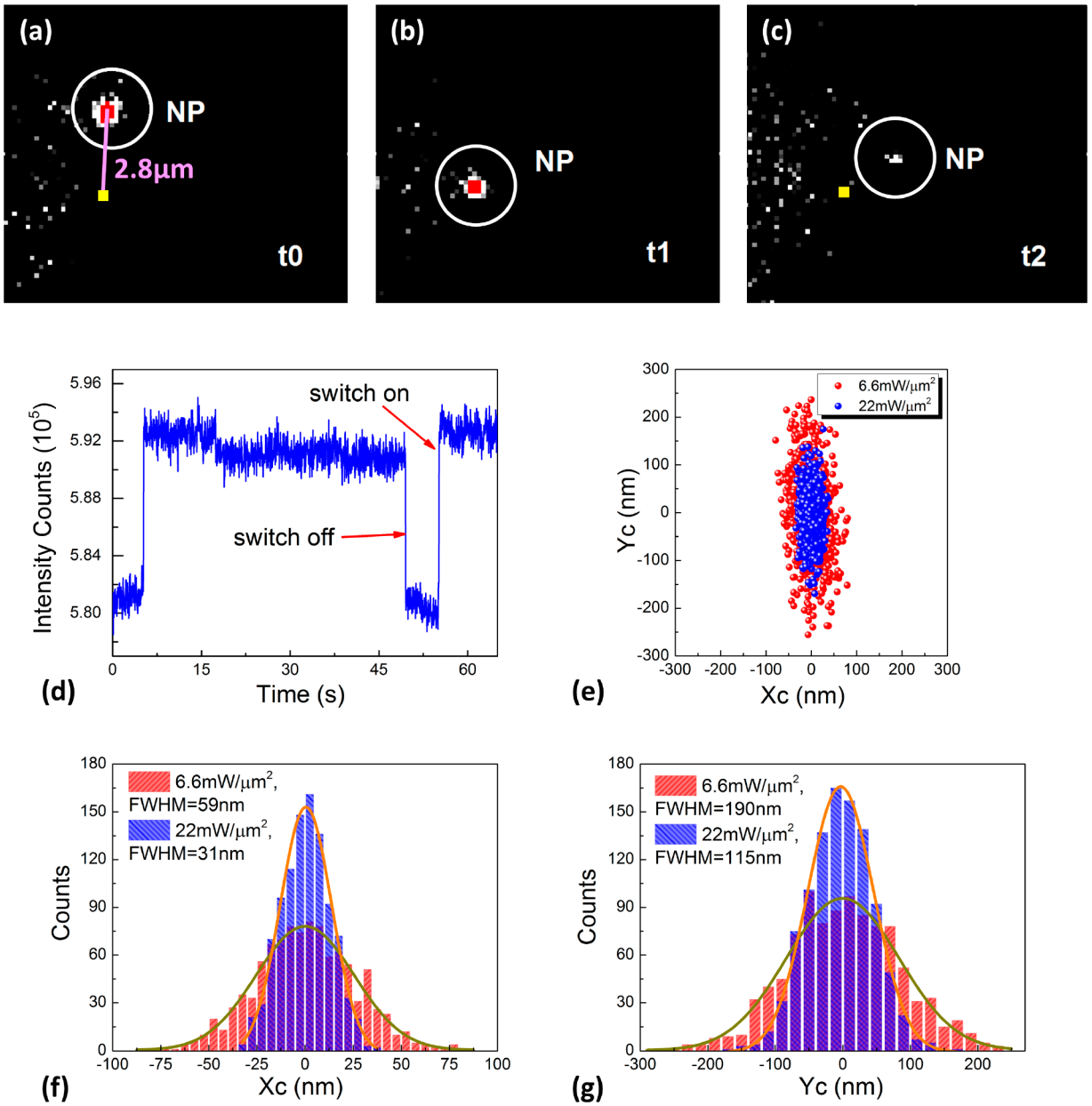

Figure 4. (a–c) EM-CCD frames showing optical trapping and release of a single 20 nm NP by DNH (approximately position: yellow dot). I_0 = 16 mW/μm^2. (d) Optical trapping of a single 20 nm NP seen as sudden discrete jumps in fluorescence intensity. I_0 = 22 mW/μm^2. (e) Scatter plots of NP center locations. (f, g) Position histograms along x- and y-axes, extracted from data of (e).

x_{center} = 0 and z_{center} = −50 or −100 nm, these positions do not allow stable trapping because displacement of the NP from x_{center} = 0 does not result in a restoring force to pull the NP back to x_{center} = 0. This indicates that NP is predominantly pulled to the sides of the DNH gap edge (30 nm wide), to the positions denoted by red dots in Figure 1a. In Figure 3d, we plot F_y and F_z as functions of NP position along the y-axis, with x_{center} = 0 nm and z_{center} = −50 or −100 nm. The positive values of F_z again confirm that the NP is pulled into the DNH. It can also be seen that F_y is positive (negative) when y_{center} is negative (positive). This indicates that the NP experiences a restoring force for excursions in the y-direction from the DNH center (y = 0) and a stable equilibrium is produced at the center in the y-direction. In Figure 3e,f, we plot the transverse forces F_x and F_y as functions of NP center position along the x- and y-axes, respectively. The calculations are performed for various vertical cross sections that are away from the DNH surface (i.e., z = −100 nm plane). The F_x pulling strength to the side walls (indicated in red dots in Figure 1a) diminishes with distance from DNH surface. This is especially evident from examination of the central part of Figure 3e. Again, the NP experiences a restoring force in the y-direction (Figure 3f) and is pulled into the DNH due to the positive values of F_z (Figure 3e,f). We also note from Figure 3e that the NP experiences a restoring force in the x-direction when it is outside of the hole. More optical forces maps can be found in the Supporting Information.

To study the trapping process experimentally, we employ fluorescence microscopy to visualize optical trapping and track the position of a polystyrene nanosphere with a diameter of 20 nm trapped by a DNH. We add a trace amount of surfactant (Tween 20, 0.05% v/v) to the particle solution to limit adhesion to the surface and use a bath sonicator to further

DOI: 10.1021/acsphotonics.8b00176
ACS Photonics 2018, 5, 2850–2859

prevent aggregation. The particle solution contains the nanospheres at 0.02% solids. Before the experiments, distilled water with Tween 20 (0.05% v/v) is flowed through the channel to prevent nonspecific binding. After the experiment is initiated, we usually wait for about 10 to 20 min for a NP to be trapped. Three EM-CCD frames are shown as Figure 4a–c, showing a few steps in the NP trapping and release process (see also Supporting Information, Movie 1). At time t_0, the NP moves randomly and is ∼2.8 μm from the DNH. From time t_1, the NP is stably trapped for ∼34 s. At time t_2, it is no longer trapped. To illustrate and analyze the optical trapping process, we plot the fluorescence intensity integrated over a 30 × 30 pixel cross section centered over the illuminated DNH as a function of time. As shown in Figure 4d, at $t \sim 6$ s, the NP enters the DNH vicinity and becomes trapped, resulting in an abrupt jump (step-like) in fluorescence. At $t \sim 49$ s, the trapping laser is turned off and the NP is released. Turning the laser on at $t \sim 55$ s results in the NP being trapped again. That the NP is trapped when the laser is on and released when it is off confirms the predominant role of optical forces in the trapping process and that the NP is not attached to the surface just by van der Waals force, etc. It can be seen from Figure 4d that blocking the laser (at $t \sim 49$ s) results in quick release of the NP from the trap. We also verify that the NP is less strongly trapped (larger positional fluctuations) when the laser power is reduced or the polarization is rotated. Note that the NP in Figure 4d is not the same NP as that in Figure 4a–c. To assess the trapping more quantitatively, we determine the trapped NP center positions from 1000 EM-CCD frames using a radial-symmetry-based particle localization algorithm[43] over an interval of 33 s for two different illumination intensities (Figure 4e). In Figure 4f,g, we plot the measured NP center positions (x_c and y_c) as histograms. The full-widths-at-half-maximum (fwhms) of fitted Gaussian distributions are 59 and 190 nm along the x- and y-directions when the illumination intensity is 6.6 mW/μm^2 (see Supporting Information, Movie 2). When the illumination intensity is 22 mW/μm^2, the fwhms are 31 and 115 nm along the x- and y-directions, respectively. It can be seen that there is suppression of Brownian motion at the higher laser intensity. Also, at both intensities, DNH results in the NPs being confined in an elliptical region, where the position histograms are narrower along the x-direction than the y-direction. This anisotropy can be ascribed to the near field being more strongly confined along the x-direction than the y-direction (see Figure 1c). In addition, the trapped NP experiences the steric hindrance from DNH edge in x-direction rather than in y-direction. To obtain experimental trapping stiffness for a rough estimate, we determine the "effective" trapping stiffness ($k_{\text{eff}} = k_B T/\text{var}(x)$, var($x$) is the position variance) for the illumination intensity of 6.6 mW/μm^2. This is extracted from the measured variance of position (determined from fwhms in Figure 4f,g) and correction function using the method of ref 44 that accounts for video-image motion blur over a finite integration time. The successive grayscale images for tracking are recorded with an ∼30 ms exposure time. This yields trapping stiffnesses in the x- and y-directions of k_x = 0.2625 fN/nm and k_y = 0.0801 fN/nm, respectively, that is, k_x is about 3× larger than k_y.

We next investigate the trapping process further by performing Langevin equation simulations to predict the motion of a NP in the vicinity of a DNH under the influence of Brownian fluctuation (stochastic) and DNH generated optical forces (deterministic).[45] These simulations combine optical forces with Brownian motion, gravity and fluid dynamics (Stokes drag). While even the early works on plasmonic trapping identified the possible role of heating (as well as other nonoptical forces) on the trapping process,[41,46] the simulations of Figure 2 predict that the peak value of the fluid velocity is only ∼7 nm/s. We thus do not include heating-driven convection velocity fields in these simulations. Volpe and Volpe previously simulated the motion of a particle in an optical trap,[47] but this approach would be unsuitable for our DNH, as a constant stiffness value was assumed whereas the DNH provides highly confined field distribution (see Figure 1b,c). Furthermore, steric hindrance (i.e., DNH gap and edge) plays an important role in the trapping.[14] We thus write the Langevin equation as given by eq 1 below (see also Figure 1e and Supporting Information), where m_p is the mass of the NP. The drag force ($\vec{F}_D$, see, e.g., refs 48 and 49), gravity force with buoyancy ($\vec{F}_g$), Brownian force ($\vec{F}_B$), and optical gradient force[40] ($\vec{F}_{opt}$) are as given in eqs 2–5. We assume no other forces are included here, such as the thermophoretic force.[50] Equations 2–5 are described further below.

$$m_p \frac{d^2\vec{r}}{dt^2} = m_p \frac{d\vec{v}}{dt} = \vec{F}_D + \vec{F}_g + \vec{F}_B + \vec{F}_{opt} \tag{1}$$

$$\vec{F}_D = \frac{m_p}{\tau_p}(\vec{u} - \vec{v}), \quad \tau_p = \frac{\rho_p d_p^2}{18\mu} \tag{2}$$

$$\vec{F}_g = m_p \vec{g} \frac{(\rho_p - \rho)}{\rho_p} \tag{3}$$

$$\vec{F}_B = \zeta \sqrt{\frac{12\pi k_B \mu T r_p}{\Delta t}} \tag{4}$$

$$\vec{F}_{opt} = \pi r_p^3 \varepsilon_0 n_f^2 \frac{n_p^2 - n_f^2}{n_p^2 + 2n_f^2} \nabla |\vec{E}(\vec{r})|^2 \tag{5}$$

The force $\vec{F}_D$ is known as Stokes drag, τ_p is the particle velocity response time, $\vec{v}$ is the particle velocity, $\vec{u}$ is the fluid velocity, μ is the fluid viscosity, ρ_p is the material density of the NP, and d_p is the particle diameter. We take the fluid velocity $\vec{u}$ to be zero, as it is predicted by the simulations of Figure 2 to have a very small value near DNH surface. The additional computational expense of including it in this simulation is therefore unjustified. We employ Stokes' drag in its basic form (eq 2) and do not modify it via Faxén's law[48,49] (see Supporting Information). The force $\vec{F}_g$ is gravity force with buoyancy, with ρ being the water density and $\vec{g}$ being the acceleration due to gravity. The force $\vec{F}_B$ is a stochastic Brownian force modeled as a Gaussian white noise process.[51,52] In this equation, Δt is the time step taken by the solver, r_p is the particle radius, T is the fluid temperature, k_B is the Boltzmann constant, and ζ is a normally distributed random number with a mean of zero and unit variance. Equation 5 provides the expression for the optical trapping force $\vec{F}_{opt}$. It can be seen that we employ the optical gradient force, with the NP approximated as an electric point dipole. This provides a considerable reduction in computational expense, in comparison to calculating the optical force rigorously using the Maxwell stress tensor (MST). One might expect the gradient force to be a reasonable approximation, given that the NP is small (20 nm diameter) and its refractive index is close to water (Δn = 0.27) in comparison to what

DOI: 10.1021/acsphotonics.8b00176
ACS Photonics 2018, 5, 2850–2859

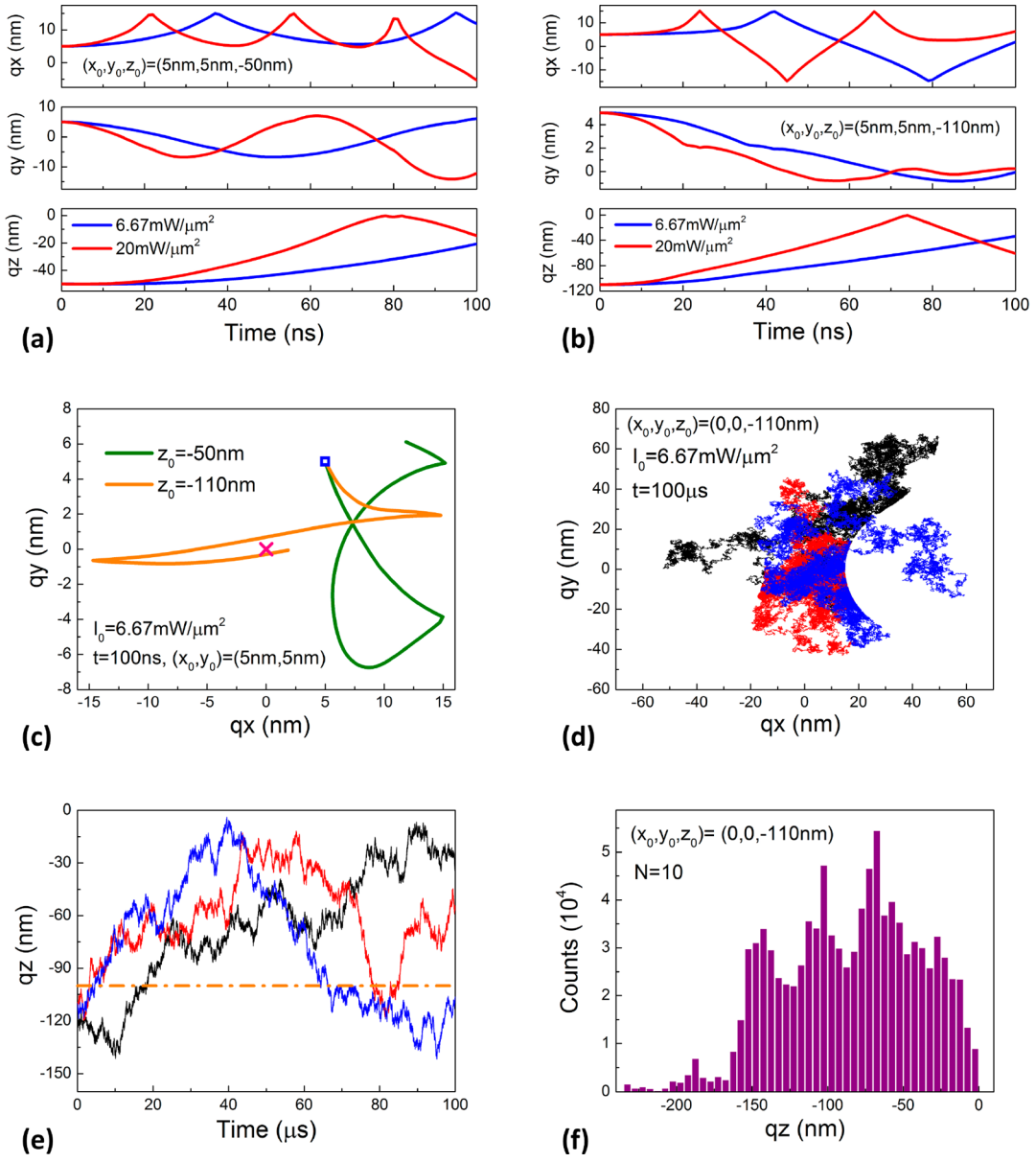

Figure 5. (a–c) Simulation of NP trajectories (20 nm diameter), with only optical force modeled. DNH is illuminated by *x*-polarized plane wave at a wavelength of 1064 nm. (a, b) Particle trajectories as a function of time. Initial release position (a) (x_0, y_0, z_0) = (5 nm, 5 nm, −50 nm); (b) (x_0, y_0, z_0) = (5 nm, 5 nm, −110 nm). (c) Plot of trajectories (each 100 ns duration) in *xy*-plane for the two different release positions, from data of (a) and (b) for I_0 = 6.67 mW/μm^2. Blue square indicates initial position and pink cross indicates DNH center. (d–f) Simulation of NP trajectories (20 nm diameter) influenced by all forces, for I_0 = 6.67 mW/μm^2. (d) Position (in *xy*-plane) vs time tracking of three NPs (20 nm diameter). (e) Vertical positions vs time for same trajectories as (d). DNH edge (gold film surface) is denoted by orange dashed-dotted line. (f) Histogram of vertical positions of trajectories of 10 NPs, for bin width of 5 nm. Each trajectory has a duration of 100 μs and time step 0.5 ns (2 × 10^5 time steps).

would occur for a metal (e.g., Au) or high index dielectric (e.g., Si) nanoparticle. We furthermore provide a comparison between the gradient force calculated in this way (dipole approximation) with that calculated rigorously by the MST in the Supporting Information. It can be seen that they are in reasonable agreement. The fact that they are in agreement also suggests that in our configuration, the perturbation to the DNH field distribution by the presence of the NP is not important for the trapping process. In other words, this effect (sometimes termed SIBA[10]) is not important in the trapping process in this tested geometry. In eq 5, ε_0 is the vacuum permittivity, n_f is the refractive index of water, and n_p is the refractive index of particle.

By solving eq 1 to eq 5 numerically with a given initial velocity ($\vec{v}_0$ = 0 at t = 0) and a given initial position (x_0, y_0, z_0), particle trajectories can be modeled. We begin, however, by performing modeling that includes only the optical forces. In other words, only $\vec{F}_{opt}$ is nonzero in eq 1. We assume that when the NP encounters the wall (gold or glass surface) it is reflected from it such that the particle momentum is conserved. In Figure 5a, we show the trajectories that result when the NP is released at (x_0, y_0, z_0) = (5 nm, 5 nm, −50 nm) for two different illumination intensities and with only optical forces included. In Figure 5b, this is repeated for a release position of (x_0, y_0, z_0) = (5 nm, 5 nm, −110 nm). In Figure 5c, we plot the corresponding trajectories in the *xy*-plane for the illumination intensity of I_0 = 6.67 mW/μm^2. The solver time step is set to be

DOI: 10.1021/acsphotonics.8b00176
ACS Photonics 2018, 5, 2850–2859

0.1 ns. It can be seen from Figure 5c that, after release, for both cases of starting position, the NP initially moves toward the right hotspot, reaching it at 20 or 40 ns. The NP is then reflected from the wall. Throughout the duration of the plotted trajectories (100 ns), the z-component of the optical force (F_z) remains positive, so the NP is continually pulled toward the bottom of the DNH, bouncing off the walls as it encounters them. We next perform modeling including all forces in eqs 1−5. As noted by Bui et al, the accurate simulation of optical and Brownian forces requires the time step Δt to be chosen carefully.[45] We set the solver time step to be $\Delta t = 0.5$ ns, which is small enough to ensure that over the distance the NP moves over one time step, the optical (and other) forces do not vary much. We simulate particle trajectories over durations of 100 μs, that is, 2×10^5 time steps. We show three trajectories in Figure 5d,e for all of which the initial release position is (x_0, y_0, z_0) = (0, 0, −110 nm). We plot the trajectories in the xy-plane in Figure 5d and the corresponding vertical (z) positions as a function of time in Figure 5e. It can be seen that the NP moves around DNH, strongly influenced by the Brownian force. We attribute the asymmetrical confinements in x- and y-axes that we observe experimentally to arise from both the optical forces and the morphology of the DNH. By the latter, we refer to the fact that the DNH morphology represents a constriction that limits particle movement along the x-axis, while it is far less constrained along the y-axis. From Figure 5e, it can be seen that the Brownian forces acting on the NP result in it jittering in and out of the DNH. In Figure 5f, the results of ten simulated NP trajectories (each with duration 100 μs) are shown as a histogram of vertical position. It can be seen that the NP largely remains within the region of high intensity, that is, within the DNH aperture or a small distance (∼50 nm) from it. In our experiments, our camera (EM-CCD) is operated at 30 frames per second, that is, 33 ms between frames, over tens of seconds. Furthermore, our imaging method is inherently two-dimensional, that is, we track particle positions in x- and y-, but not along the z-axis. Our theoretical modeling on the other hand, allows us to predict nanoparticle trajectories in three dimensions and with temporal resolution that is in principle arbitrarily high. Due to practical considerations, the duration of the modeled trajectory is limited, in our case, to 100 μs. This simulation takes 3 days to perform on a standard desktop computer at the time of writing. Nonetheless, the combination of theoretical modeling and particle tracking experiments elucidate the dynamics of nanoparticles trapped by the DNH nanoaperture on time scales ranging from nanoseconds to tens of seconds. In these simulations, we do not include forces such as adhesion and so on. Such forces can be challenging to accurately model.[45] Finally, we note that we do not rule out the possibility that other forces may contribute to the observed localization. These may be the topic of future investigations.

In conclusion, we employ fluorescence microscopy to directly observe the dynamics of a single nanosphere with a diameter of 20 nm optically trapped by a double nanohole in a gold film. We track its position and fluorescent emission as a function of time, demonstrating that the region visited by the trapped nanoparticle has an elliptical shape and that tighter spatial confinement occurs at the higher laser intensity. We perform numerical simulations to further elucidate the DNH trapping process, including predicting trajectories over time intervals too short for the experiments. Our simulations include electric field distribution, heat generation, fluid velocity, optical forces, potential energy, and the dynamics of the trapping process, that is, nanoparticle trajectories. The theoretical prediction and experimental demonstration in this work will be useful for the better understanding of the fundamental physics of light−nanostructure interactions and could open new avenues for the future optical trapping devices on the nanoscale.

■ ASSOCIATED CONTENT

Supporting Information

The Supporting Information is available free of charge on the ACS Publications website at DOI: 10.1021/acsphotonics.8b00176.

Detailed descriptions of the experimental methods, simulation methods, theoretical formula, and additional experimental and numerical figures (PDF).

Movie 1 illustrates the optical trapping and release of a single 20 nm polystyrene nanoparticle in real time (AVI).

Movie 2 demonstrates the optical tracking of a 20 nm nanoparticle trapped by a DNH (AVI).

■ AUTHOR INFORMATION

Corresponding Author

*E-mail: kcrozier@unimelb.edu.au.

ORCID

Kenneth B. Crozier: 0000-0003-0947-001X

Author Contributions

Z.X. and K.B.C. conceived and designed the research study. Z.X. performed experiments, simulation, and data analysis. All authors discussed the results. Z.X. and K.B.C. wrote the manuscript.

Notes

The authors declare no competing financial interest.

■ ACKNOWLEDGMENTS

This research was sponsored in part by the Australian Research Council (DP150103736 and FT140100577), by the Victorian Endowment for Science, Knowledge and Innovation (VESKI), and by the Laby Foundation. This work was performed in part at the Melbourne Centre for Nanofabrication (MCN) in the Victorian Node of the Australian National Fabrication Facility (ANFF).

■ REFERENCES

(1) Ashkin, A. Acceleration and trapping of particles by radiation pressure. *Phys. Rev. Lett.* **1970**, *24*, 156−159.

(2) Ashkin, A.; Dziedzic, J. M.; Bjorkholm, J.; Chu, S. Observation of a single-beam gradient force optical trap for dielectric particles. *Opt. Lett.* **1986**, *11*, 288−290.

(3) Ashkin, A.; Dziedzic, J. M.; Yamane, T. Optical trapping and manipulation of single cells using infrared laser beams. *Nature* **1987**, *330*, 769−771.

(4) Grier, D. G. A revolution in optical manipulation. *Nature* **2003**, *424*, 810−816.

(5) Neuman, K. C.; Block, S. M. Optical trapping. *Rev. Sci. Instrum.* **2004**, *75*, 2787−2809.

(6) Spesyvtseva, S. E. S.; Dholakia, K. Trapping in a material world. *ACS Photonics* **2016**, *3*, 719−736.

(7) Kwak, E. S.; Onuta, T. D.; Amarie, D.; Potyrailo, R.; Stein, B.; Jacobson, S. C.; Schaich, W.; Dragnea, B. Optical trapping with integrated near-field apertures. *J. Phys. Chem. B* **2004**, *108*, 13607−13612.

(8) Grigorenko, A.; Roberts, N.; Dickinson, M.; Zhang, Y. Nanometric optical tweezers based on nanostructured substrates. *Nat. Photonics* **2008**, *2*, 365−370.
(9) Righini, M.; Ghenuche, P.; Cherukulappurath, S.; Myroshnychenko, V.; García de Abajo, F.; Quidant, R. Nano-optical trapping of Rayleigh particles and Escherichia coli bacteria with resonant optical antennas. *Nano Lett.* **2009**, *9*, 3387−3391.
(10) Juan, M. L.; Gordon, R.; Pang, Y.; Eftekhari, F.; Quidant, R. Self-induced back-action optical trapping of dielectric nanoparticles. *Nat. Phys.* **2009**, *5*, 915−919.
(11) Zhang, W.; Huang, L.; Santschi, C.; Martin, O. J. Trapping and sensing 10 nm metal nanoparticles using plasmonic dipole antennas. *Nano Lett.* **2010**, *10*, 1006−1011.
(12) Juan, M. L.; Righini, M.; Quidant, R. Plasmon nano-optical tweezers. *Nat. Photonics* **2011**, *5*, 349−356.
(13) Tsai, W. Y.; Huang, J. S.; Huang, C. B. Selective trapping or rotation of isotropic dielectric microparticles by optical near field in a plasmonic archimedes spiral. *Nano Lett.* **2014**, *14*, 547−552.
(14) Pang, Y.; Gordon, R. Optical trapping of 12 nm dielectric spheres using double-nanoholes in a gold film. *Nano Lett.* **2011**, *11*, 3763−3767.
(15) Chen, C.; Juan, M. L.; Li, Y.; Maes, G.; Borghs, G.; Van Dorpe, P.; Quidant, R. Enhanced optical trapping and arrangement of nano-objects in a plasmonic nanocavity. *Nano Lett.* **2012**, *12*, 125−132.
(16) Berthelot, J.; Aćimović, S.; Juan, M.; Kreuzer, M.; Renger, J.; Quidant, R. Three-dimensional manipulation with scanning near-field optical nanotweezers. *Nat. Nanotechnol.* **2014**, *9*, 295−299.
(17) Al Balushi, A. A.; Kotnala, A.; Wheaton, S.; Gelfand, R. M.; Rajashekara, Y.; Gordon, R. Label-free free-solution nanoaperture optical tweezers for single molecule protein studies. *Analyst* **2015**, *140*, 4760−4778.
(18) Mestres, P.; Berthelot, J.; Aćimović, S. S.; Quidant, R. Unraveling the optomechanical nature of plasmonic trapping. *Light: Sci. Appl.* **2016**, *5*, 1−14.
(19) Wang, K.; Schonbrun, E.; Steinvurzel, P.; Crozier, K. B. Trapping and rotating nanoparticles using a plasmonic nano-tweezer with an integrated heat sink. *Nat. Commun.* **2011**, *2*, 469.
(20) Wang, K.; Crozier, K. B. Plasmonic trapping with a gold nanopillar. *ChemPhysChem* **2012**, *13*, 2639−2648.
(21) Yang, A. H.; Moore, S. D.; Schmidt, B. S.; Klug, M.; Lipson, M.; Erickson, D. Optical manipulation of nanoparticles and biomolecules in sub-wavelength slot waveguides. *Nature* **2009**, *457*, 71−75.
(22) Lin, S.; Crozier, K. B. An integrated microparticle sorting system based on near-field optical forces and a structural perturbation. *Opt. Express* **2012**, *20*, 3367−3374.
(23) Lin, S.; Schonbrun, E.; Crozier, K. B. Optical manipulation with planar silicon microring resonators. *Nano Lett.* **2010**, *10*, 2408−2411.
(24) Lin, S.; Crozier, K. B. Planar silicon microrings as wavelength-multiplexed optical traps for storing and sensing particles. *Lab Chip* **2011**, *11*, 4047−4051.
(25) Mandal, S.; Serey, X.; Erickson, D. Nanomanipulation using silicon photonic crystal resonators. *Nano Lett.* **2010**, *10*, 99−104.
(26) Chen, Y. F.; Serey, X.; Sarkar, R.; Chen, P.; Erickson, D. Controlled photonic manipulation of proteins and other nanomaterials. *Nano Lett.* **2012**, *12*, 1633−1637.
(27) Baffou, G.; Quidant, R. Thermo-plasmonics: using metallic nanostructures as nano-sources of heat. *Laser Photonics Rev.* **2013**, *7*, 171−187.
(28) Johnson, P. B.; Christy, R. W. Optical constants of the noble metals. *Phys. Rev. B* **1972**, *6*, 4370−4379.
(29) Baffou, G.; Quidant, R.; García de Abajo, F. J. Nanoscale control of optical heating in complex plasmonic systems. *ACS Nano* **2010**, *4*, 709−716.
(30) Baffou, G.; Berto, P.; Bermúdez Ureña, E.; Quidant, R.; Monneret, S.; Polleux, J.; Rigneault, H. Photoinduced heating of nanoparticle arrays. *ACS Nano* **2013**, *7*, 6478−6488.
(31) Garcés-Chávez, V.; Quidant, R.; Reece, P.; Badenes, G.; Torner, L.; Dholakia, K. Extended organization of colloidal microparticles by surface plasmon polariton excitation. *Phys. Rev. B: Condens. Matter Mater. Phys.* **2006**, *73*, 085417.
(32) Landau, L. D.; Lifshitz, E. M. *Fluid Mechanics*; Elsevier Science, 2013.
(33) Donner, J. S.; Baffou, G.; McCloskey, D.; Quidant, R. Plasmon-assisted optofluidics. *ACS Nano* **2011**, *5*, 5457−5462.
(34) Haynes, W. M. *CRC Handbook of Chemistry and Physics*; CRC Press, 2014.
(35) Roxworthy, B. J.; Bhuiya, A. M.; Vanka, S. P.; Toussaint, K. C., Jr. Understanding and controlling plasmon-induced convection. *Nat. Commun.* **2014**, *5*, 3173.
(36) Ndukaife, J. C.; Mishra, A.; Guler, U.; Nnanna, A. G. A.; Wereley, S. T.; Boltasseva, A. Photothermal heating enabled by plasmonic nanostructures for electrokinetic manipulation and sorting of particles. *ACS Nano* **2014**, *8*, 9035−9043.
(37) Ndukaife, J. C.; Kildishev, A. V.; Nnanna, A. G.; Shalaev, V. M.; Wereley, S. T.; Boltasseva, A. Long-range and rapid transport of individual nano-objects by a hybrid electrothermoplasmonic nanotweezer. *Nat. Nanotechnol.* **2015**, *11*, 53−60.
(38) Wang, X.; Wang, X. B.; Gascoyne, P. R. General expressions for dielectrophoretic force and electrorotational torque derived using the Maxwell stress tensor method. *J. Electrost.* **1997**, *39*, 277−295.
(39) Jackson, J. D. *Classical Electrodynamics*; John Wiley & Sons, 2007.
(40) Novotny, L.; Hecht, B. *Principles of Nano-Optics*; Cambridge University Press, 2012.
(41) Ploschner, M.; Mazilu, M.; Krauss, T. F.; Dholakia, K. Optical forces near a nanoantenna. *J. Nanophotonics* **2010**, *4*, 041570.
(42) Lehmuskero, A.; Johansson, P.; Rubinsztein-Dunlop, H.; Tong, L.; Kall, M. Laser trapping of colloidal metal nanoparticles. *ACS Nano* **2015**, *9*, 3453−3469.
(43) Parthasarathy, R. Rapid, accurate particle tracking by calculation of radial symmetry centers. *Nat. Methods* **2012**, *9*, 724−726.
(44) Wong, W. P.; Halvorsen, K. The effect of integration time on fluctuation measurements: calibrating an optical trap in the presence of motion blur. *Opt. Express* **2006**, *14*, 12517−12531.
(45) Bui, A. A.; Stilgoe, A. B.; Lenton, I. C.; Gibson, L. J.; Kashchuk, A. V.; Zhang, S.; Rubinsztein-Dunlop, H.; Nieminen, T. A. Theory and practice of simulation of optical tweezers. *J. Quant. Spectrosc. Radiat. Transfer* **2017**, *195*, 66−75.
(46) Righini, M.; Zelenina, A. S.; Girard, C.; Quidant, R. Parallel and selective trapping in a patterned plasmonic landscape. *Nat. Phys.* **2007**, *3*, 477−480.
(47) Volpe, G.; Volpe, G. Simulation of a Brownian particle in an optical trap. *Am. J. Phys.* **2013**, *81*, 224−230.
(48) Durlofsky, L.; Brady, J. F.; Bossis, G. Dynamic simulation of hydrodynamically interacting particles. *J. Fluid Mech.* **1987**, *180*, 21−49.
(49) Svoboda, K.; Block, S. M. Biological applications of optical forces. *Annu. Rev. Biophys. Biomol. Struct.* **1994**, *23*, 247−285.
(50) Duhr, S.; Braun, D. Why molecules move along a temperature gradient. *Proc. Natl. Acad. Sci. U. S. A.* **2006**, *103*, 19678−19682.
(51) Kim, M.-m.; Zydney, A. L. Effect of electrostatic, hydrodynamic, and Brownian forces on particle trajectories and sieving in normal flow filtration. *J. Colloid Interface Sci.* **2004**, *269*, 425−431.
(52) Heiniger, A. T.; Miller, B. L.; Fauchet, P. M. Numerical study of sensitivity enhancement in a photonic crystal microcavity biosensor due to optical forces. *Opt. Express* **2015**, *23*, 25072−25083.

DOI: 10.1021/acsphotonics.8b00176
ACS Photonics 2018, 5, 2850−2859

Supporting Information

Direct particle tracking observation and Brownian dynamics simulations of a single nanoparticle optically trapped by a plasmonic nanoaperture

Zhe Xu,[†] *Wuzhou Song,*[†,‡] *and Kenneth B. Crozier**[*,†,§]

[†]School of Physics, University of Melbourne, Victoria 3010, Australia

[‡]School of Materials Science and Engineering, Huazhong University of Science and Technology, Wuhan 430074, P. R. China

[§]Department of Electrical and Electronic Engineering, University of Melbourne, Victoria 3010, Australia

Corresponding Author

* E-mail: kcrozier@unimelb.edu.au.

S1 Experimental setup

The experimental set-up is schematically illustrated as Fig. S1a. Trapping is monitored by observing the nanoparticle (NP) fluorescence using an electron multiplying camera (EM-CCD). An optical beam shutter is used to switch on and off the trapping laser. A 1064 nm half-wave plate is used to rotate the polarization of the laser beam (*x*-polarized). The polystyrene nanoparticles (FluoSpheres, 20 nm diameter, carboxylate-modified, Nile Red, Life Technologies) are suspended in Ultra-Pure distilled water with a trace amount of Tween 20 surfactant (0.05% v/v) and the solution is passed through a filter to remove aggregates, etc. The nanoparticles have a coefficient of variation of about 20%, according to the manufacturer (Life Technologies). The transmission of oil objective to the focal plane at 1064 nm is ~50%. Fig. S1b details the cross section of closed perfusion chamber, sealed with UV-cured optical adhesives. The chamber is fabricated on a glass slide using standard photolithography methods. The photoresist (AZ9260) thickness is determined by the rotation speed of spin-coater and measured with an optical profilometer. A thickness of ~20 μm is chosen in order to make the chamber relatively shallow, which facilitates observation of the trapping process. The sample package is mounted upside-down. Polyethylene tubing is used to deliver fluid into the channel. Prior to chamber fabrication, the glass coverslip is sonicated in water and cleaned with a plasma cleaner to remove particles etc. from the surface. The gold film (containing the DNH) is washed with acetone and rinsed with isopropanol and distilled water. Fig. S1c shows the SEM (left) and microscope (right) images of double nanohole (DNH) aperture fabricated in the gold film.

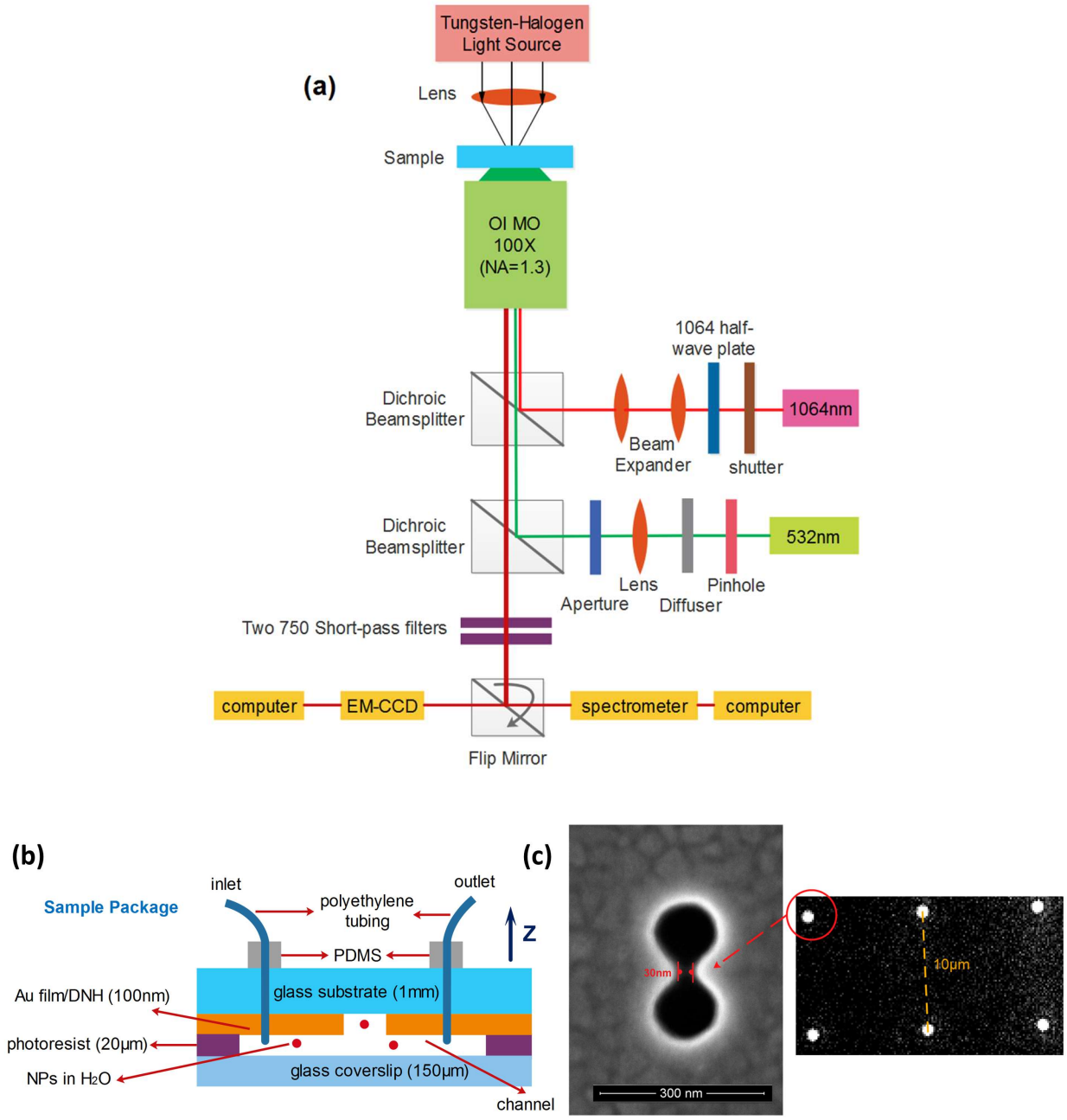

Figure S1. (a) Schematic diagram of experimental set-up. Trapping laser: Laser Quantum Ventus 1064; Oil immersion objective: Nikon Plan Fluorite Oil Immersion Objective, 100×, NA=1.3; Electron multiplying camera: EM-CCD, ProEM-HS: 512×512. (b) Cross section of closed perfusion chamber, sealed with UV-cured optical adhesives. (c) SEM (left) and optical microscope (right) images of DNH fabricated in the gold film.

S2 Optical forces in confined fields

Forces in the dipole approximation: Conventional optical tweezers can be well described by the dipole approximation[1-5], where the particle dimension is much smaller than the illumination wavelength ($r_p << \lambda$). In this case, the particle is approximated by an electric dipole and two types of *time-averaged* optical forces can be considered[2, 4].

The first type of force, the *gradient force* due to dielectrophoresis, is proportional to the gradient of the square of the electric field, which pulls the particle towards the region of maximum light intensity. This term is called the optical trapping force and is a conservative force.

$$\left\langle \vec{F}_{grad} \right\rangle = \pi {r_p}^3 \varepsilon_0 n_f^2 \frac{n_p^2 - n_f^2}{n_p^2 + 2n_f^2} \nabla \left| \vec{E} \right|^2 \tag{1}$$

where r_p is the particle radius, ε_0 is the vacuum permittivity, n_f is the refractive index of the surrounding medium and n_p is the refractive index of the particle.

The second type of force, the non-conservative *scattering force*, proportional to the total cross-section of the particle, can be written as the sum of two contributions: a *radiation pressure force* that acts to push the particle in the direction of the Poynting vector, and a *spin curl force* associated with a non-uniform distribution of the spin density of the light field.

$$\left\langle \vec{F}_{scat} \right\rangle = \frac{\sigma}{2c} \mathrm{Re}(\vec{E} \times \vec{H}^*) + \sigma c \nabla \times (\frac{\varepsilon_0}{4\omega i} \vec{E} \times \vec{E}^*) \tag{2}$$

For a plane wave of intensity I_0 propagating in direction of $\vec{s}$, the spin curl force is zero and the scattering force on a *dielectric* particle is:

$$\left\langle \vec{F}_{scat} \right\rangle = \frac{128\pi^5 r_p^6}{3\lambda^4 c} (\frac{n_p^2 - n_f^2}{n_p^2 + 2n_f^2})^2 I_0 \vec{s} \tag{3}$$

where σ is the total cross-section of the particle, c is the light speed in vacuum, λ is the trapping laser wavelength and $\vec{s}$ is the unit propagation vector.

Forces beyond the dipole approximation: When a particle cannot be approximated as a dipole, the net force exerted on it can be determined by the Maxwell's stress tensor (MST).[3, 6, 7] MST analysis is a rigorous way of computing the optical force acting on an object. The total *time-averaged* electromagnetic force exerted on a particle interacting with an optical field is given by:

$$\left\langle \vec{F} \right\rangle = \int_{\partial V} \left\langle \vec{\vec{T}}(\vec{r},t) \right\rangle \bullet \vec{n}(\vec{r}) da \tag{4}$$

where $\vec{\vec{T}}(\vec{r},t)$ is called Maxwell's stress tensor (MST), $\vec{n}(\vec{r})$ is the unit vector perpendicular to the object surface ∂V, and da is an infinitesimal surface element. In Cartesian components, the MST reads as:

$$\vec{\vec{T}} = [\varepsilon_e \vec{E}\vec{E} + \mu_e \vec{H}\vec{H} - \frac{1}{2}(\varepsilon_e E^2 + \mu_e H^2)\vec{\vec{I}}] \tag{5}$$

where $\varepsilon_e = \varepsilon_0 \varepsilon_r$, $\mu_e = \mu_0 \mu_r$ are the permittivity and permeability of the surrounding medium respectively, ε_0 is the vacuum permittivity, μ_0 is the vacuum permeability, ε_r is the relative permittivity and μ_r is the relative permeability. The fields used to calculate the force are the self-consistent fields, which means that they are a superposition of the incident and the scattered fields. The trapping potential energy of the particle in the force fields can be directly defined as[3]:

$$U(\vec{r}_0) = -\int_{\infty}^{\vec{r}_0} \left\langle \vec{F}(\vec{r}) \right\rangle \bullet d\vec{r} \tag{6}$$

For comparison, we calculate the force on a NP (20 nm diameter) in the vicinity of the DNH structure using both the gradient force (dipole approximation) and the MST method (i.e. the rigorous approach). The configuration is schematically illustrated as Fig. S2a. The results are shown as Fig. S2b. It can be seen that the methods yield results that are in general agreement. This is reasonable because the NP is small (20 nm diameter) and has a refractive index that is close to that of the water. Accordingly, we employ the optical gradient force in the Langevin equation for the trajectory simulations.

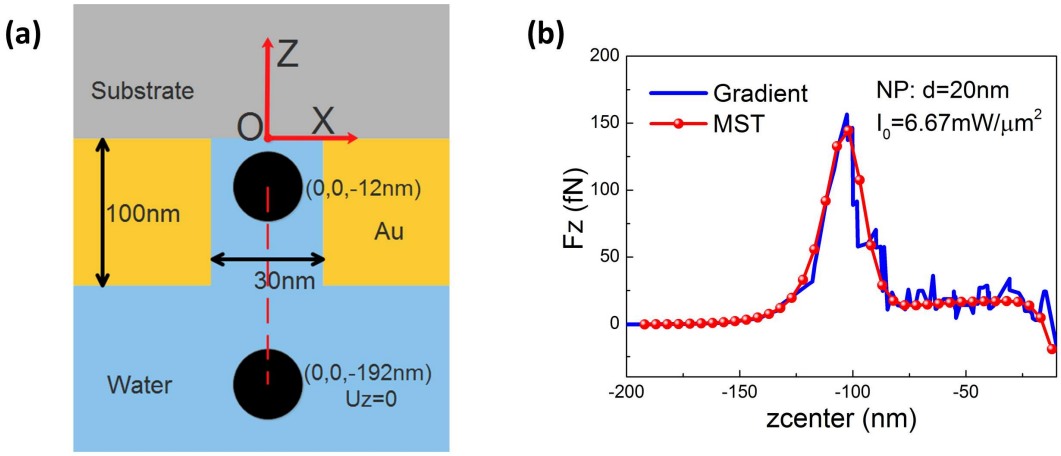

Figure S2. (a) Schematic diagram for MST force calculation. (b) Comparison of vertical force F_z along z direction exerted on a 20 nm polystyrene NP trapped by a DNH, calculated by the dipole approximation (Eq. 1) and the MST (Eq. 4) for I_0=6.67 mW/μm^2. (x_{center}=y_{center}=0)

S3 COMSOL simulation method

We use COMSOL Multiphysics to simulate our DNH with three-dimensional geometry.

S3.1 Numerical simulation of electromagnetic scattering, force and potential;

We use the "Wave Optics Module" of COMSOL Multiphysics. The DNH is formed in a 100 nm thick gold film on a glass substrate. The simulations are performed as follows. We begin by finding the background field ($|E_0|$) via a full-field simulation in which light is incident on the glass substrate from the water, i.e. the gold film and DNH are not included. We then perform a scattered-field simulation that includes the gold film and DNH. The first simulation is set up with two port conditions. One defines the incident plane wave and allows for reflection, while the other absorbs the transmitted plane wave. The side boundaries have Floquet periodicity conditions. The second simulation introduces DNH as the scatterer and surrounds the geometry with PMLs (perfectly matched layers).

To calculate the optical forces with the MST, as explained in Ref [8], the problem reduces to solving the electromagnetic scattering problem. In the scattered-field simulation, the DNH and a single NP are introduced as two scatterers. The results are shown as Fig. S3. Once the fields are found, the force acting on the NP surface is determined by the MST. To find the force maps, this process is repeated for different choices of the NP position (x, y, z). The trapping potential is

found from the force map using the COMSOL "PDE Module" (partial differential equations). The refractive indices of water, glass and polystyrene are taken as 1.33, 1.45 and 1.6 respectively. The optical constant of gold is taken from the data of Johnson and Christy [9] (i.e. relative permittivity at 1064 nm is ε_r=-48.45-*i*3.6).

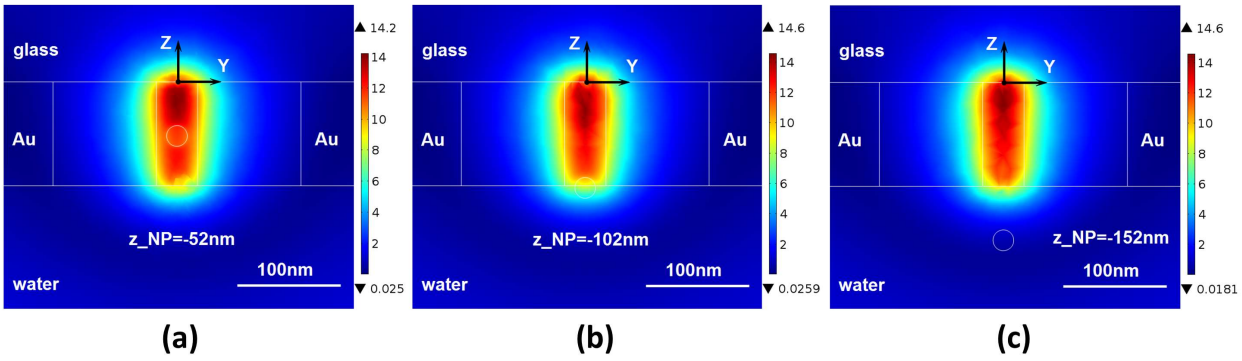

Figure S3. Electric field enhancement ($|E|/|E_0|$) distribution (x=0 cross section) in DNH, with a single NP (20 nm diameter) included in simulation. Plane wave illumination from water side is employed (x-polarized, λ=1064 nm). Black dot indicates coordinate system origin. Center z-coordinates of NP are as follows (with (x_{center}, y_{center})=(0 nm, 0 nm)). (a) z_{center}=-52 nm; (b) z_{center}=-102 nm; (c) z_{center}=-152 nm.

S3.2 Numerical simulation of thermal effects;

We use the heat transfer module ("Conjugate Heat Transfer-Laminar Flow") to solve the heat transfer and Navier-Stokes equations (here for steady state). The geometric configuration is shown in Fig. S4 (plot in y=0 and z=-50 nm cross section). The equations used in the modeling are as detailed in Ref [10-12], and include determination of the heat source, heat transfer in the solid and fluid regions, and non-isothermal flow in the water with volume force due to buoyancy. From the scattering simulation (Section S3.1), we can determine the absorbed total power from volume integration of power dissipation density. The spot size of the laser that is used in the experiments to illuminate the DNH is ~ μm-scale. We thus assume that the only source of heat in the system is the gold region with extent 1 μm×1 μm×100 nm that is centered over the DNH. We furthermore assume that the heating power is uniformly distributed throughout this region, which is reasonable because of the high thermal conductivity of gold. In the simulation, the outer glass boundaries are set to be 293.15 K. The initial temperature is also set to be 293.15 K. No-slip boundary conditions are employed at the boundaries between water and gold/glass. The

temperature-dependent thermal parameters of gold, glass and water are taken from COMSOL material library. The chamber height is taken to be 20 µm. As noted previously[10], the chamber height has an important influence on the magnitude of the water convection.

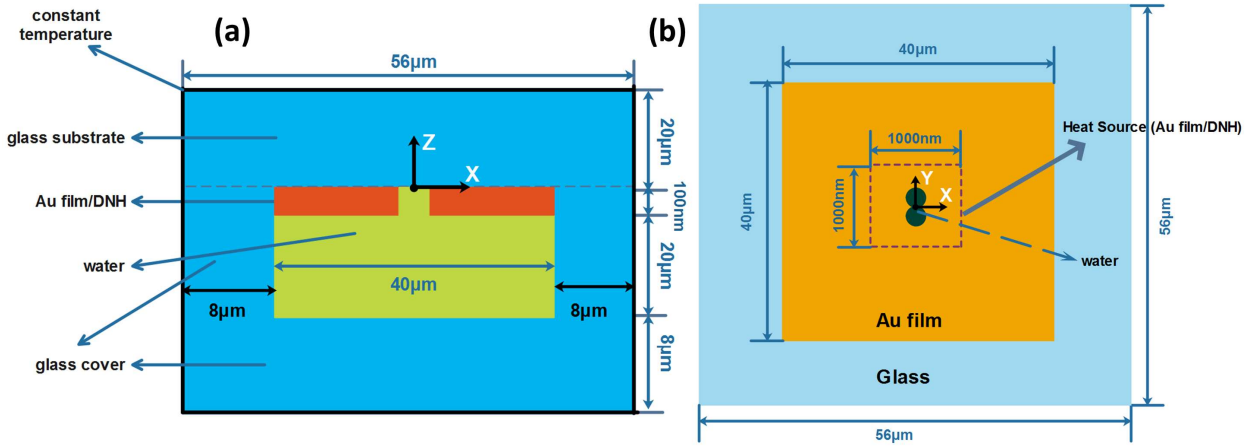

Figure S4. Geometric configuration used for the heating calculation. Sketch is not to scale. (a) y=0 cross section. Black line indicates chamber glass boundaries at which T_0=293.15 K. (b) z=-50 nm cross section. Purple dashed line indicates region that is assumed to act as the heat source.

The results of our heating calculations are shown as Fig. S5. These show the heat source power as a function of illumination intensity (Fig. S5a), the steady state temperature rise distribution (Fig. S5b) and the water convection velocity distribution in close proximity (200 nm, Fig. S5c) and further away (10 µm, Fig. S5d) from the gold film.

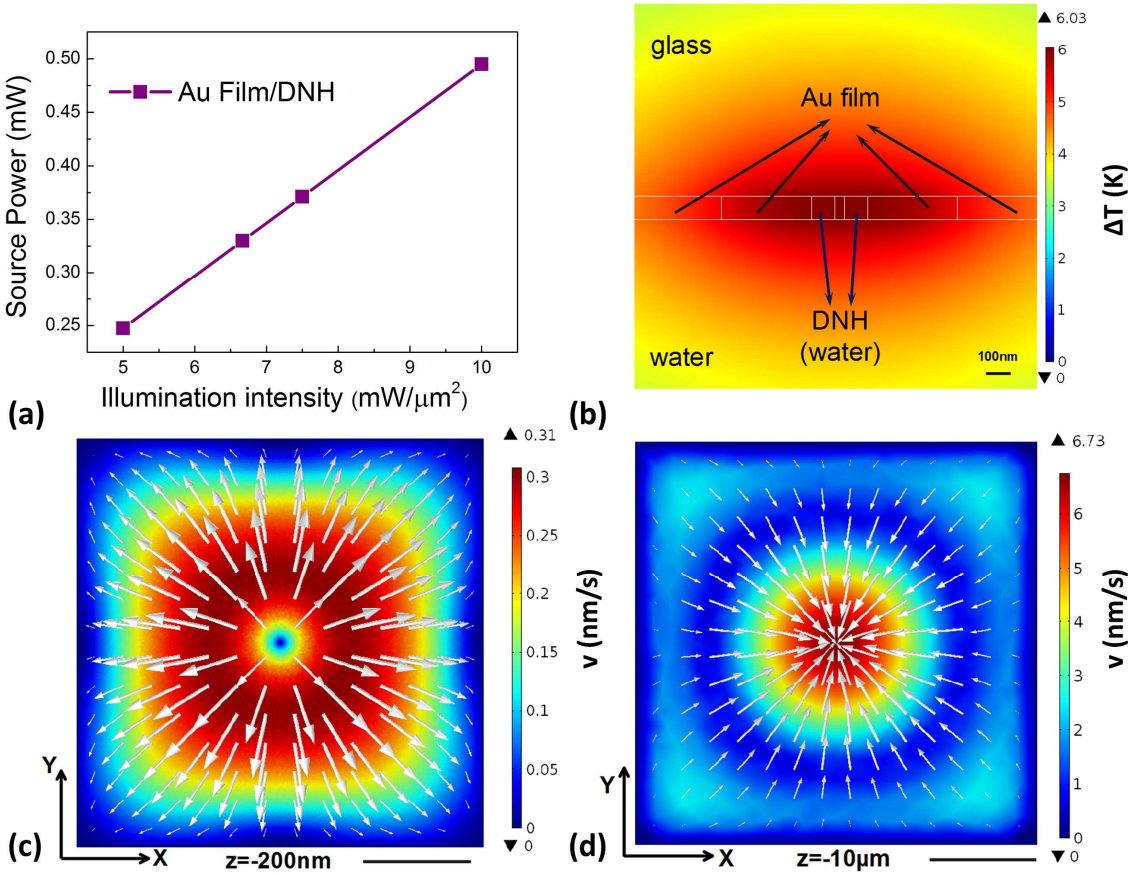

Figure S5. (a) Heat source power as a function of trapping laser intensity. (b) Steady-state temperature increase (ΔT: K) profile around DNH (x=0 cross section). (c)(d) FEM simulations of water convection velocity plotted in both magnitude (color map: nm/s) and direction (white arrows, magnitude proportionally-scaled). Scale bar: 10 μm. (c) z=-200 nm cross section; (d) z=-10 μm cross section. For panels b-d, I_0=6.67 mW/μm^2.

S3.3 Numerical simulation of particle trajectories;

We use the "Particle Tracing" option of the "Fluid Flow Module" of COMSOL Multiphysics to simulate particle trajectories. Initially (i.e. t=0), polystyrene nanospheres (20 nm diameter, n_{NP}=1.6) are released at different positions. For all of these, the initial velocities are zero. Forces on the particle include Stokes drag, gravity with buoyancy, Brownian and dielectrophoretic (i.e. optical gradient force) forces. We use the "Bounce" option of the module to model the interaction of the particle with the wall, i.e. the particles are taken as bouncing off the walls in a way that conserves particle momentum. This simplifying approach is often used when tracking particles in a fluid, but it may be interesting in the future to develop a more complex approach.

Stokes drag is used, with the background fluid velocity set to be zero. We make this assumption due to the fact that the modeling (e.g. Fig. S5c and d) reveals that it is very small. The basic form of Stokes drag (Eq. 2 of main text) is for the case of a sphere with a very small Reynolds number in an unbounded viscous fluid. If rather than being in an unbounded fluid, the sphere is close to a wall, then the Stokes drag is modified, as given by Faxén's law. We note however that the basic form of Faxén's law is only rigorously applicable to a much simpler geometry (sphere near flat wall) than our case (sphere inside or near DNH). We therefore employ Stokes drag in its basic form, and do not modify it via Faxén's law. For the dielectrophoretic force (optical gradient force) we use the electric field distribution found using the "Wave Optics Module", using piecewise polynomial recovery smoothing it to make results more accurate. The particle and water densities are 1.04 g/cm^3 and 1 g/cm^3 respectively. The temperature is set to be 300 K, which is roughly the sum of initial value 293.15 K and temperature increase ΔT at I_0=6.67 mW/μm^2. The water viscosity is 0.859 mPa·s. The time stepping method is the generalized-alpha method. The steps taken by solver are manually set to be 0.1 ns (*optical gradient force* only) and 0.5 ns (*all forces*). Data is extracted from the solver every 1 ns. In the simulation, a forward Euler step is used to compute the motion both before and after the wall collision when a particle-wall interaction happens.

S4 Optical force calculation using Maxwell stress tensor method

Calculations made using the Maxwell's stress tensor (MST) method of the force (F_z, i.e. vertical component) on the nanoparticle (NP) and the trapping potential energy U_z are shown as Fig. S6. It can be seen from Fig. S6a that F_z increases with the NP diameter, which is also expected from the dipole approximation. From Fig. S6b and c, it can be seen that F_z decreases with distance from the gold film surface and DNH, which is to be expected due to the evanescent nature of the fields. It can be seen from Fig. S6d that F_z is largest when the NP is close to the entry to the DNH. Calculations of trapping potential energy U_z and F_z are presented as Fig. S6e and f.

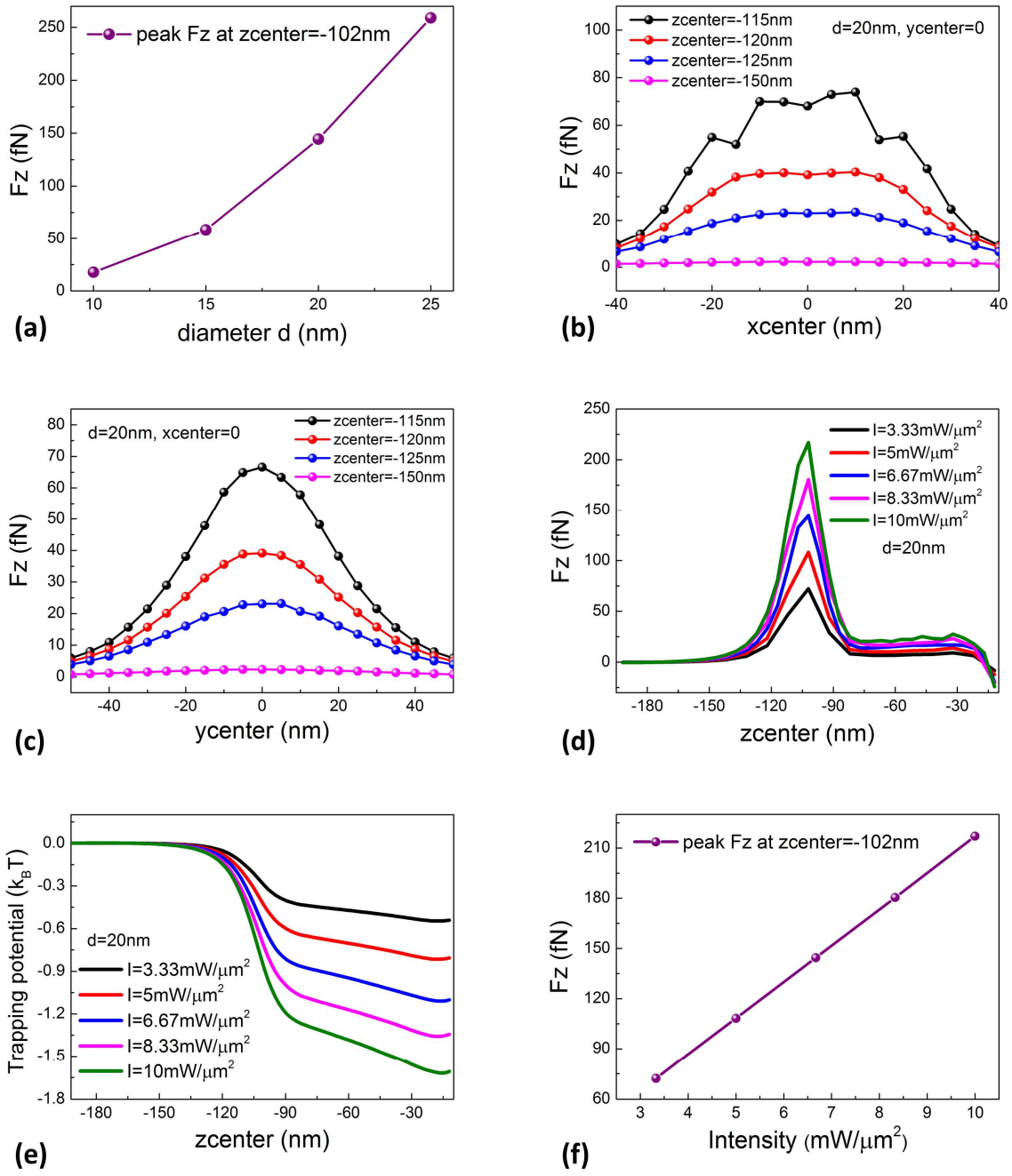

Figure S6. Optical forces of DNH exerted on a polystyrene nanoparticle (n_{NP}=1.6). (a) Peak F_z vs NP diameter d (extracted from data of Figure 3a). (b)(c) Vertical force F_z exerted on d=20 nm NP vs position. (b) y_{center}=0; (c) x_{center}=0. For panels a-c, I_0=6.67 mW/μm^2. (d) Vertical force F_z and (e) trapping potential energy U_z along z direction exerted on a 20 nm NP, as functions of

trapping laser intensity and position. (x_{center}=y_{center}=0) (f) Peak F_z vs trapping laser intensity (extracted from data of Figure S6d).

S5 EM-CCD fluorescence image of nanoparticles

As an additional check of the imaging capabilities of our system, we place a drop containing NPs at high concentration between two glass coverslips. This is then mounted in our optical microscope, and illuminated by our green laser. The image obtained with the EM-CCD camera is shown as Fig. S7a, with a red circle indicating an example of a single NP. We also use the system to obtain the fluorescence spectrum (Fig. S7b).

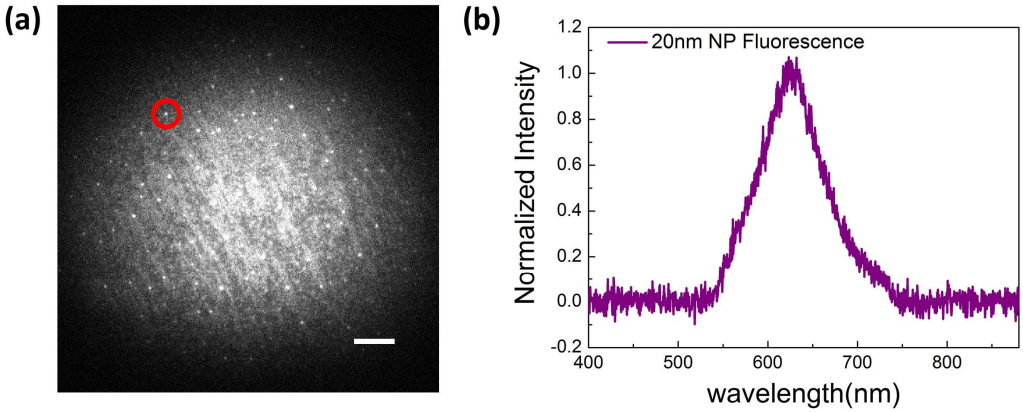

Figure S7. (a) EM-CCD image and (b) spectrum of high concentration NP solution drops between two coverslips, illuminated by a green laser. A single NP is indicated by a red circle. Scale bar: 8 μm.

S6 Results of numerical simulations of particle trajectories in DNH trapping

Selected results of the numerical simulations of the NP trajectory carried out using the method described in Section S3.3 are shown as Fig. S8. In Fig. S8a, simulated trajectories are presented in which the forces acting on the NP are due to the optical gradient force, gravity with buoyancy and Stokes drag (i.e. no Brownian force). In Fig. S8b, three particle trajectories are calculated with all forces in the *xz*-plane. In Fig. S8c and d, the results of ten simulated NPs trajectories (each with duration 100 μs) with all forces are shown as histograms in *x*- and *y*-axes. For panels a-d, I_0=6.67 mW/μm^2. In Fig. S8e, particle trajectories are plotted with all forces in the *xy*-plane. In Fig. S8f, a histogram of vertical NP positions with all forces is presented. For panels e and f, I_0=20 mW/μm^2.

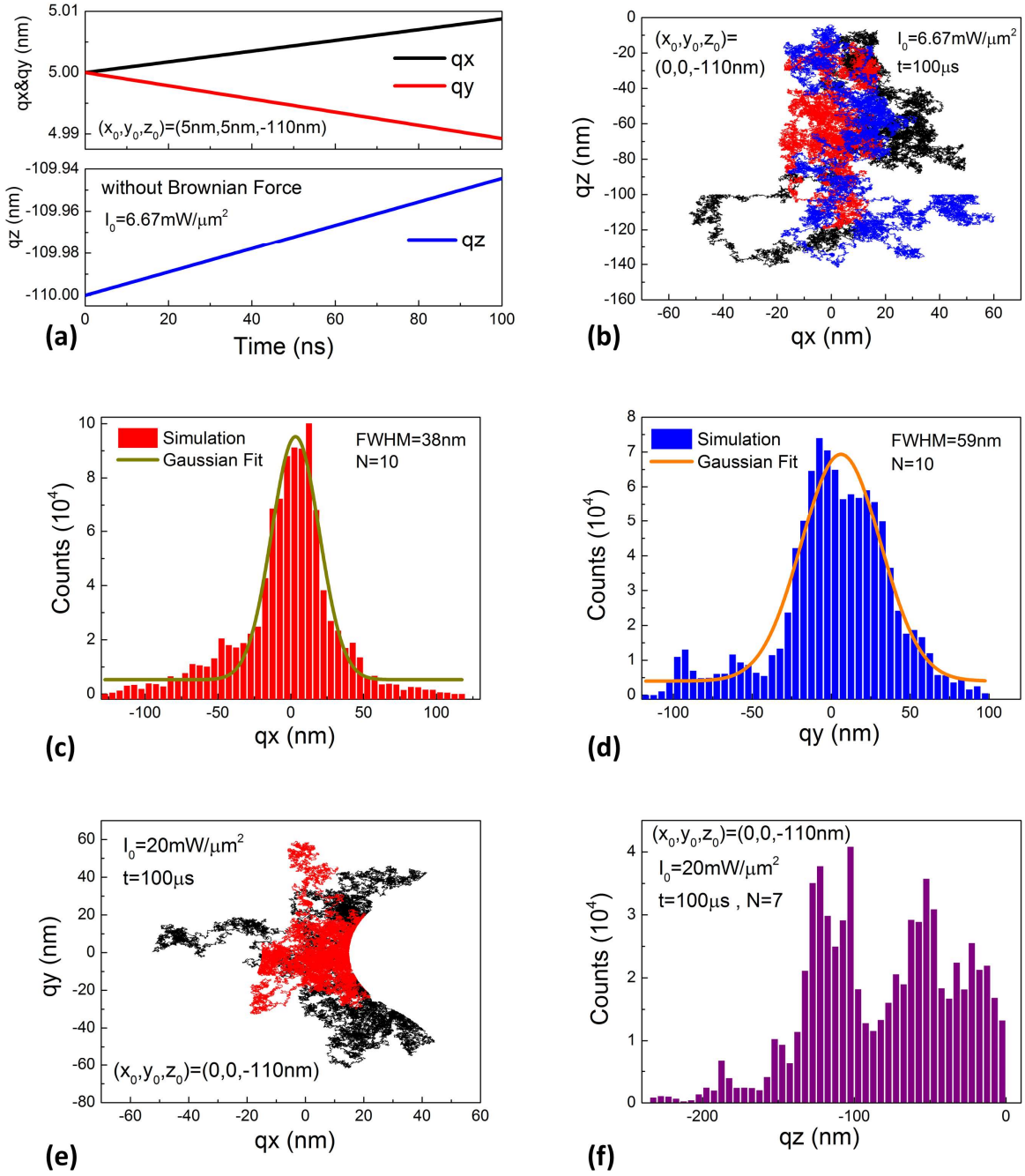

Figure S8. (a) Simulation of NP (20 nm diameter) trajectories influenced by drag force, gravity with buoyancy and optical force. (x_0,y_0,z_0)=(5 nm,5 nm,-110 nm). Trapping laser intensity I_0=6.67 mW/μm^2. Time step: 0.1 ns. (b)-(f) Simulation of particle trajectories (20 nm diameter) over 100 μs influenced by all forces. (x_0,y_0,z_0)=(0,0,-110 nm). Time step: 0.5 ns. (b) Position tracking in *xz*-plane for three NPs (same color particles as Figure 5d&e). Histograms of (c) *x*-

positions and (d) *y*-positions of ten NPs trajectories, for bin width of 5 nm (same ten NPs as Figure 5f). (e) Position tracking in *xy*-plane for two NPs. (f) Histogram of vertical positions of trajectories of seven modeled particles during 100 μs, for bin width of 5 nm. For panels b-d, I_0=6.67 mW/μm^2. For panels e&f, I_0=20 mW/μm^2.

Captions for Supporting Movies

Supporting Movie 1. DNH trapping and release of a single 20 nm polystyrene nanosphere. The movie is recorded at 30 fps. Trapping laser power P=38 mW (before objective) (i.e. I_0=16 mW/μm^2).

Supporting Movie 2. Optical tracking of a 20 nm nanoparticle trapped by a DNH. The movie is recorded at 30 fps. Trapping laser power P=15 mW (before objective) (i.e. I_0=6.6 mW/μm^2).

SUPPORTING INFORMATION REFERENCES

(1) Neuman, K. C.; Block, S. M. Optical trapping. *Rev. Sci. Instrum.* **2004**, 75, 2787-2809.
(2) Albaladejo, S.; Marqués, M. I.; Laroche, M.; Sáenz, J. J. Scattering forces from the curl of the spin angular momentum of a light field. *Phys. Rev. Lett.* **2009**, 102, 113602.
(3) Novotny, L.; Hecht, B. *Principles of Nano-Optics*. Cambridge University Press: **2012**.
(4) Spesyvtseva, S. E. S.; Dholakia, K. Trapping in a material world. *ACS Photonics* **2016**, 3, 719-736.
(5) Wang, K.; Crozier, K. B. Plasmonic trapping with a gold nanopillar. *ChemPhysChem* **2012**, 13, 2639-2648.
(6) Wang, X.; Wang, X. B.; Gascoyne, P. R. General expressions for dielectrophoretic force and electrorotational torque derived using the Maxwell stress tensor method. *J. Electrostatics* **1997**, 39, 277-295.
(7) Jackson, J. D. *Classical Electrodynamics*. John Wiley & Sons: **2007**.
(8) Ploschner, M.; Mazilu, M.; Krauss, T. F.; Dholakia, K. Optical forces near a nanoantenna. *J. Nanophotonics* **2010**, 4, 041570.
(9) Johnson, P. B.; Christy, R. W. Optical constants of the noble metals. *Phys. Rev. B* **1972**, 6, 4370-4379.
(10) Donner, J. S.; Baffou, G.; McCloskey, D.; Quidant, R. Plasmon-assisted optofluidics. *ACS Nano* **2011**, 5, 5457-5462.
(11) Roxworthy, B. J.; Bhuiya, A. M.; Vanka, S. P.; Toussaint, K. C., Jr. Understanding and controlling plasmon-induced convection. *Nat. Commun.* **2014**, 5, 3173.
(12) Ndukaife, J. C.; Kildishev, A. V.; Nnanna, A. G.; Shalaev, V. M.; Wereley, S. T.; Boltasseva, A. Long-range and rapid transport of individual nano-objects by a hybrid electrothermoplasmonic nanotweezer. *Nat. Nanotechnol.* **2016**, 11, 53-60.

CHAPTER 4

Optical trapping of nanoparticles using all-silicon nanoantennas

This chapter is originally published in ACS Photonics:

Zhe Xu, Wuzhou Song, and Kenneth B. Crozier. Optical Trapping of Nanoparticles Using All-Silicon Nanoantennas. ***ACS Photonics*** **2018**, 5, 4993–5001.

ACS Photonics

Article

Cite This: ACS Photonics 2018, 5, 4993−5001

pubs.acs.org/journal/apchd5

Optical Trapping of Nanoparticles Using All-Silicon Nanoantennas

Zhe Xu,[†] Wuzhou Song,[†,‡] and Kenneth B. Crozier*[,†,§]

[†]School of Physics, University of Melbourne, Victoria 3010, Australia

[‡]School of Materials Science and Engineering, Huazhong University of Science and Technology, Wuhan 430074, China

[§]Department of Electrical and Electronic Engineering, University of Melbourne, Victoria 3010, Australia

Supporting Information

ABSTRACT: The ability to optically trap nanoscale particles in a reliable and noninvasive manner is emerging as an important capability for nanoscience. Different techniques have been introduced, including plasmonic nanostructures. Nano-optical tweezers based on plasmonics face the problem of Joule heating, however, due to high losses in metals. Here we experimentally demonstrate the optical trapping and transport of nanoparticles using a nonplasmonic approach, namely, a silicon nanoantenna. We trap polystyrene nanoparticles with diameters of 20 and 100 nm and use fluorescence microscopy to track their positions as a function of time. We show that multiple nanoparticles can be trapped simultaneously with a single nanoantenna. We show that the infrared trapping laser beam also produces fluorescent emission from trapped nanoparticles via two-photon excitation. We present simulations of the nanoantenna that predict enhanced optical forces with insignificant heat generation. Our work demonstrates that silicon nanoantennas enable nanoparticles to be optically trapped without deleterious thermal heating effects.

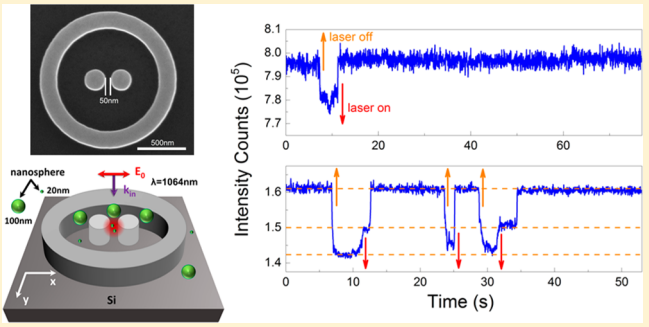

KEYWORDS: *optical trapping, silicon nanoantenna, thermal effect, nanoparticle, optical force*

Conventional optical tweezers provide an effective technique for the trapping of micrometer-sized particles[1−3] for various applications in nanoscience, utilizing optical forces exerted by focused laser beams. They face challenges, however, for the trapping of nanoparticles because the optical gradient force scales with the particle volume.[4] Furthermore, lenses obey the diffraction limit, and the focused laser spot sizes are thus approximately half the wavelength. This puts an upper limit to the maximum optical gradient force that can be applied to a nanoparticle of a given size, shape, and refractive index, for a given laser power. An additional consequence of the diffraction limit of conventional optical tweezers is that a trapped nanoparticle is localized to a region that is far larger (typically hundreds of nanometers for visible or infrared light) than the particle itself (nanoscale). To address these challenges, near-field optical trapping approaches using plasmonics[5−14] and other methods[15−17] have been investigated. Using plasmonic nanostructures, optical field distributions can be achieved with deeply subwavelength confinement and with field enhancement, leading to optical forces that are sufficient for the stable trapping of nanoparticles at relatively low optical powers. The trapping of various materials has been demonstrated with plasmonic nanotweezers, including polystyrene and silica beads,[9] gold nanoparticles,[7] proteins,[12] quantum dots,[13] and magnetic nanoparticles.[14] Plasmonic nanotweezers, however, exhibit Joule heating due to the strong absorption losses that occur in metals at optical frequencies.[18] This generally decreases trapping stability because it can lead to thermophoresis and convection, and even to boiling of the water (where the trapping is performed) and to specimen damage at high intensities.[11,19,20] Several works have sought to mitigate this issue. In ref 11, for example, Wang et al. demonstrated that heating can be reduced about 100-fold via integrating a high thermal conductivity heat sink structure with the plasmonic nanoantenna. In nanoaperture trapping,[21] the metallic film itself serves as a heat sink, thereby decreasing localized heating. While these approaches address this issue, temperature increases nonetheless occur. This motivates the development of a nonplasmonic approach to optical nanotweezers and is the subject of this study.

The need to decrease local heating has been emphasized for a lot of practical applications of nanostructures (and not only for nanotweezers), prompting recent theoretical and experimental investigations concerning all-dielectric nanoantennas.[22−25] These are made of low-loss high refractive index dielectrics, for example, silicon and germanium.[26] We note that we here refer to silicon and germanium nanoantennas as "dielectric nanoantennas" (rather than "semiconductor nanoantennas") to be consistent with the literature. Two of the key advantages they have over plasmonic nanoantennas are as

Received: September 5, 2018
Published: November 6, 2018

DOI: 10.1021/acsphotonics.8b01250
ACS Photonics 2018, 5, 4993−5001

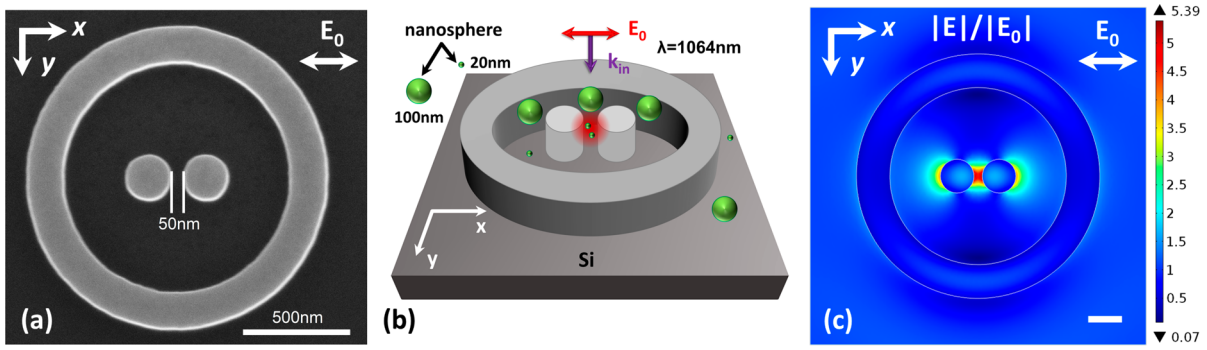

Figure 1. (a) SEM image (top-view) of a Si nanoantenna fabricated on a Si substrate. (b) Schematic illustration of optical trapping of nanospheres using all-Si nanoantennas. (c) Electric field enhancement in the center plane for plane wave illumination (*x*-polarized, 1064 nm). Scale bar: 200 nm.

follows. First, due to the low absorption losses, heat generation by the nanoantenna is low, and the temperature increases that occur can be much smaller than what would occur for a comparable plasmonic nanoantenna. The latter is particularly true if the dielectric nanoantenna is incorporated into a design that makes use of the high thermal conductivity of materials such as silicon to provide a heat sink functionality. Second, all-dielectric nanoantennas feature both strong electric and magnetic resonant modes ("hotspots"). For example, Bakker et al. showed that for an isolated silicon nanodimer (i.e., a pair of nanoparticles separated by a small gap), the hotspot in the gap can have either an electric or a magnetic character, depending on the polarization of the incident light.[27] Several works have recently employed these favorable attributes of dielectric nanoantennas for different applications. Silicon dimer antennas on glass substrates were employed to enhance fluorescence and Raman scattering from layers of molecules formed on them.[28] It has been furthermore demonstrated that silicon dimer nanoantennas enhance the fluorescence from single molecules.[29]

In this paper, we experimentally demonstrate the optical trapping of 20 and 100 nm (in diameter) polystyrene nanospheres (NSs) in water with a novel all-dielectric (silicon, Si) nanoantenna. This comprises a pair of identical Si cylinders separated by a 50 nm gap, an outer Si ring, and an underlying Si substrate (Figure 1a). Using fluorescence microscopy, we directly observe the optical trapping process and track the position and fluorescent emission of the trapped NS as a function of time. We perform simulations of the near-field distribution, optical force, potential energy, temperature rise, and fluid velocity. Our device provides significant benefits compared to previous plasmonic nano-optical tweezers, which are made of metals. First, at the trapping wavelength used here (λ = 1064 nm), Si has a relative permittivity whose real part is much larger than its imaginary part, significantly diminishing heating. Second, Si has a high thermal conductivity, so any generated heating is readily dissipated into the entire Si substrate, rather than into the surrounding environment. Furthermore, we report that the trapped nanospheres can be transported with respect to an array of Si nanoantennas. That is, by moving the Si chip with software control, the nanospheres can access different nanoantennas across the array. We observe the simultaneous trapping and transport of multiple NSs by a single nanoantenna. We also demonstrate that fluorescence from the trapped NSs can be excited in a one-photon process with light from a green laser (532 nm), but also in a two-photon process with light from the trapping laser (1064 nm). To the best of our knowledge, our results represent the first experimental realization of optical nano-tweezers based on all-dielectric nanoantennas.

Figure 1a displays a scanning electron micrograph (SEM) top-view image of one of our fabricated all-silicon nano-antennas. Each nanoantenna is composed of two identical Si cylinders separated by a 50 nm gap. The cylinders have 200 nm diameters and 200 nm heights. They are surrounded with a Si outer ring and are situated on a Si wafer. The ring has outer and inner radii of 725 and 525 nm, respectively, and a height of 200 nm. The Si nanoantennas are fabricated by electron beam lithography (EBL) and reactive ion etching on a Si wafer (see Supporting Information). We next provide some comments on the design. Cylinders with equal diameters and heights have similar optical properties to those of spheres and are readily fabricated. The outer ring in our design increases the near-field enhancement and thus the optical force. We situate the nanoantenna on a Si substrate, rather than for example glass, to achieve an all-Si device. The Si substrate acts as a good heat sink to minimize thermal effects[11] due to its high thermal conductivity ($\kappa_{Si} \approx 148$ W K^{-1} m^{-1}, $\kappa_{glass} \approx 1$ W K^{-1} m^{-1}, $\kappa_{water} \approx 0.58$ W K^{-1} m^{-1}).[30] The use of Si is motivated by its low light absorption and high refractive index at the trapping wavelength (1064 nm). Other favorable attributes of Si include its wide availability, low cost, and the existence of mature fabrication technologies. Figure 1b schematically illustrates the optical trapping of NSs of different diameters by the Si nanoantenna. We expect that it should be possible for NSs with diameters smaller than the gap width to be trapped in the gap center. We also expect that it should be possible for several of such NSs to be simultaneously trapped. Larger NSs on the other hand are expected to be blocked from the gap center due to steric hindrance from the nanoantenna morphology.[21] In Figure 1c, the electric field enhancement is plotted on an *xy*-plane that is halfway through the antenna. The medium above the Si is water. The Si nanoantenna is illuminated by a normally incident plane wave (1064 nm, *x*-polarized) from the water side. As shown in Figure 1c, the maximum enhancement occurs in the gap and takes a value of $|E|/|E_0| \approx 5.39$. Here $|E_0|$ is the electric field amplitude of the incident plane wave. It can be seen that there are three locations at which the electric fields are enhanced, with the gap region for the main maximum and the cylinder pair outer edges for the two secondary maxima. This potentially enables the simultaneous trapping of multiple nanoparticles. For comparison, we simulate the electric field enhancement for a gold (Au) nanoantenna on a glass substrate. The Au nanoantenna also consists of two

DOI: 10.1021/acsphotonics.8b01250
ACS Photonics 2018, 5, 4993−5001

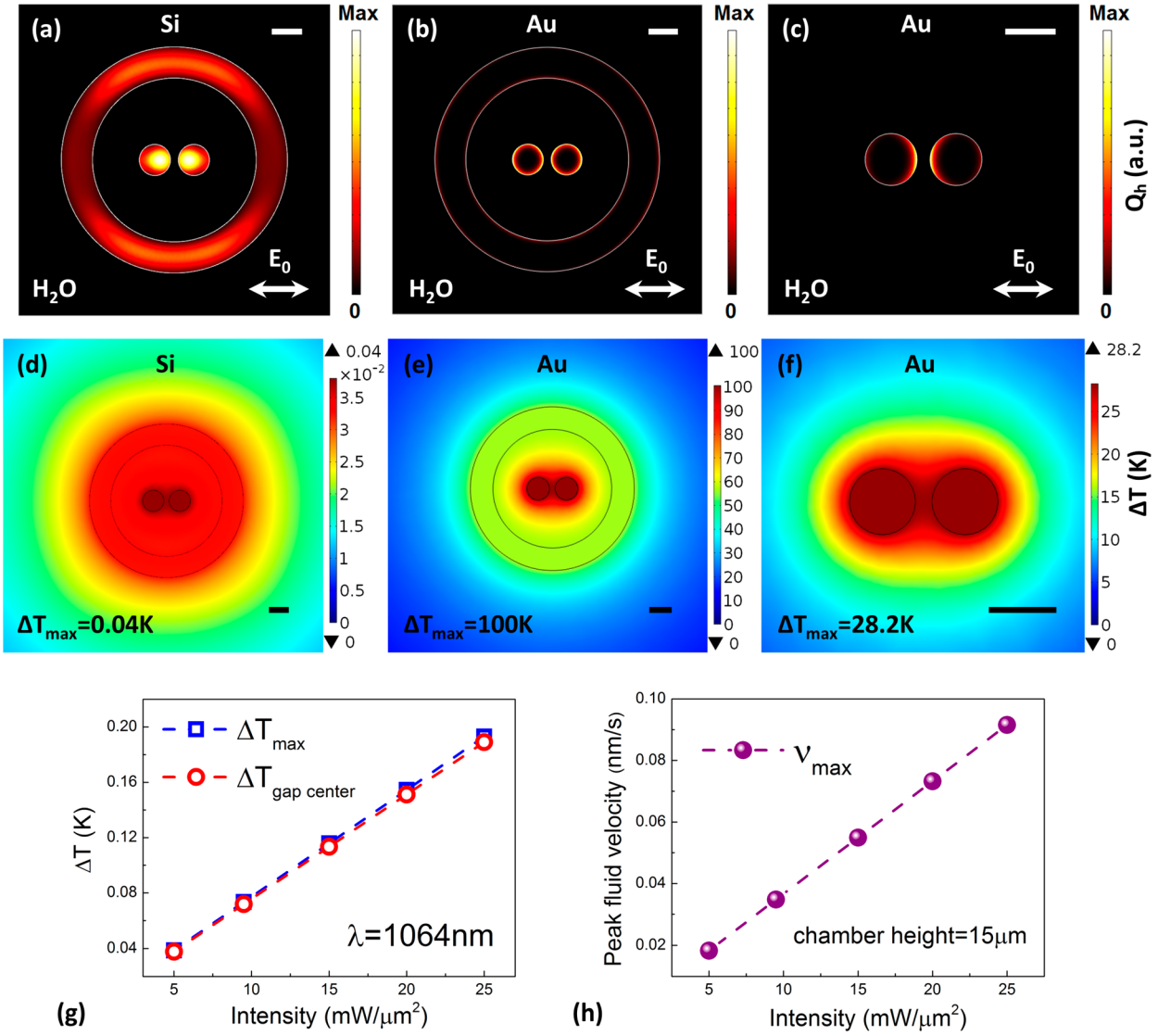

Figure 2. Heat power dissipation density around (a) a Si nanoantenna on a Si substrate, (b) a Au nanoantenna on a glass substrate, and (c) a Au cylinder nanodimer on a glass substrate. Steady state temperature increase profile around (d) a Si nanoantenna on a Si substrate, (e) a Au nanoantenna on a glass substrate, and (f) a Au cylinder nanodimer on a glass substrate. Panels a–f are plotted in the center plane of the nanostructures (z = −100 nm) with an illumination intensity I_0 = 5 mW/μm^2. Scale bar: 200 nm. (g) Peak (blue squares) and at gap center (red circles) temperature increases (in Si nanoantenna) vs trapping laser intensity. (h) Maximum convection velocity (near Si nanoantenna) vs trapping laser intensity. Chamber height is 15 μm.

identical cylinders and a ring, and these have the same dimensions as that of the Si nanoantenna considered. The results are presented in the Supporting Information and show an electric field enhancement of ∼9.23.[28]

We next report numerical simulations of the temperature rise of our all-Si nanoantennas and the water convection velocity field[11,20,31] when nanoantennas are illuminated at intensities typical of those used for experiments we report later. We consider three nanostructures: our all-Si nanoantenna on a Si substrate; a Au nanoantenna with the same dimensions on a glass substrate; and a Au cylinder dimer on a glass substrate. For the latter, the cylinders have the same dimensions as other nanoantennas (diameter = 200 nm, height = 200 nm, gap = 50 nm), and no ring structure is included. All designs have water superstrates and are illuminated at normal incidence with an x-polarized 1064 nm plane wave. In Figure 2a–c, we show the power dissipation density in a cross section through each nanostructure's center, at an intensity that is typical in experiments (I_0 = 5 mW/μm^2). Because the physical mechanisms that underlie the resonances of metallic and dielectric nanoantennas are different,[23,26,28] the power dissipation distributions are also different. For the case of Si (Figure 2a), most of the dissipated power is confined inside the individual cylinders and the ring. For the case of Au (Figure 2b,c), the power dissipation peaks close to the surface of nanoantenna. For both Si and Au nanostructures, the power dissipation is very small in the surrounding water. The difference between these power dissipation distributions can be understood from the sign of the relative permittivity of the nanoantenna, which is positive for Si and negative for Au.[26] It should be noted that the peak values of the scale bar are different (Figure 2a: ∼10^{13} W/m^3; Figure 2b,c: ∼10^{16} W/m^3). The steady state temperature rise distributions are plotted as Figure 2d–f. In Figure 2d, the simulation predicts the maximum temperature rise is ∼0.04 K on the plotted center cross section for the Si nanoantenna, which is very small. The

DOI: 10.1021/acsphotonics.8b01250
ACS Photonics 2018, 5, 4993−5001

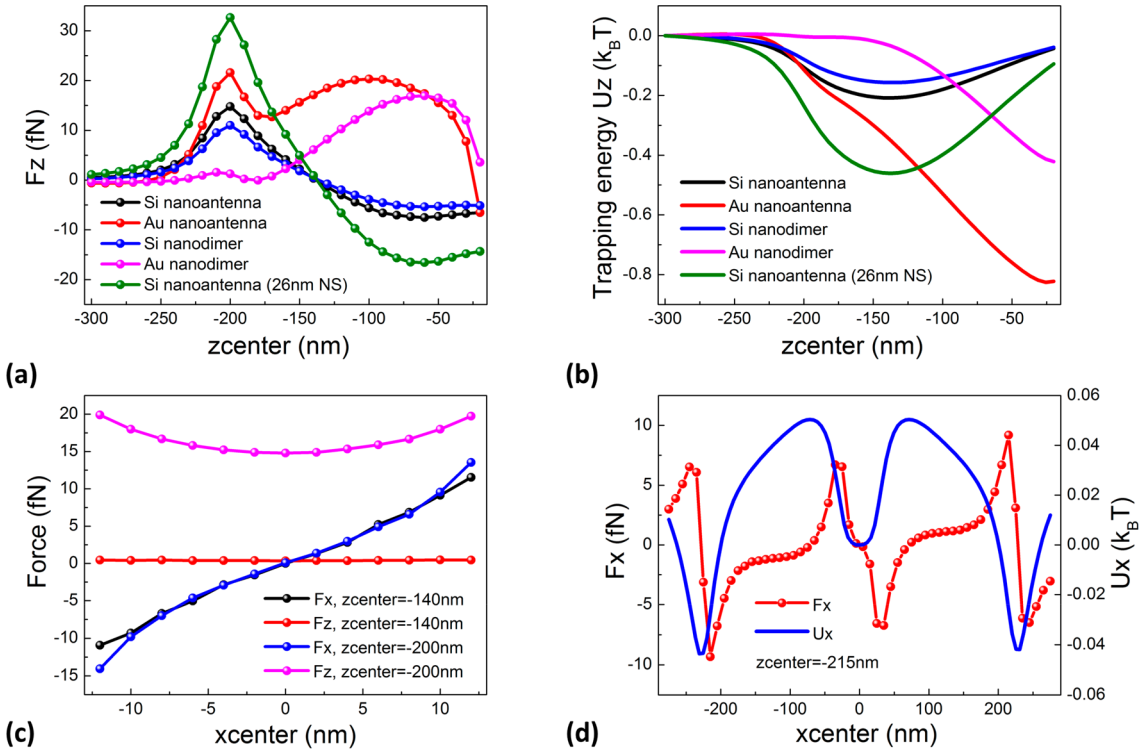

Figure 3. MST optical force and associated trapping energy on a polystyrene NS (n_{NS} = 1.6, d = 20 nm) for illumination intensity I_0 = 9.5 mW/μm^2. (a) Optical force F_z and (b) trapping energy U_z vs vertical position centered over the gap (x_{center} = y_{center} = 0). (c) F_x and F_z along the x-direction (y_{center} = 0) when moving along the middle (z_{center} = −140 nm) and edge (z_{center} = −200 nm) of the Si nanoantenna. (d) F_x and U_x vs NS position at 15 nm outside of Si nanoantenna along the x-axis (y_{center} = 0 nm, z_{center} = −215 nm). In panels b and d, $1k_BT = 4.05 \times 10^{-21}$ J.

simulation method used to predict this temperature rise and its assumptions are described in the Supporting Information. Figure 2e plots the simulation for the Au nanoantenna under the same illumination conditions, with the maximum temperature rise being ∼100 K. The temperature rise distribution for the Au dimer nanoantenna is plotted as Figure 2f and on the plotted cross section takes a maximum value of ∼28.2 K. The temperature rise for the Si nanoantenna is thus ∼3 orders of magnitude smaller than that predicted for the Au nanostructures. The reason for this is twofold. First, the absorption cross section of the Si nanoantenna is much lower than those of the Au nanoantennas.[18] Second, the Si nanoantenna is on a substrate (Si) with a much greater thermal conductivity than that of the Au nanoantennas (glass).[11] For all three nanostructures, the highest temperature rise zones are concentrated over the cylinder pair including the small gap in which the field enhancement is strong. In Figure 2g, we show the temperature rise of an all-Si nanoantenna versus trapping laser intensity. It can be seen that the maximum temperature increase (on nanoantenna surface) and the temperature increase in the nanoantenna center (i.e., water gap) are both very small. The fact that heating is low would allow high laser intensities to be used, for example, to explore nonlinear processes in trapped nanoparticles. In Figure 2h, the maximum water convection velocity around an all-Si nanoantenna is plotted versus trapping laser intensity. For the range of intensities considered, the peak velocity is only ∼0.02 nm/s, which is much smaller than what occurs for single plasmonic nanoantennas[20] (see Supporting Information). These results demonstrate that our all-Si nanoantennas produce local enhancement with negligible heat generation and ultralow fluid convection,[28] meaning that light-induced thermophoresis and convection have negligible contributions to the trapping.[20]

Plasmonic nanostructures[8,32] can overcome the diffraction limit and enhance trapping forces. Here we calculate the optical forces generated by our Si nanoantenna to consider its use as nanotweezers[33] for the optical trapping of nanoparticles. We use the finite element method package (FEM; COMSOL Multiphysics)[21] and the Maxwell stress tensor (MST)[34] analysis to determine the time-averaged forces.[35] The nanoparticle is a 20 nm polystyrene NS. The force is integrated in one dimension to obtain the trapping potential energy,[21] under the simplifying assumption that it is a conservative force. In Figure 3a, we show the vertical force F_z on the NS (20 and 26 nm diameter) versus its vertical center position (i.e., z_{center}). Four nanostructures are considered: our all-Si nanoantenna on a Si substrate; a Au nanoantenna with the same dimensions on a glass substrate; a Si cylinder dimer nanoantenna on a Si substrate; and a Au cylinder dimer nanoantenna on a glass substrate. For the Si and Au nanodimers, the cylinders have the same dimensions as other nanoantennas (diameter = 200 nm, height = 200 nm, gap = 50 nm), and no ring structures are included. They are all covered with water and illuminated with an x-polarized 1064 nm plane wave. Due to the difference of the near-field distributions (see Supporting Information), the force distributions are also different. For the Si case (all-Si nanoantenna and Si cylinder dimer), for $z_{center} < -140$ nm, the particle is attracted into the nanoantenna with F_z being positive, while for $z_{center} > -140$ nm, F_z is negative. This indicates that the vertical force guides NSs to around the middle of the antenna where the intensity reaches its maximum. The maximum forces occur at the antenna surface (z_{center} = −200 nm) where the field gradients are largest. It can

DOI: 10.1021/acsphotonics.8b01250
ACS Photonics 2018, 5, 4993−5001

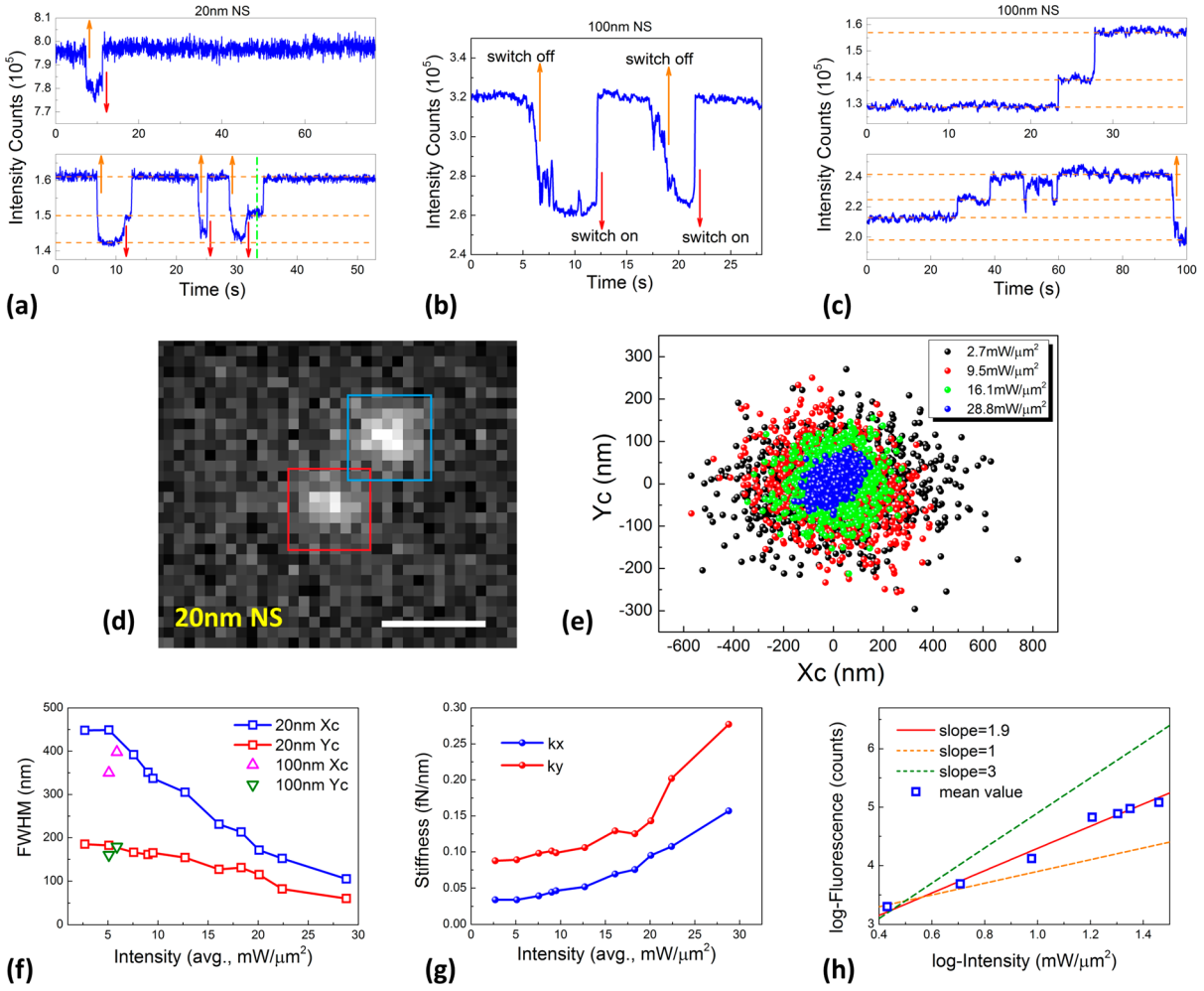

Figure 4. Fluorescence counts vs time for trapping of (a) one (top) and two (bottom) 20 nm NSs, (b) one 100 nm NS, and (c) two (top) and three (bottom) 100 nm NSs. Orange arrow: trapping laser is switched off. Red arrow: trapping laser is switched on. (a) Top: I_0 = 18.3 mW/μm^2, 25 × 25 pixels; bottom: I_0 = 9 mW/μm^2, 12 × 12 pixels; (b) I_0 = 5 mW/μm^2, 17 × 17 pixels; (c) top: I_0 = 5.9 mW/μm^2, 12 × 12 pixels; bottom: I_0 = 18.3 mW/μm^2, 15 × 15 pixels. (d) EM-CCD frame showing a pair of 20 nm NSs in the vicinity of a Si nanoantenna (time indicated by green dashed-dotted line in panel a). Blue box: nontrapped NS; red box: trapped NS. Scale bar: 1.6 μm. (e) Scatter plots of measured center position distribution (20 nm NS). (f) fwhms from Gaussian fitting of location scatter plots vs trapping laser intensity. (g) Calibrated effective transversal stiffness vs trapping laser intensity (20 nm NS). (h) Log–log plot of emitted fluorescence (with background subtracted) vs trapping laser intensity (20 nm NSs). Red solid line has a slope of 1.9. Slopes of the dashed lines indicate linear and cubic dependencies.

also be seen that larger NSs experience stronger optical forces, which is also expected from the dipole approximation.[4] The positive values of F_z for the Au nanoantenna and Au cylinder nanodimer indicate that the NSs are pulled into the nanostructures. For both the Si and Au designs, the outer ring enhances the force values compared with the cylinder dimer geometry. In Figure 3b, we show the corresponding effective trapping potential energy U_z.[21] This quantity is determined from Figure 3a with the line integration path being along the z-axis, from outside (z_{center} = −300 nm, U_z = 0) to inside each nanostructure (z_{center} = −20 nm). The Au nanoantenna produces a higher trapping potential energy than its Si counterpart, but with a much greater temperature rise (Figure 2). We next calculate the horizontal forces for the all-Si nanoantenna. In Figure 3c, we show F_z and F_x versus NS center location in the x-axis, with y_{center} = 0 nm. It can be seen that F_x is negative for x_{center} < 0 and F_x is positive for x_{center} > 0. This reveals that the NSs are primarily dragged to the edge surfaces of the antenna gap because of the unstable equilibrium at the gap center. In Figure 3d, we show F_x and U_x as a function of NS location outside of the antenna in the x-axis (y_{center} = 0 nm, z_{center} = −215 nm). The zero point of U_x is defined as being when the NS is in the antenna center (x_{center} = 0). Three energy wells can be seen: one around the small gap area and two near the cylinder pair outer edges. A consequence of the multiple potential wells is that it should be possible to trap multiple nanoparticles.

To study the trapping process, we perform direct observations with fluorescence microscopy, tracking the position of, and fluorescent emission from, polystyrene NSs in water trapped by our all-Si nanoantennas. The NSs have diameters of 20 and 100 nm. An infrared trapping laser with x-polarization (1064 nm, continuous wave) is tightly focused by an oil immersion microscope objective (100×, NA = 1.3) into a chamber including polystyrene NSs (FluoSpheres, Life Technologies), distilled water, and Tween 20 surfactant (to minimize sticking). The laser spot diameter is ∼1.2 μm. Another loosely focused green laser (532 nm), for fluorescence excitation, is introduced with the same optical path over a wide field-of-view, and the emitted fluorescence is detected with an

DOI: 10.1021/acsphotonics.8b01250
ACS Photonics 2018, 5, 4993−5001

electron multiplying camera (EM-CCD) after being passed through a set of filters. The EM-CCD camera is operated at 30 fps (frames per second). The green laser intensity at the sample is roughly 5 orders of magnitude smaller than that of the trapping beam. Experimental results showing the trapping of one or more NSs by the Si nanoantenna are provided as Supporting Movies 1−5. Here we display this trapping information in different formats to analyze the process. In Figure 4a−c, we show the recorded fluorescent emission counts integrated over a square cross section (of pixels) from every EM-CCD frame versus time. This cross section encompasses the illuminated Si nanoantenna. The 1064 nm laser is turned on and off at times that are marked by (red) downward- and (orange) upward-pointing arrows, respectively. The abrupt rises in fluorescence show single-particle trapping events, which is also verified by observing the movies. Figure 4a shows the optical trapping of a single NS (top, Supporting Movie 1) and two NSs (bottom, Supporting Movie 2). These NSs have diameters of 20 nm, which is smaller than the gap width. It is thus possible for a pair of such NSs to be trapped at the gap center. Figure 4b and c show the optical trapping of a single NS (Supporting Movie 3), two NSs (top, Supporting Movie 4), and three NSs (bottom, Supporting Movie 5). These have diameters of 100 nm. This is larger than the gap width, so it is not possible for such an NS to be trapped at a gap center. The reversibility of trapping and release confirms that the process is driven by the optical forces. We demonstrate that the trapped NSs are not being adsorbed to the Si antenna surface by nonoptical means[36−38] via switching the trapping laser off and observing that the NSs are released. Switching the laser on again results in the NSs being trapped again immediately if they are still in the illuminated nanoantenna vicinity. In Figure 4d, a typical frame from a trapping movie is displayed, showing a pair of NSs (each 20 nm diameter, with white appearance) in the vicinity of a Si nanoantenna. We analyze the movies to find the positions of the NSs versus time and perform quantitative analysis. In Figure 4e, we show scatter plots of the position (centroid) of single trapped NSs (20 nm) at four different intensities. At each intensity, data are collected over a period of 33 s for 1000 frames. The NSs' center locations are tracked with a radial-symmetry-based particle localization algorithm.[39] Our results demonstrate that the higher laser intensities with stronger trapping forces contribute to the tighter particle spatial localizations. In Figure 4f, we show the corresponding full widths at half-maximum (fwhms) of Gaussian function fitting distributions. As discussed earlier, our simulations predict that the trapping energy for 20 nm NSs is smaller than the thermal energy k_BT ($1k_BT = 4.05 \times 10^{-21}$ J, k_B is the Boltzmann constant, and $T = 293.15$ K is temperature). Our experimental results nonetheless show the optical trapping of 20 nm (and 100 nm) NSs. Figure 4f presents data on the trapping of the smaller (20 nm) NSs over a wide range of intensities. For comparison, the experiment is repeated with the larger (100 nm) NSs at two intensities near the lower end of the range. Interestingly, the fwhms for the 100 nm NSs are comparable to those of the 20 nm NSs at around the same intensity. This runs counter to an expectation that the optical gradient force would be larger for the 100 nm NSs, due to their greater polarizability. One possible explanation is that the 100 nm NSs are limited in the gradient force that they can experience because they cannot enter the gap center (around which the electric field intensity reaches a maximum). We next study the trapping behavior by considering the trapping stiffness. From Figure 3d and the related discussion, it can be seen that the potential produced by the antenna is clearly not harmonic. It is nonetheless instructive to determine the "effective" trapping stiffnesses[40] along the x- and y-axes, using $k_{x,\mathrm{eff}} = k_BT/\mathrm{var}(x)$ and $k_{y,\mathrm{eff}} = k_BT/\mathrm{var}(y)$, respectively. Here, $\mathrm{var}(x)$ and $\mathrm{var}(y)$ are the variances in position in the x- and y-axes, respectively. The "effective" trapping stiffness can be thought of as the stiffness that would be possessed by an ideal harmonic trap that produces the same localization (position variance) as our Si nanoantenna. The results are shown in Figure 4g and are extracted from the measured variances of 20 nm NS positions using a correction method[41] that considers the issue of motion blur during the finite camera exposure time (∼30 ms). It can be seen that the effective trap stiffness increases with trapping laser intensity. This relationship is not the simple linear increase that would be expected for an ideal harmonic trap in which the optical gradient force and the Brownian force act. Several factors could account for this. First, as discussed, the potential is not strictly harmonic. Second, in our Si nanoantenna tweezers, the NS to be trapped cannot move freely in all directions, but rather is restricted by the antenna boundaries.[9,13,21] Third, there may be other effects such as particle−surface interactions[42] and electrostatic effects.[43] One might also consider that heating, and the resultant thermophoresis[44] and convection,[20] at higher intensities might play a role. We do not think that this is the case, however, as our modeling predicts a negligible temperature rise. Recently, Shoji et al. reported optical trapping of 500 nm polystyrene particles using Si nanopyramids.[45] We note that these particles have volumes ∼4 orders of magnitude larger than those of the polystyrene NSs (20 nm diameter) we employ.

We next show not only that single NSs can be optically trapped by the trapping beam but also that this (infrared) beam can excite fluorescence from the single NSs by two-photon absorption (TPA). In Figure 4h, we plot (log−log format) the measured mean values of fluorescence intensity counts from various single trapped 20 nm NSs with noise subtracted (i.e., background intensity from green laser and intrinsic noise from system) versus trapping laser intensity. Each data point is obtained by averaging the fluorescent emission extracted from 1000 frames over a 30 × 30 pixel cross section. It can be seen that the experimental measurements are consistent with the quadratic dependence of two-photon absorption,[13,46−48] with the best fit to the log−log plot having slope 1.9. Further results that compare the fluorescence from trapped NSs produced when both the infrared and green lasers are on and when only the infrared laser is on are shown in the Supporting Information. We notice that the modification to the trapping process via the nonlinear refractive index of the NS is expected to be insignificant, as the nonlinear refractive index of polystyrene is much smaller than its linear part.[46]

The technique of optical manipulation represents an important tool in nanotechnology.[33,49] Here we provide a method for optical manipulation that also demonstrates the repeatability of the trapping process as it is based on continually trapping, releasing, then retrapping NSs. We show that the trapped NSs (100 nm diameter) can be transported through the movement of the Si chip by computer software control (that is, access different nanoantennas of the array). Our device can achieve the controlled transport of either a single NS or a pair of NSs. Figure 5a displays the SEM

DOI: 10.1021/acsphotonics.8b01250
ACS Photonics 2018, 5, 4993−5001

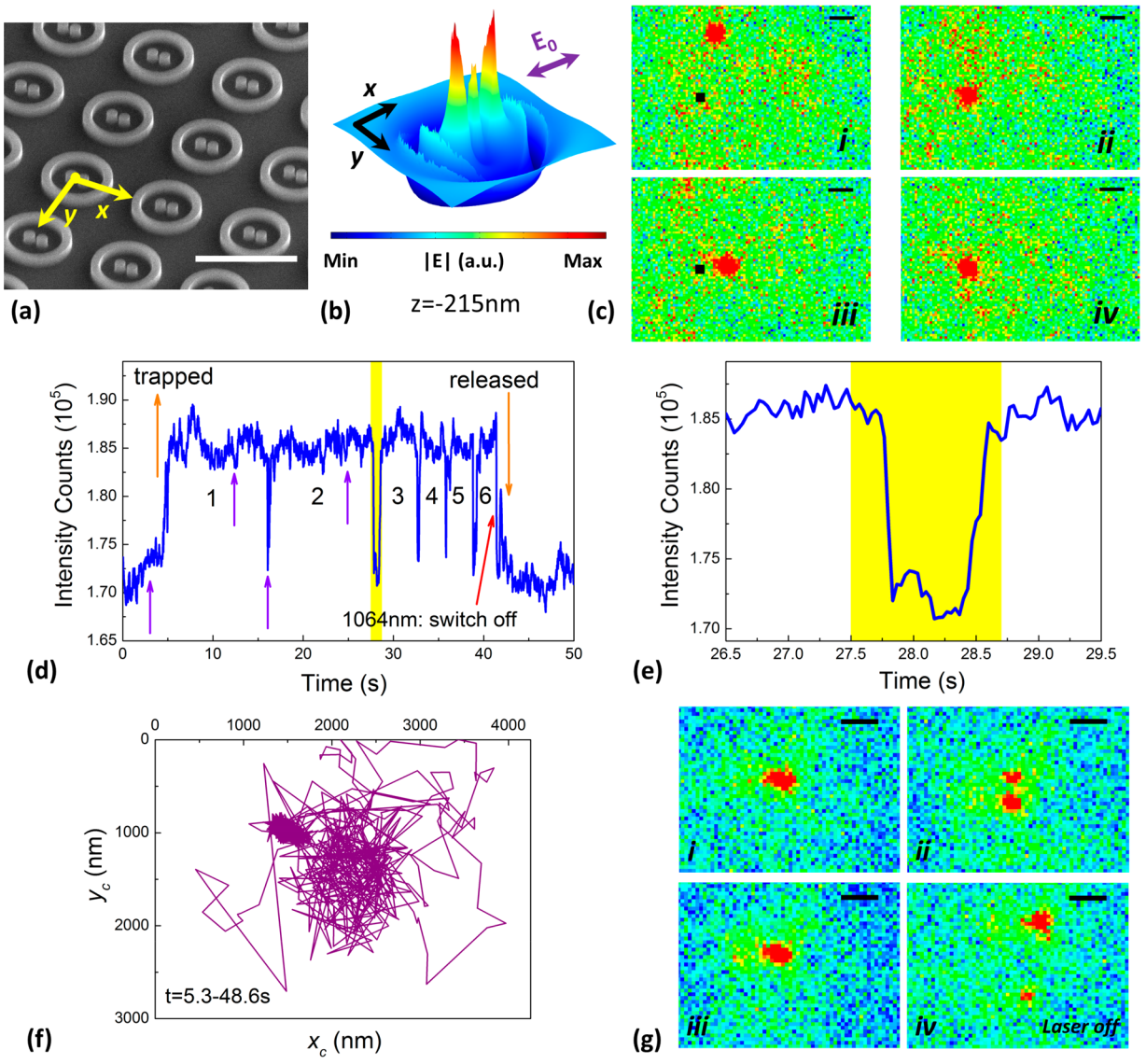

Figure 5. (a) SEM picture (45° tilt) of Si nanoantenna arrays. Periodicities of the antennas in *x*- and *y*-axes are both 2 μm. Scale bar: 2 μm. (b) Electric field profile in the *xy*-plane, with 15 nm height above the antenna surface. (c) EM-CCD images (time marked by violet arrows in d) illustrating trapping and transport of an individual 100 nm NS. Illuminated nanoantenna and focused trapping beam: black square. Scale bar: 1.6 μm. (d) Fluorescent emission counts vs time for individual NS trapping, release, and transport. (e) Zoom-in of panel d illustrating NS release, free diffusion, and move from one nanoantenna to another. (f) Corresponding NS location scatter plots analyzed from EM-CCD images. For panels c–f, I_0 = 5 mW/μm^2. (g) EM-CCD images illustrating the simultaneous trapping, release, and transport of a pair of 100 nm NSs. I_0 = 8.3 mW/μm^2. Scale bar: 1.6 μm.

image of a representative Si nanoantenna array. Each antenna has the same design as that used in trapping experiments (Figure 1a). The antennas are formed in square arrays with a period of 2 μm. As the gap is narrower than the NSs' diameters, the NSs are not trapped in the center of the small gap. In Figure 5b, we plot the electric field profile in the *xy*-plane at a distance of 15 nm from the antenna surface. There are two main maxima around the Si cylinder pair outer ends and one minor maximum around the middle gap. The schematic of the experimental configuration is given in the Supporting Information. We begin by discussing our demonstration of the transport of a single NS across the array. This process is shown as Supporting Movie 6, from which four frames are shown as Figure 5c. At the beginning, the NS moves randomly with Brownian motion (Figure 5c, time *i*). The first Si nanoantenna is illuminated by the focused trapping beam, and its location is pointed by a black square. When the NS moves in the first Si nanoantenna's vicinity (time *ii*), it can be trapped by optical forces of the Si nanoantenna. At time *iii*, the piezoelectric stage has moved the Si nanoantenna chip along the *x*-axis by 2 μm by software control, meaning that the second nanoantenna within the array is irradiated. This leads to the NS trapped by the first antenna being released immediately and then moving freely as Brownian diffusion, until it is recaptured by the second illuminated nanoantenna before time *iv*. In this way, the nanoparticle can access various nanoantennas in the array along an arbitrary path. In Figure 5d, we show a typical fluorescent intensity count versus time integrated from a 14 × 14 pixel cross section (~2.24 μm × 2.24 μm) over the trapping location. The trapping of the NS results in the fluorescence increasing in an approximately step-like fashion. Four violet arrows in Figure 5d

DOI: 10.1021/acsphotonics.8b01250
ACS Photonics 2018, 5, 4993−5001

denote the times (*i*–*iv*) of four frames of Figure 5c. In the experiment of Figure 5d, the NS has been made to access six different Si nanoantennas. The distance between the first and last nanoantenna is thus 10 μm. Further insight of the movement process could be found in Figure 5e. The yellow shaded area represents the approximate time duration when the NS is diffusing, between being released by the one antenna and recaptured by the next antenna. In Figure 5f, we display a plot of the tracked NS center locations for ∼43 s, as determined by processing 1300 EM-CCD frames.[39] The cluster at ∼(1500 nm, 1000 nm) represents the NS being trapped by six antennas. There is also a larger cluster at ∼(2250 nm, 1500 nm). This can be understood as follows. When the piezoelectric stage is moved, the first nanoantenna on which the NS is trapped moves out of the focal spot of the trapping laser. The NS is thus released from the first antenna and moves randomly before being pulled onto the second antenna, which is now within the focal spot of the trapping laser. This larger cluster represents the trajectories that occur during this process. We next show an example (Supporting Movie 7) of a pair of NSs being simultaneously trapped (Figure 5g, time *i*), released (because of the movement of Si chip of 18 μm, Figure 5g, time *ii*), and retrapped (by a new nanoantenna, Figure 5g, time *iii*). NSs are released from the nanoantennas when the trapping laser is switched off (Figure 5g, time *iv*). The ability of the nanoantenna to trap multiple NSs originates from the fact that it supports several hotspots. Our results suggest the future possibility of integrating Si nanoantenna arrays with microfluidic systems for lab-on-a-chip manipulation.

In this work, we demonstrate optical nanotweezers based on all-dielectric (Si) nanoantennas, for the first time to the best of our knowledge. Although the electric field enhancements (and thus optical forces) they provide are modest in comparison to those provided by plasmonic nanotweezers, we nonetheless demonstrate that they are sufficient to trap NSs with diameters down to 20 nm. Furthermore, the fact that absorption loss (and thus heating) is much smaller for our Si nanoantennas than plasmonic nanotweezers means that higher laser intensities can be used. This both permits high optical trapping forces and allows other phenomena that occur at high intensities to be investigated. One example of the latter that we study in this work is two-photon absorption. Using fluorescence microscopy, we perform nanoparticle tracking experiments, including position distribution and fluorescent emission. We perform a quantitative analysis of the trapped particle dynamics in the vicinity of silicon nanoantennas. In addition, we report the transport of an individual polystyrene nanoparticle within the Si nanoantenna array. Numerical simulations are performed to better understand these findings. Our results verify that silicon nanoantennas are robust as nano-optical tweezers with negligible local heating. We anticipate a number of topics that could be fruitful for future investigation, with two examples as follows. First, it would be interesting to develop all-dielectric nanotweezers for the manipulation of other nanomaterials, such as quantum dots, molecules, and nanodiamonds. Second, based on investigations with optical tweezers, it has been suggested that the electric double-layer coating of nanoparticles (sub-100 nm) may have a significant role in their optical trapping behavior.[43] To understand the trapping process in Si nanoantennas in a complete fashion, theoretical and experimental investigations of this and other interactions could be performed.

■ ASSOCIATED CONTENT

Supporting Information

The Supporting Information is available free of charge on the ACS Publications website at DOI: 10.1021/acsphotonics.8b01250.

Detailed descriptions of the device fabrication, microfluidic chamber preparation, experimental setup, simulation methods, and additional numerical and experimental figures (PDF)

Movie showing optical trapping of a single 20 nm NS (AVI)

Movie showing optical trapping of two 20 nm NSs (AVI)

Movie showing optical trapping of a single 100 nm NS (AVI)

Movie showing optical trapping of two 100 nm NSs (AVI)

Movie showing optical trapping of three 100 nm NSs (AVI)

Movie showing optical trapping and transport of a single 100 nm polystyrene nanosphere (AVI)

Movie showing optical trapping and transport of two 100 nm polystyrene nanospheres (AVI)

■ AUTHOR INFORMATION

Corresponding Author

*E-mail: kcrozier@unimelb.edu.au.

ORCID

Kenneth B. Crozier: 0000-0003-0947-001X

Author Contributions

Z.X. and K.B.C. designed the experiment, discussed the results, and wrote the manuscript. Z.X. performed trapping experiments, simulation, and data analysis. W.S. performed nanoantenna design and fabrication. W.S. designed and constructed experimental setup.

Notes

The authors declare no competing financial interest.

■ ACKNOWLEDGMENTS

This research was sponsored in part by the Australian Research Council (DP150103736, DP180104141, and FT140100577), by the Victorian Endowment for Science, Knowledge and Innovation (VESKI), and by the Laby Foundation.

■ REFERENCES

(1) Ashkin, A. Acceleration and trapping of particles by radiation pressure. *Phys. Rev. Lett.* **1970**, *24*, 156–159.

(2) Grier, D. G. A revolution in optical manipulation. *Nature* **2003**, *424*, 810–816.

(3) Neuman, K. C.; Block, S. M. Optical trapping. *Rev. Sci. Instrum.* **2004**, *75*, 2787–2809.

(4) Spesyvtseva, S. E. S.; Dholakia, K. Trapping in a material world. *ACS Photonics* **2016**, *3*, 719–736.

(5) Grigorenko, A.; Roberts, N.; Dickinson, M.; Zhang, Y. Nanometric optical tweezers based on nanostructured substrates. *Nat. Photonics* **2008**, *2*, 365–370.

(6) Juan, M. L.; Gordon, R.; Pang, Y.; Eftekhari, F.; Quidant, R. Self-induced back-action optical trapping of dielectric nanoparticles. *Nat. Phys.* **2009**, *5*, 915–919.

(7) Zhang, W.; Huang, L.; Santschi, C.; Martin, O. J. Trapping and sensing 10 nm metal nanoparticles using plasmonic dipole antennas. *Nano Lett.* **2010**, *10*, 1006–1011.

(8) Juan, M. L.; Righini, M.; Quidant, R. Plasmon nano-optical tweezers. *Nat. Photonics* **2011**, *5*, 349−356.
(9) Pang, Y.; Gordon, R. Optical trapping of 12 nm dielectric spheres using double-nanoholes in a gold film. *Nano Lett.* **2011**, *11*, 3763−3767.
(10) Berthelot, J.; Aćimović, S.; Juan, M.; Kreuzer, M.; Renger, J.; Quidant, R. Three-dimensional manipulation with scanning near-field optical nanotweezers. *Nat. Nanotechnol.* **2014**, *9*, 295−299.
(11) Wang, K.; Schonbrun, E.; Steinvurzel, P.; Crozier, K. B. Trapping and rotating nanoparticles using a plasmonic nano-tweezer with an integrated heat sink. *Nat. Commun.* **2011**, *2*, 469.
(12) Pang, Y.; Gordon, R. Optical trapping of a single protein. *Nano Lett.* **2012**, *12*, 402−406.
(13) Jensen, R. A.; Huang, I. C.; Chen, O.; Choy, J. T.; Bischof, T. S.; Lončar, M.; Bawendi, M. G. Optical trapping and two-photon excitation of colloidal quantum dots using bowtie apertures. *ACS Photonics* **2016**, *3*, 423−427.
(14) Xu, H.; Jones, S.; Choi, B. C.; Gordon, R. Characterization of individual magnetic nanoparticles in solution by double nanohole optical tweezers. *Nano Lett.* **2016**, *16*, 2639−2643.
(15) Yang, A. H.; Moore, S. D.; Schmidt, B. S.; Klug, M.; Lipson, M.; Erickson, D. Optical manipulation of nanoparticles and biomolecules in sub-wavelength slot waveguides. *Nature* **2009**, *457*, 71−75.
(16) Lin, S.; Schonbrun, E.; Crozier, K. B. Optical manipulation with planar silicon microring resonators. *Nano Lett.* **2010**, *10*, 2408−2411.
(17) Mandal, S.; Serey, X.; Erickson, D. Nanomanipulation using silicon photonic crystal resonators. *Nano Lett.* **2010**, *10*, 99−104.
(18) Baffou, G.; Quidant, R. Thermo-plasmonics: using metallic nanostructures as nano-sources of heat. *Laser Photonics Rev.* **2013**, *7*, 171−187.
(19) Bendix, P. M.; Reihani, S. N. S.; Oddershede, L. B. Direct measurements of heating by electromagnetically trapped gold nanoparticles on supported lipid bilayers. *ACS Nano* **2010**, *4*, 2256−2262.
(20) Donner, J. S.; Baffou, G.; McCloskey, D.; Quidant, R. Plasmon-assisted optofluidics. *ACS Nano* **2011**, *5*, 5457−5462.
(21) Xu, Z.; Song, W.; Crozier, K. B. Direct particle tracking observation and Brownian dynamics simulations of a single nanoparticle optically trapped by a plasmonic nanoaperture. *ACS Photonics* **2018**, *5*, 2850−2859.
(22) Krasnok, A. E.; Miroshnichenko, A. E.; Belov, P. A.; Kivshar, Y. S. All-dielectric optical nanoantennas. *Opt. Express* **2012**, *20*, 20599−20604.
(23) Albella, P.; Poyli, M. A.; Schmidt, M. K.; Maier, S. A.; Moreno, F.; Sáenz, J. J.; Aizpurua, J. Low-loss electric and magnetic field-enhanced spectroscopy with subwavelength silicon dimers. *J. Phys. Chem. C* **2013**, *117*, 13573−13584.
(24) Albella, P.; Alcaraz de la Osa, R.; Moreno, F.; Maier, S. A. Electric and magnetic field enhancement with ultralow heat radiation dielectric nanoantennas: considerations for surface-enhanced spectroscopies. *ACS Photonics* **2014**, *1*, 524−529.
(25) Kuznetsov, A. I.; Miroshnichenko, A. E.; Brongersma, M. L.; Kivshar, Y. S.; Luk'yanchuk, B. Optically resonant dielectric nanostructures. *Science* **2016**, *354*, aag2472.
(26) Decker, M.; Staude, I. Resonant dielectric nanostructures: a low-loss platform for functional nanophotonics. *J. Opt.* **2016**, *18*, 103001.
(27) Bakker, R. M.; Permyakov, D.; Yu, Y. F.; Markovich, D.; Paniagua-Domínguez, R.; Gonzaga, L.; Samusev, A.; Kivshar, Y.; Luk'yanchuk, B.; Kuznetsov, A. I. Magnetic and electric hotspots with silicon nanodimers. *Nano Lett.* **2015**, *15*, 2137−2142.
(28) Caldarola, M.; Albella, P.; Cortés, E.; Rahmani, M.; Roschuk, T.; Grinblat, G.; Oulton, R. F.; Bragas, A. V.; Maier, S. A. Non-plasmonic nanoantennas for surface enhanced spectroscopies with ultra-low heat conversion. *Nat. Commun.* **2015**, *6*, 7915.
(29) Regmi, R.; Berthelot, J.; Winkler, P. M.; Mivelle, M.; Proust, J.; Bedu, F., d. r.; Ozerov, I.; Begou, T.; Lumeau, J.; Rigneault, H. All-dielectric silicon nanogap antennas to enhance the fluorescence of single molecules. *Nano Lett.* **2016**, *16*, 5143−5151.
(30) Haynes, W. M. *CRC Handbook of Chemistry and Physics*; CRC Press, 2014.
(31) Wang, K.; Crozier, K. B. Plasmonic trapping with a gold nanopillar. *ChemPhysChem* **2012**, *13*, 2639−2648.
(32) Shoji, T.; Tsuboi, Y. Plasmonic optical tweezers toward molecular manipulation: tailoring plasmonic nanostructure, light source, and resonant trapping. *J. Phys. Chem. Lett.* **2014**, *5*, 2957−2967.
(33) Maragò, O. M.; Jones, P. H.; Gucciardi, P. G.; Volpe, G.; Ferrari, A. C. Optical trapping and manipulation of nanostructures. *Nat. Nanotechnol.* **2013**, *8*, 807.
(34) Novotny, L.; Hecht, B. *Principles of Nano-Optics*; Cambridge University Press, 2012.
(35) Ploschner, M.; Mazilu, M.; Krauss, T. F.; Dholakia, K. Optical forces near a nanoantenna. *J. Nanophotonics* **2010**, *4*, 041570.
(36) Liang, Y.; Hilal, N.; Langston, P.; Starov, V. Interaction forces between colloidal particles in liquid: Theory and experiment. *Adv. Colloid Interface Sci.* **2007**, *134*, 151−166.
(37) Parsegian, V. A. *Van der Waals Forces: A Handbook for Biologists, Chemists, Engineers, and Physicists*; Cambridge University Press, 2005.
(38) Padding, J.; Louis, A. Hydrodynamic interactions and Brownian forces in colloidal suspensions: Coarse-graining over time and length scales. *Phys. Rev. E* **2006**, *74*, 031402.
(39) Parthasarathy, R. Rapid, accurate particle tracking by calculation of radial symmetry centers. *Nat. Methods* **2012**, *9*, 724−726.
(40) Tanaka, Y.; Kaneda, S.; Sasaki, K. Nanostructured potential of optical trapping using a plasmonic nanoblock pair. *Nano Lett.* **2013**, *13*, 2146−2150.
(41) Wong, W. P.; Halvorsen, K. The effect of integration time on fluctuation measurements: calibrating an optical trap in the presence of motion blur. *Opt. Express* **2006**, *14*, 12517−12531.
(42) Schein, P.; Kang, P.; O'Dell, D.; Erickson, D. Nanophotonic force microscopy: characterizing particle−surface interactions using near-field photonics. *Nano Lett.* **2015**, *15*, 1414−1420.
(43) Rodríguez-Sevilla, P.; Prorok, K.; Bednarkiewicz, A.; Marqués, M. I.; García-Martín, A.; García Solé, J.; Haro-González, P.; Jaque, D. Optical forces at the nanoscale: size and electrostatic effects. *Nano Lett.* **2018**, *18*, 602−609.
(44) Duhr, S.; Braun, D. Why molecules move along a temperature gradient. *Proc. Natl. Acad. Sci. U. S. A.* **2006**, *103*, 19678−19682.
(45) Shoji, T.; Mototsuji, A.; Balčytis, A.; Linklater, D.; Juodkazis, S.; Tsuboi, Y. Optical tweezing and binding at high irradiation powers on black-Si. *Sci. Rep.* **2017**, *7*, 12298.
(46) Sutherland, R. L. *Handbook of Nonlinear Optics*; CRC Press, 2003.
(47) Florin, E. L.; Pralle, A.; Hörber, J. H.; Stelzer, E. H. Photonic force microscope based on optical tweezers and two-photon excitation for biological applications. *J. Struct. Biol.* **1997**, *119*, 202−211.
(48) Jauffred, L.; Oddershede, L. B. Two-photon quantum dot excitation during optical trapping. *Nano Lett.* **2010**, *10*, 1927−1930.
(49) Gao, D.; Ding, W.; Nieto-Vesperinas, M.; Ding, X.; Rahman, M.; Zhang, T.; Lim, C.; Qiu, C. W. Optical manipulation from the microscale to the nanoscale: fundamentals, advances and prospects. *Light: Sci. Appl.* **2017**, *6*, e17039.

DOI: 10.1021/acsphotonics.8b01250
ACS Photonics 2018, 5, 4993−5001

Supporting Information

Optical Trapping of Nanoparticles Using All-Silicon Nanoantennas

Zhe Xu,[†] *Wuzhou Song,*[†,‡] *and Kenneth B. Crozier**[*,†,§]

[†]School of Physics, University of Melbourne, Victoria 3010, Australia

[‡]School of Materials Science and Engineering, Huazhong University of Science and Technology, Wuhan 430074, China

[§]Department of Electrical and Electronic Engineering, University of Melbourne, Victoria 3010, Australia

Corresponding Author

*E-mail: kcrozier@unimelb.edu.au.

Methods

Device fabrication and chamber preparation. The Si nanoantennas studied in this paper are fabricated by standard electron beam lithography (EBL) and inductively coupled plasma reactive ion etching (ICP-RIE) on an Si wafer (Virginia Semiconductor Inc.). The resist used is ZEP520 (Zeon Chemicals). After etching, residual resist is removed, resulting in silicon nanoantenna arrays.

The microfluidic chamber (4 mm × 16 mm) is formed from photoresist on a 150 μm thick microscope glass coverslip as follows. The glass coverslip is first sonicated in water, baked on a hot plate to dry it, and cleaned in an oxygen plasma to remove particles etc. from the surface. This is followed by photoresist (AZ9260) coating, photolithography and development. The photoresist thickness is determined by the rotation speed of spin coater and measured with an optical profilometer. The photoresist is applied onto the cleaned coverslip while it is spinning at 500 rpm for 10 s to allow it to spread. The coverslip is then spun at 1000 rpm for 60 s, thereby resulting in a photoresist thickness of ~ 15 μm. Holes are drilled in the Si chip containing the nanoantennas to allow tubing to be added later. The Si chip is washed with acetone and rinsed with isopropanol and distilled water. It is then glued to the glass coverslip containing the microfluidic chamber with UV-cured optical adhesive, resulting in the chamber being closed. Polyethylene tubing to the Si chip is used to deliver fluid into the channel.

Trapping experiments. The experimental setup is based on an inverted optical microscope (Nikon TE2000). The optical trapping process is monitored by observing the nanosphere fluorescence after a set of filters (dichroic mirrors and shortpass filters) with an electron multiplying camera (EM-CCD, ProEM-HS: 512×512, Princeton Instruments) operated at 30 fps with an exposure time of ~ 30 ms. An optical beam shutter is used to switch on and off the light

from the continuous wave trapping laser (Laser Quantum Ventus 1064). A half-wave plate (λ_0 = 1064 nm) is used to rotate the polarization of the trapping laser beam. The *x*-polarized trapping beam is collimated and then focused by an oil immersion objective (Nikon Plan Fluorite Oil Immersion Objective, 100×, NA = 1.3) into a ~ 15 μm thick perfusion chamber (4 mm × 16 mm). The sample is mounted upside-down and aligned using a piezoelectric stage with a subnanometer position resolution. The focal spot diameter is ~ 1.2 μm. A loosely focused green laser (532 nm) is projected along the same optical path to excite fluorescence. The intensity at the sample due to the green laser is approximately five orders of magnitude smaller than that of the trapping beam. We thus expect that the contributions of the green laser to local heating and optical forces are negligible. The polystyrene nanospheres (FluoSpheres, 20 nm or 100 nm diameter, carboxylate-modified, Life Technologies) are suspended in distilled water with a trace amount of Tween 20 surfactant added, and the diluted suspension is ultrasonicated using a bath sonicator and further passed through a filter to remove aggregates, etc. The nanospheres have a coefficient of variation of about 20% for 20 nm and 5% for 100 nm respectively, according to the manufacturer (Life Technologies). The transmission of oil objective to the focal plane at 1064 nm is ~ 55%. Before the experiments, the mixture of water with Tween 20 is flowed through the channel to prevent nonspecific binding. Each experiment is done with freshly made suspension. Each pixel on the EM-CCD sensor array is 16 μm × 16 μm, which translates to around 160 nm × 160 nm in the focal plane with the 100× magnification objective.

Numerical calculations. Three-dimensional simulations are performed by the finite element method (FEM) using COMSOL Multiphysics. We use the "Wave Optics Module" to solve the near field distribution and for force determination. We begin by finding the background field ($|E_b|$) between substrate (Si or glass) and water space. We then perform a scattered field

simulation with the nanoantenna (Si or Au) being the scatterer. We use perfectly matched layers (PMLs) at the boundaries of the simulation space. To calculate the optical force with the MST, the nanoantenna and a single NS are introduced as two scatterers in the simulation. The optical trapping force on the NS is obtained by integrating the MST over its surface. The trapping energy is determined from the force map using the PDE module (partial differential equation) by solving the following equation: $-\nabla U = \vec{F}$. The refractive indices of water, glass and polystyrene are taken as 1.33, 1.45 and 1.6 respectively. The optical constant of Si is taken from Palik[1] and the optical constant of Au is taken from the data of Johnson and Christy.[2]

We use the heat transfer and laminar flow modules to solve the temperature rise distribution and fluid dynamics problems (here for steady state). This is performed as follows. The absorbed power in the Si cylinder dimer, in the Si ring, and in a region of the underlying Si substrate that has dimensions 2 μm × 2 μm × 1 μm (along *x*, *y*, *z* axes) is found from the electromagnetic simulations described above. This absorbed power is then taken as heat source power in the subsequent temperature rise distribution calculation. The heat source power is assumed to be evenly distributed, i.e., has the same density, over the Si cylinder dimer, over the Si ring and over the underlying region of the substrate (2 μm × 2 μm × 1 μm). While additional optical power is absorbed deeper into the substrate (i.e., beyond 1 μm), this absorbed power has an effect upon the temperature rise at the surface that decreases with distance. In the simulation, as shown in Figure S5, the outer boundaries and initial temperature are set to be 293.15 K. No-slip boundary conditions are employed at the boundaries between water and solids. The thermal parameters of silicon, gold, glass and water are all taken from COMSOL material library.

Figures and captions

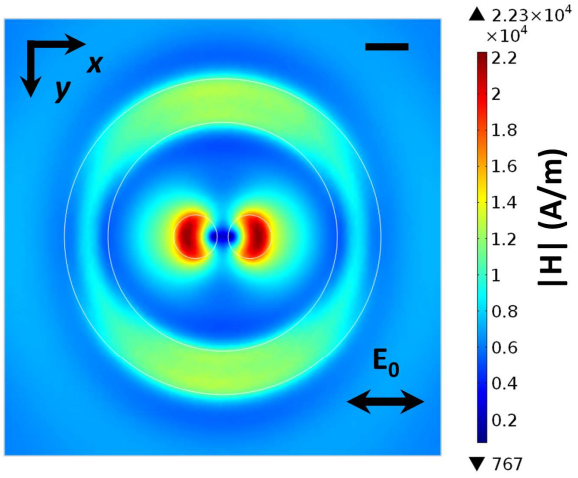

Figure S1 | Magnetic fields distribution. Plotted in the center plane of our Si nanoantenna with plane wave illumination (*x*-polarized, λ = 1064 nm, I_0 = 5 mW/μm^2). Scale bar: 200 nm.

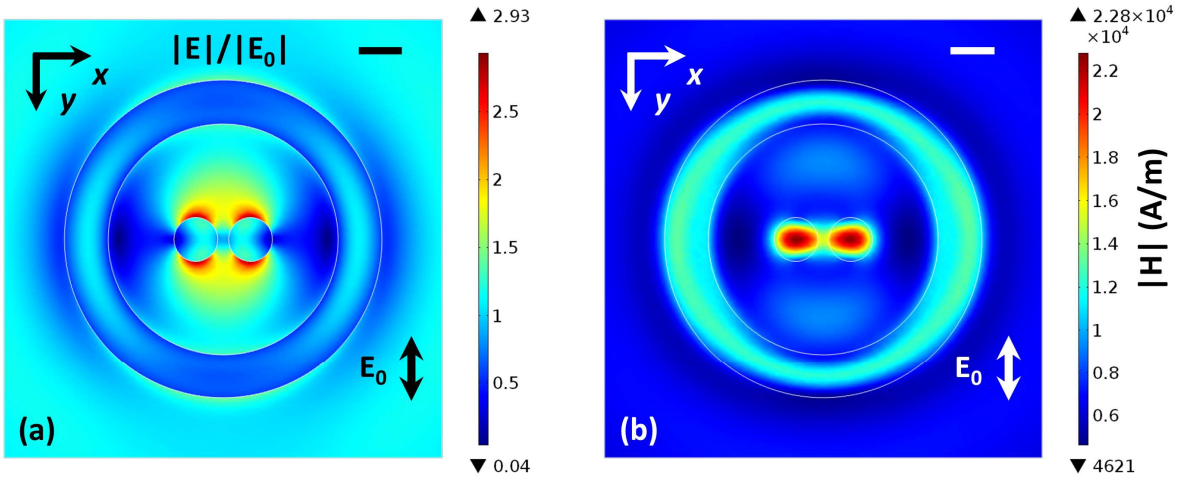

Figure S2 | Near fields for *y*-polarized illumination. (a) Electric field enhancement and (b) magnetic field amplitude in the center plane of our Si nanoantenna, for plane wave illumination (*y*-polarized, $\lambda = 1064$ nm, $I_0 = 5$ mW/μm^2). Scale bar: 200 nm.

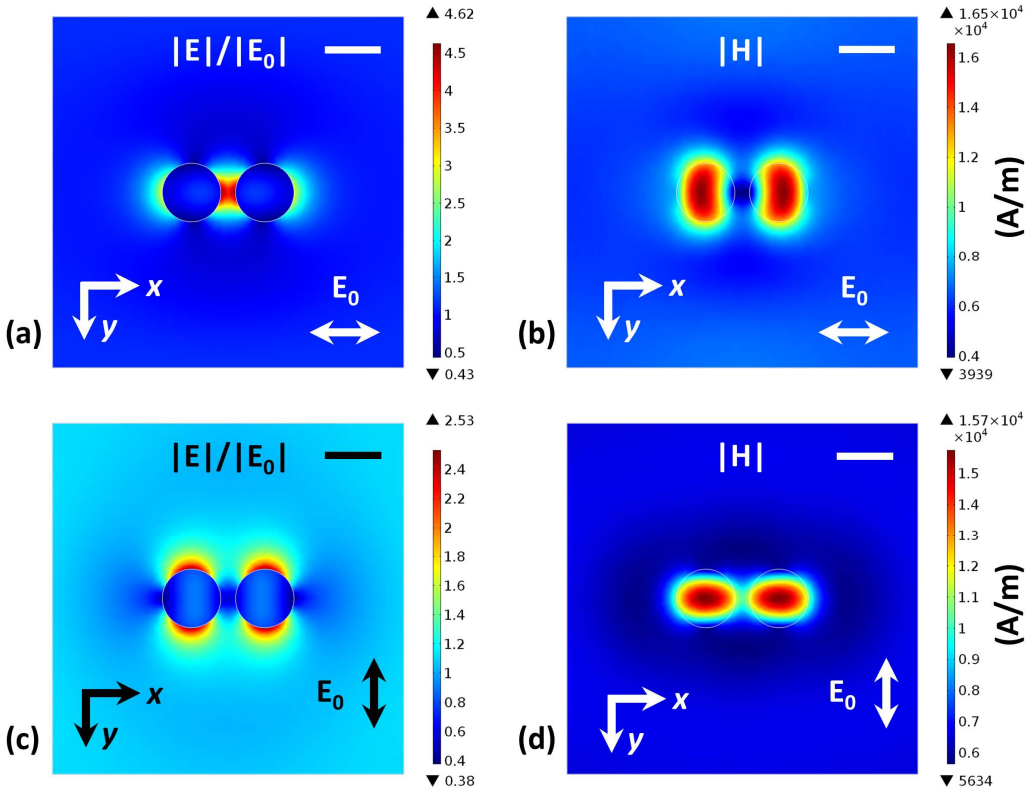

Figure S3 | Near fields in Si nanodimer. Si cylinder dimer nanoantenna (two cylinders of diameters and heights of 200 nm, 50 nm gap in between) on an Si substrate, covered with water. Plotted in the center plane ($z = -100$ nm cross section), illuminated by plane waves with different polarizations (λ = 1064 nm, I_0 = 5 mW/μm^2). (a)(b) *x*-polarized; (c)(d) *y*-polarized. Scale bar: 200 nm.

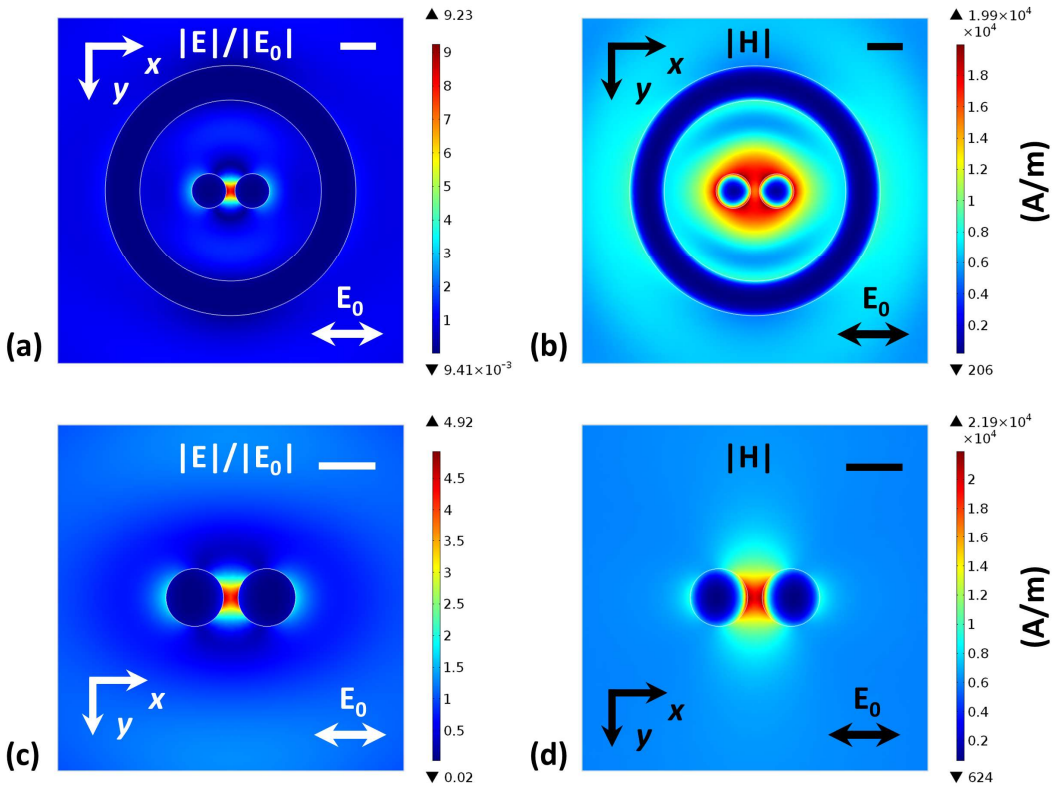

Figure S4 | Near fields in Au nanostructures. (a)(b) Au nanoantenna with same dimensions as Si nanoantenna on a glass substrate; (c)(d) Au nanodimer (two cylinders of diameters and heights of 200 nm, 50 nm gap in between) on a glass substrate, covered with water. (a)(c) Electric field enhancement, and (b)(d) magnetic field amplitude, plotted in the center plane and illuminated by plane wave with *x*-polarization (λ = 1064 nm, I_0 = 5 mW/μm^2). Scale bar: 200 nm.

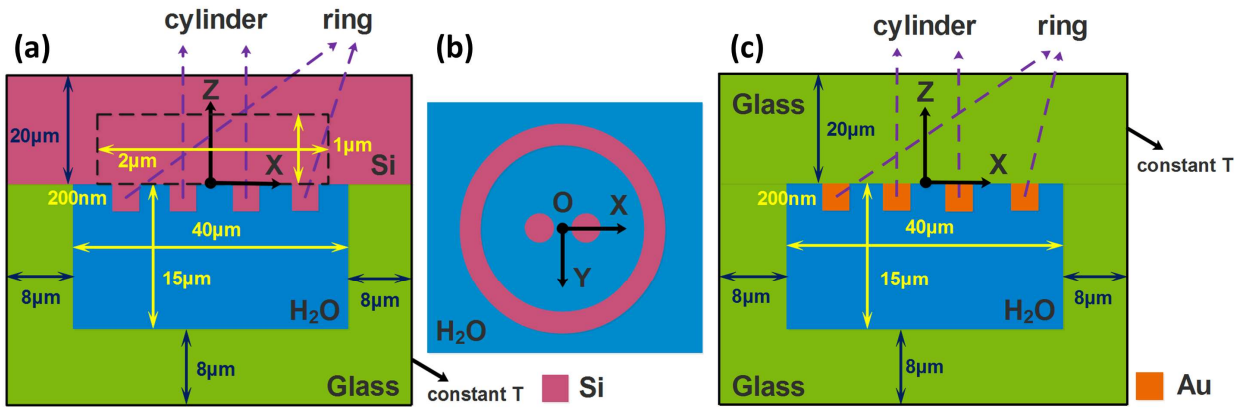

Figure S5 | Geometric configuration for heat calculation. Sketch is not to scale. (a)(b) Si nanoantenna on an Si substrate. (c) Au nanoantenna with same dimensions on a glass substrate. Black line indicates chamber boundaries at which T_0 = 293.15 K. Black dashed line in panel a indicates underlying Si substrate heat source. Si cylinders and Si ring also act as heat sources.

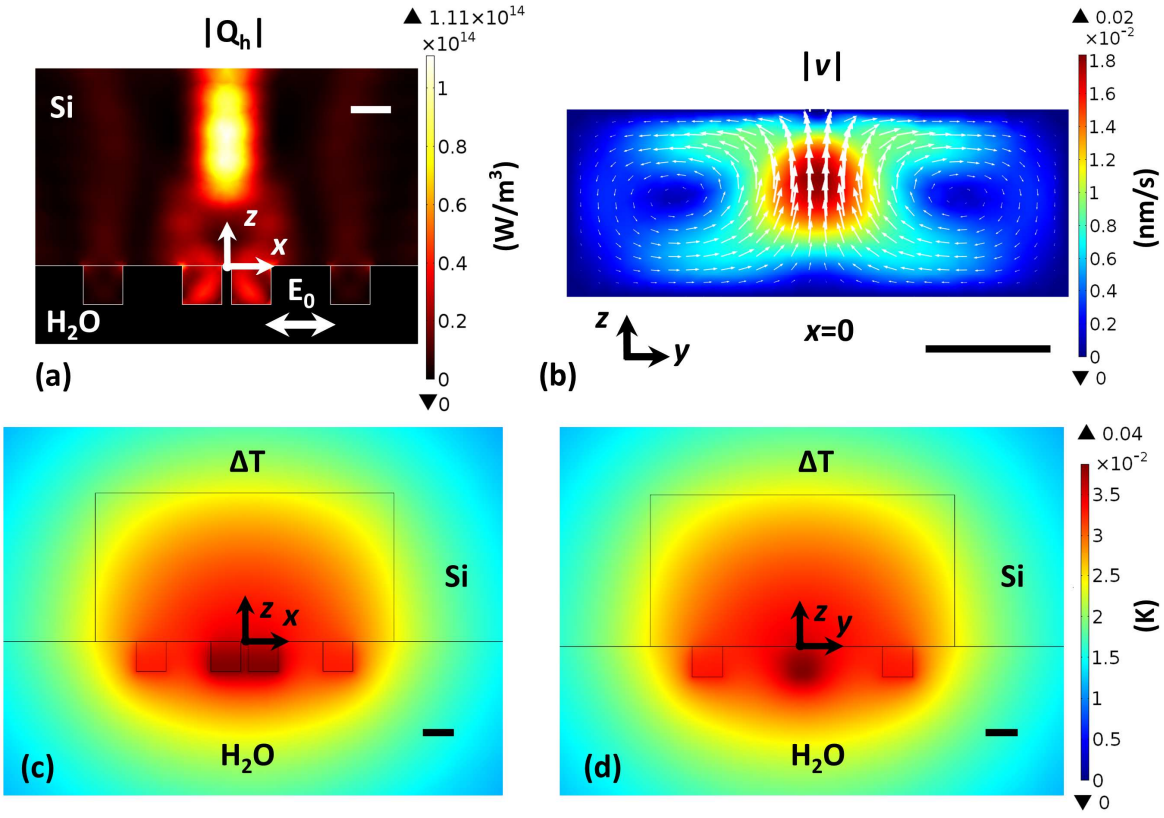

Figure S6 | Photothermal effects in Si nanoantenna. (a) Heat power dissipation density in the *xz*-plane. Scale bar: 200 nm. (b) Water convection velocity field in the *yz*-plane, plotted in both magnitude (color map: nm/s) and direction (white arrows, magnitude proportionally scaled). Chamber height is 15 μm. Scale bar: 10 μm. Steady state temperature increase profile in the (c) *xz*- and (d) *yz*-plane. Scale bar: 200 nm. White & black dots indicate coordinate system origin. I_0 = 5 mW/μm^2.

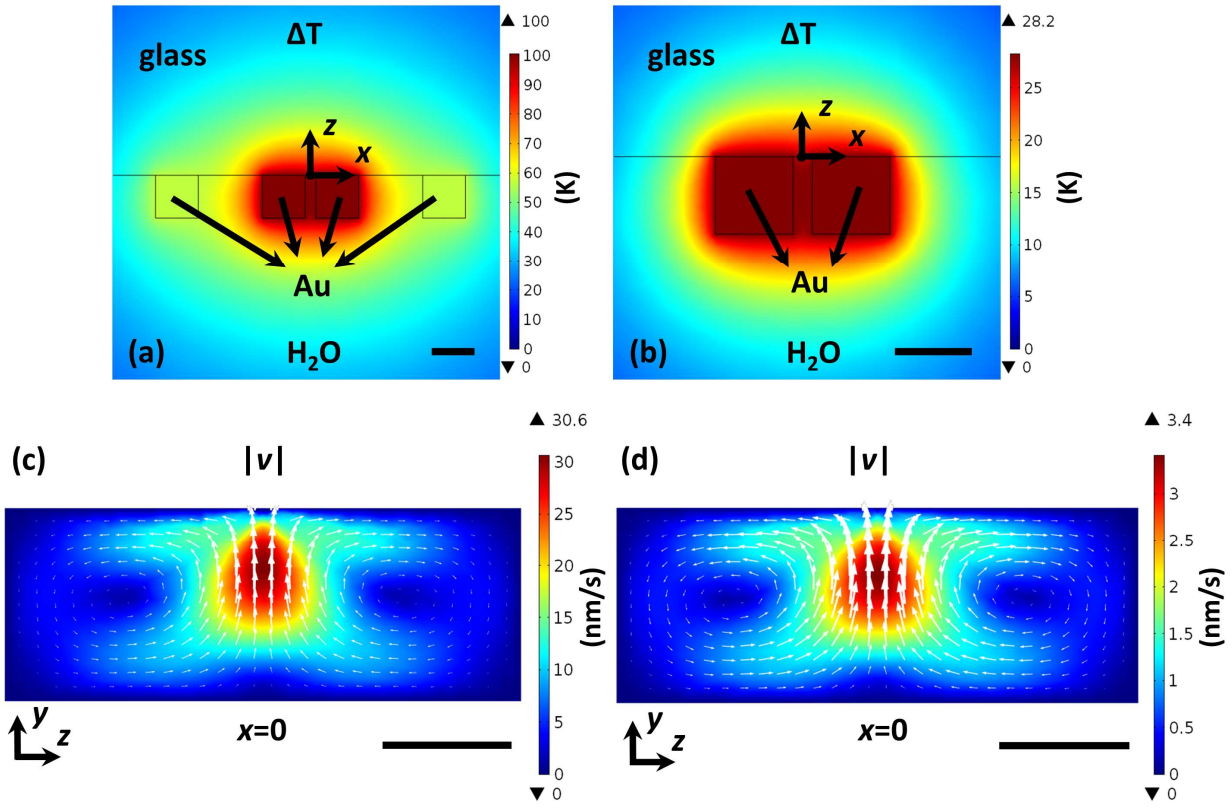

Figure S7 | Photothermal effects in Au nanostructures. (a)(c) Au nanoantenna with same dimensions as Si nanoantenna on a glass substrate; (b)(d) Au nanodimer (two cylinders of diameters and heights of 200 nm, 50 nm gap in between) on a glass substrate. (a)(b) Steady state temperature increase profile in the *xz*-plane. Black dot indicates coordinate system origin. Scale bar: 200 nm. (c)(d) Simulation of water convection velocity field in the *yz*-plane, plotted in both magnitude (color map: nm/s) and direction (white arrows, magnitude proportionally scaled). Chamber height is 15 μm. Scale bar: 10 μm. I_0 = 5 mW/μm^2.

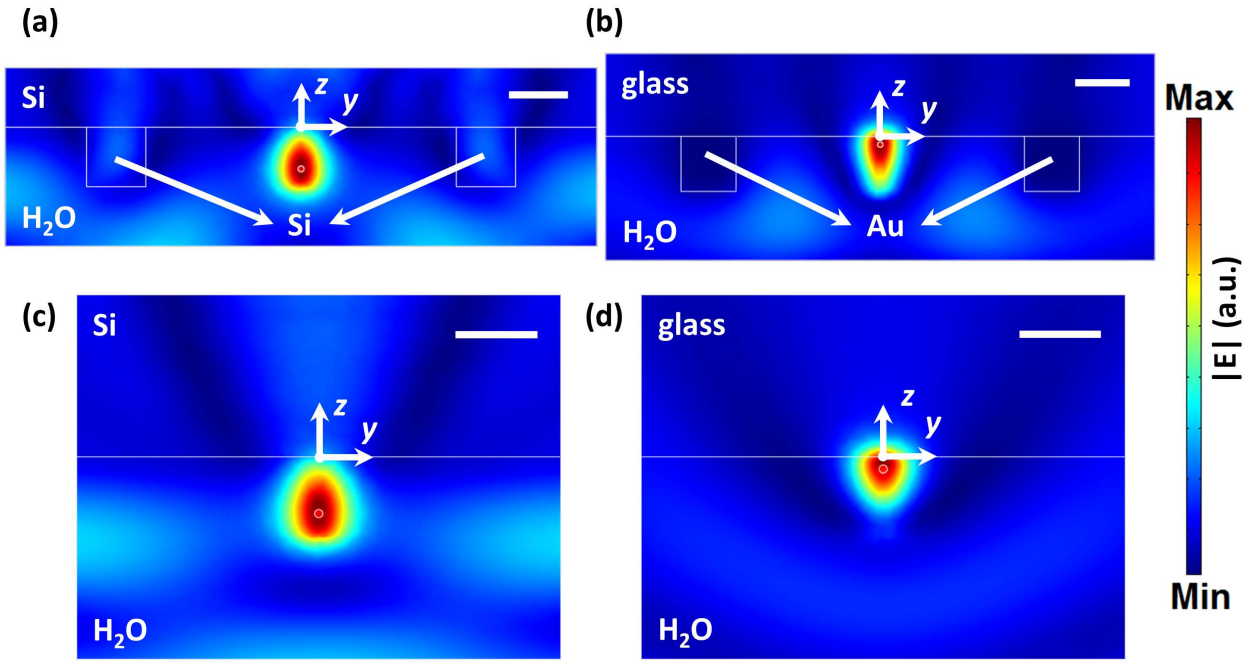

Figure S8 | Electric fields distributions, with a single NS included in simulation. Polystyrene NS: n_{NS} = 1.6, d = 20 nm. (a) Si nanoantenna on an Si substrate; (b) Au nanoantenna with same dimensions on a glass substrate; (c) Si cylinder dimer nanoantenna on an Si substrate; (d) Au cylinder dimer nanoantenna on a glass substrate. For each of these, water superstrate is used. Plane wave illumination from water side is employed (traveling in $+z$ direction, x-polarized, λ = 1064 nm). White dot indicates coordinate system origin. Center z-coordinates of NS are as follows ((x_{center}, y_{center}) = (0, 0)). (a)(c) z_{center} = −140 nm; (b)(d) z_{center} = −30 nm. I_0 = 9.5 mW/μm^2. Scale bar: 200 nm.

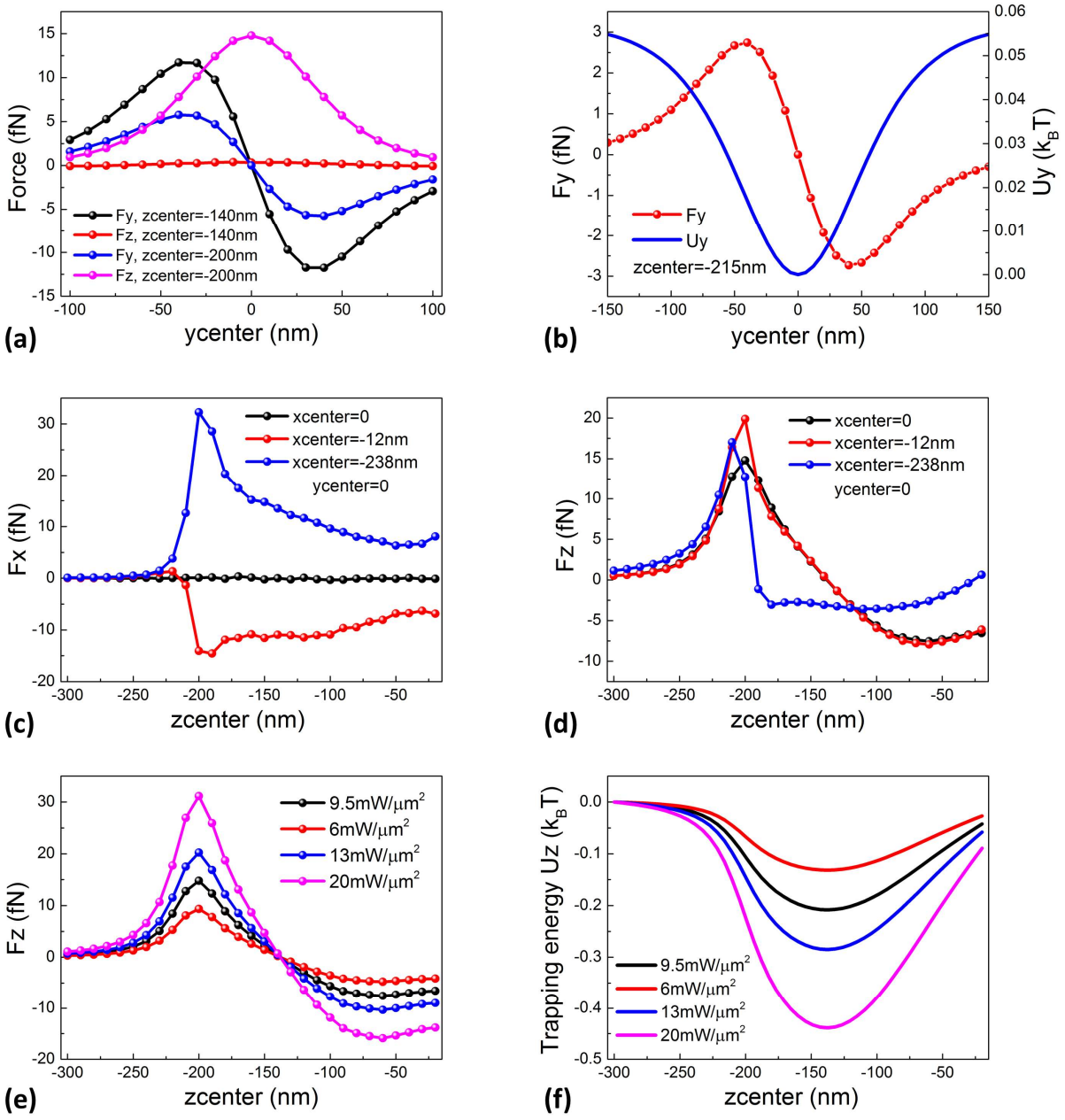

Figure S9 | MST optical forces in Si nanoantenna. Polystyrene NS: n_{NS} = 1.6, d = 20 nm. (a) F_y and F_z along y-direction (x_{center} = 0) for moving in the middle (z_{center} = −140 nm) and the edge (z_{center} = −200 nm). (b) F_y and U_y vs. NS position at 15 nm outside of nanoantenna along y-axis (x_{center} = 0, z_{center} = −215 nm). (c)(d) NS moving in the xz-plane (y_{center} = 0) along z-direction in the middle (x_{center} = 0) and around left cylinder (x_{center} = −12 nm and −238 nm, that is, 3 nm distance to Si surface) of (c) F_x and (d) F_z. (a)–(d) I_0 = 9.5 mW/μm^2. (e) Vertical force F_z and (f) trapping potential energy U_z along z-axis as functions of trapping laser intensity and position over the gap (x_{center} = y_{center} = 0). In panels b and f, $1k_BT = 4.05\times10^{-21}$ J.

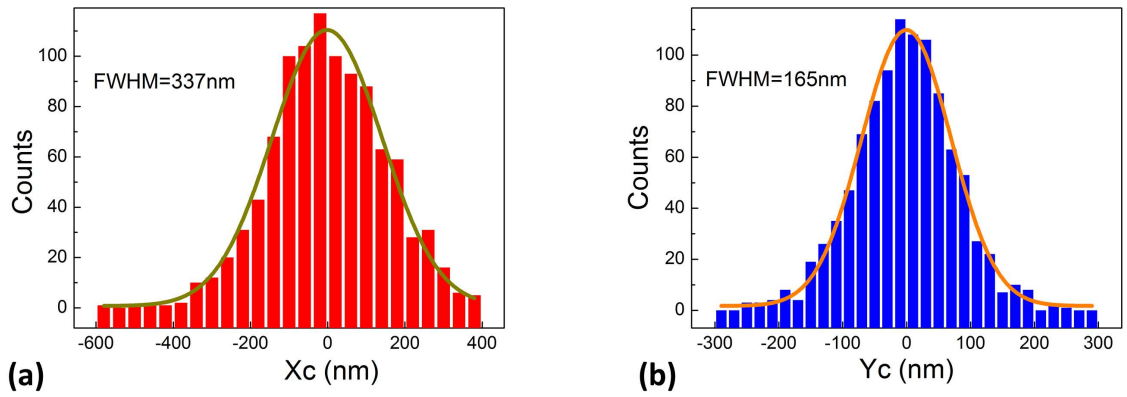

Figure S10 | Brownian motion histogram. Position histograms (1000 EM-CCD frames) of a trapped 20 nm NS, relative to trap center along *x*- and *y*-axes. Illumination intensity is I_0 = 9.5 mW/μm^2. These plots are extracted from data of Figure 4e.

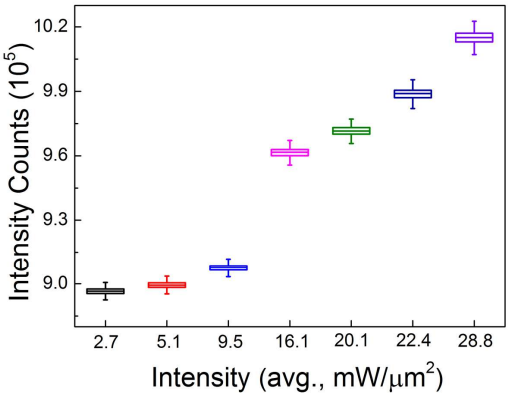

Figure S11 | Fluorescence measurement. Recorded EM-CCD intensity counts vs. trapping laser intensity (single 20 nm NSs, same green laser power, 30×30 pixel cross section, 1000 frames). Box plot measured for single trapped NSs. Background has not been subtracted from data in this plot. For each box, the center is the median, the edges of the box are the 25th and 75th percentiles, and the whiskers are the 5th and 95th percentiles.

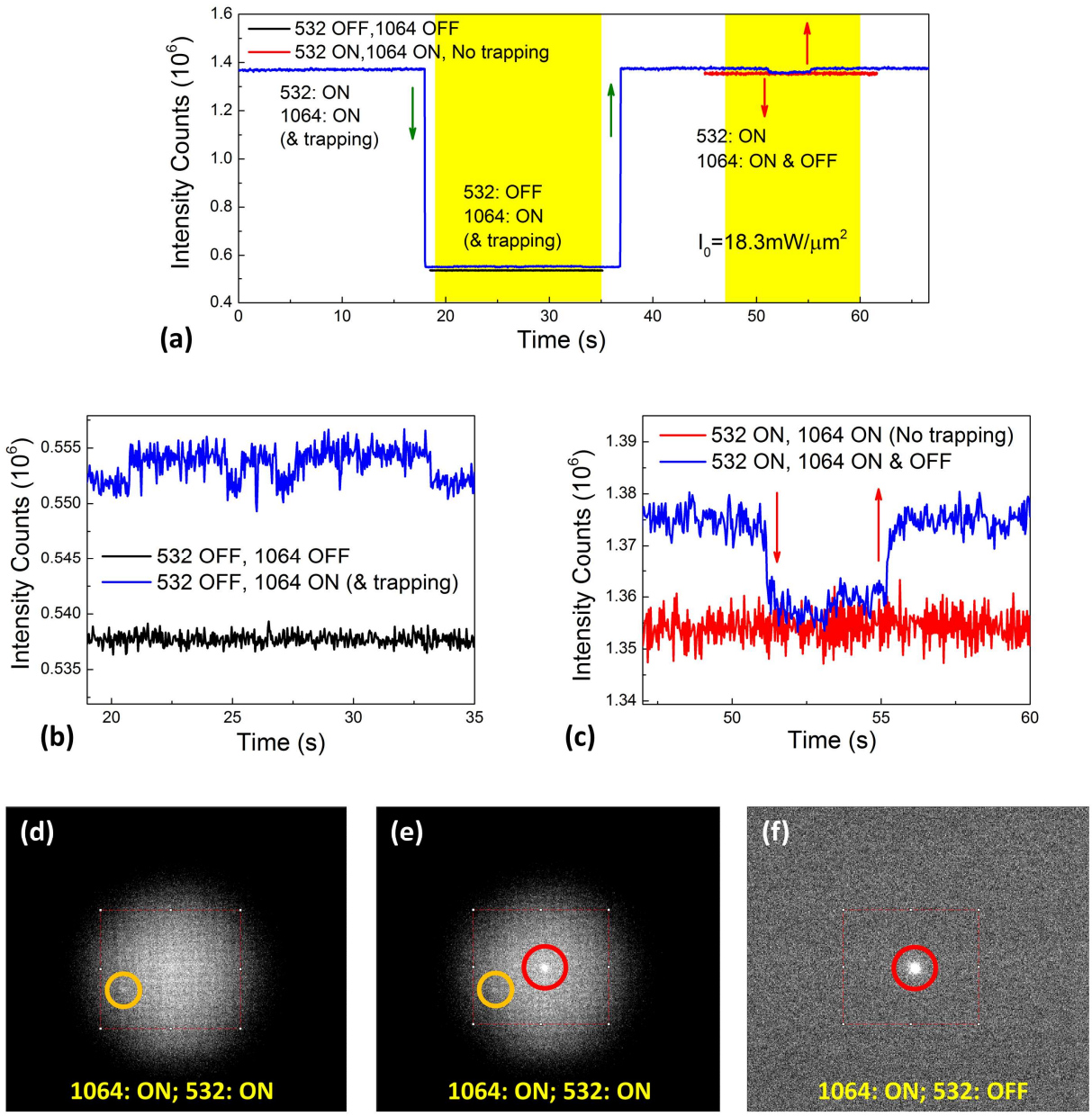

Figure S12 | Two-photon excitation. (a) Experimental fluorescence time trace indicating optical trapping, release and two-photon excitation of a single 20 nm NS (30×30 pixel cross section, I_0 = 18.3 mW/μm^2). Black and red curves, obtained in separate measurements, are included on this plot for comparison of signal levels (intensity counts). Zoom-in of panel a from (b) 19−35 s and (c) 47−60 s. (d)−(f) EM-CCD images of fluorescence. Orange circles indicate the NS that is attached to the Si surface, and the red circles indicate the NS being trapped. Switching the trapping laser off releases NS from the nanoantenna. After switching the green laser off, one observes the two-photon absorption induced fluorescence from trapped NS, but no one-photon induced fluorescence from the NS attached to the surface. Images are captured with auto-scale contrast of EM-CCD camera.

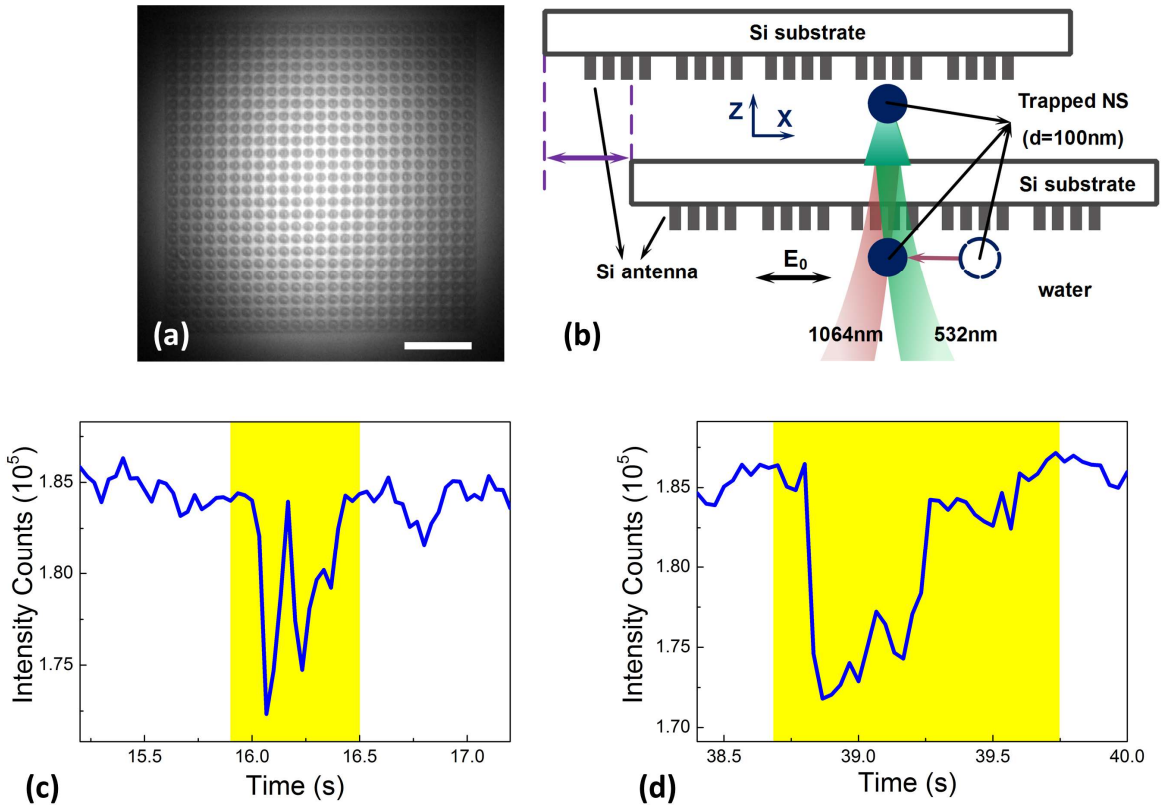

Figure S13 | Optical transport of NSs. (a) Microscope image of Si nanoantenna array chip immersed in water. Scale bar: 10 μm. (b) Schematic of trapping and transport of single NSs (d = 100 nm) across an array of Si nanoantennas. (c)(d) Zoom-in of Figure 5d showing NS release, Brownian diffusion and transport from one illuminated nanoantenna to another.

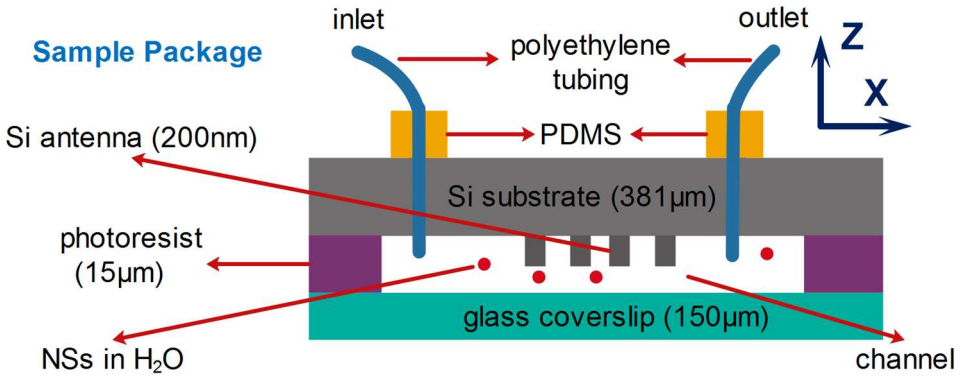

Figure S14 | Microfluidic chamber. Cross section of closed perfusion chamber, sealed with UV-cured optical adhesives.

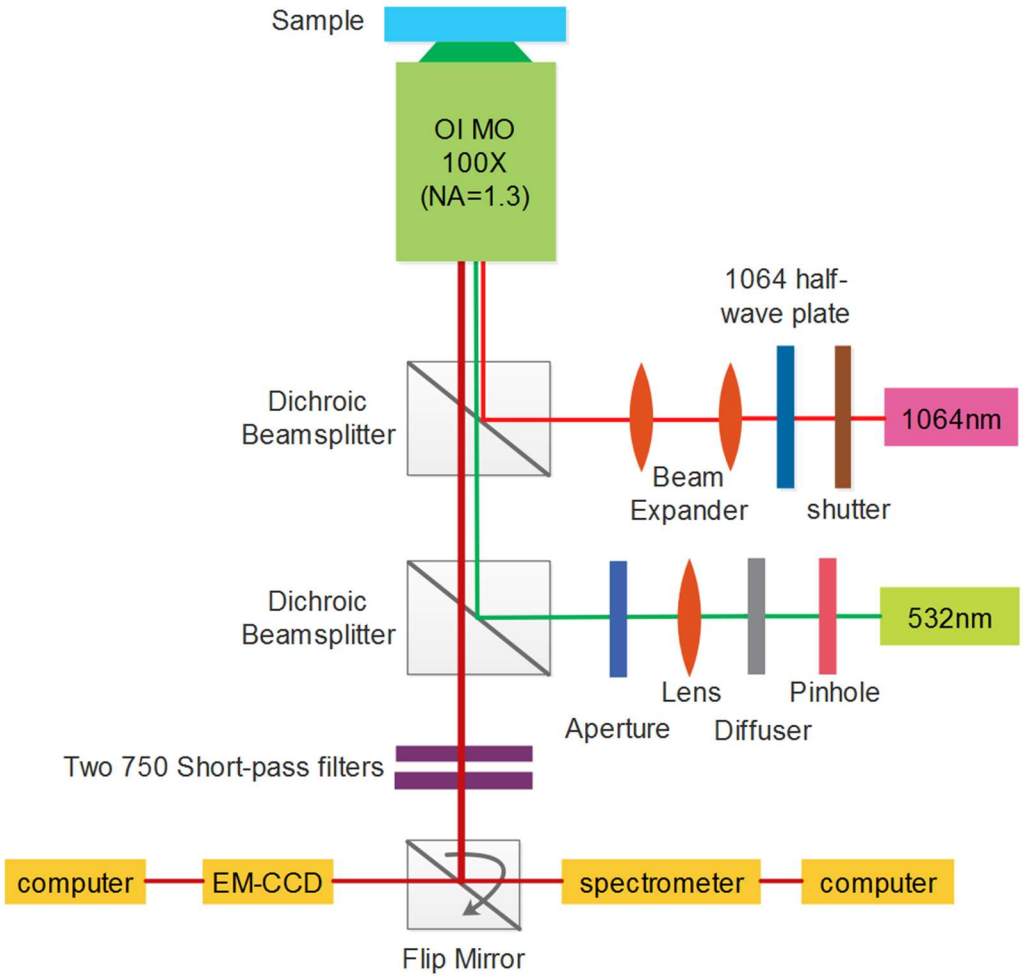

Figure S15 | Schematic diagram of experimental setup. The trapping is monitored by observing the NSs fluorescence. (OI MO = Oil Immersion Microscope Objective)

Movies

Movie 1. Optical trapping and release of a single 20 nm polystyrene nanosphere.

Movie 2. Optical trapping and release of two 20 nm polystyrene nanospheres.

Movie 3. Optical trapping and release of a single 100 nm polystyrene nanosphere.

Movie 4. Optical trapping and release of two 100 nm polystyrene nanospheres.

Movie 5. Optical trapping and release of three 100 nm polystyrene nanospheres.

Movie 6. Optical trapping and transport of a single 100 nm polystyrene nanosphere.

Movie 7. Optical trapping and transport of two 100 nm polystyrene nanospheres.

References

(1) Palik, E. D. *Handbook of Optical Constants of Solids*; Academic Press: New York, 2007.

(2) Johnson, P. B.; Christy, R. W. Optical constants of the noble metals. *Phys. Rev. B* **1972**, 6, 4370-4379.

CHAPTER 5

All-dielectric nanotweezers for trapping and observation of a single quantum dot

This chapter is originally published in Optics Express:

Zhe Xu and Kenneth B. Crozier. All-dielectric nanotweezers for trapping and observation of a single quantum dot. ***Optics Express*** **2019**, 27, 4034–4045.

Research Article | Vol. 27, No. 4 | 18 Feb 2019 | OPTICS EXPRESS 4034
Optics EXPRESS

All-dielectric nanotweezers for trapping and observation of a single quantum dot

ZHE XU[1] AND KENNETH B. CROZIER[1,2,*]

[1]School of Physics, University of Melbourne, Victoria 3010, Australia
[2]Department of Electrical and Electronic Engineering, University of Melbourne, Victoria 3010, Australia
*kcrozier@unimelb.edu.au

Abstract: We report the optical trapping of a single streptavidin-coated CdSe/ZnS quantum dot whose overall diameter is around 15–20 nm, in a microfluidic chamber by an all-dielectric (silicon) nanotweezer with negligible local heating. The use of fluorescence microscopy allows us to readily observe trapping events, tracking the fluorescence emission from, and the position of, each individual trapped quantum dot as a function of time. The blinking behavior of the quantum dots is observed during the trapping process, that is, in the near field region of the silicon nanoantenna. We furthermore show that the continuous wave infrared laser employed to trap the quantum dots can also excite photoluminescence from them via two-photon absorption. We present Maxwell stress tensor simulations of optical forces applied to a single quantum dot in the nanoantenna's vicinity. This work demonstrates that all-dielectric nanotweezers are a promising means to handle quantum dots in solution, enabling them to be localized for observations over extended periods of time.

1. Introduction

Plasmon-based nano-optical tweezers [1–8] have been shown to offer advantages over conventional optical tweezers [9–11] for the trapping of nanometer-sized objects via the enhanced optical forces that occur when light is confined on a deeply subwavelength scale. The ability to optically trap and manipulate nanomaterials presents many opportunities for nanoscience [12,13]. However, the high level of Joule heating from dissipative losses is recognized as a big challenge faced by plasmonic tweezers [14,15], especially for the trapping and sensing of biological specimens [16]. Loss is also a major issue for many other applications of plasmonics (and not just nanotweezers). This has motivated recent advances in an alternative approach for nano-optics that uses subwavelength high refractive index dielectric nanoelements. These devices are termed all-dielectric nanoantennas [17–23], and generate strong near-field hotspots with much lower absorption losses than plasmonics. In this work, we demonstrate that all-dielectric nanoantennas allow single quantum dots to be trapped optically in a robust fashion.

Colloidal quantum dots (QDs) are nanoscale semiconductor crystals [24] with applications ranging from consumer products such as displays to use as fluorescent markers in biological labeling [25]. They have excellent fluorescence properties [26] that include size-dependent emission, high quantum yield, large linear and nonlinear absorption cross-sections and excellent photostability. At present, there has been much interest in using optical tweezers to trap nanomaterials in solution for a variety of reasons, including to localize these materials to facilitate their characterization via spectroscopy [12,13]. It has been demonstrated that conventional single light-based optical tweezers can be utilized to trap individual QDs and aggregates of QDs [27–33]. This prompts the question of whether QDs can be trapped using nanotweezers supported by surface plasmons and other methods, due to the potential advantages that include tighter spatial confinement, lower optical power requirements and integration with sensing. The trapping of QDs using silicon nitride photonic crystal resonators

#355248 https://doi.org/10.1364/OE.27.004034
Journal © 2019 Received 17 Dec 2018; accepted 20 Dec 2018; published 4 Feb 2019

Optics EXPRESS

has been investigated [34], but this approach is not trivial from an experimental standpoint, requiring tunable laser sources and coupling to waveguides. It has been shown that plasmonic nanotweezers can trap individual QDs and silica-coated QDs [35–37], but it is well-established that the optical properties of QDs can be considerably altered when they are in the vicinity of plasmonic nanostructures [38,39]. This motivates us to demonstrate QDs trapping with a non-plasmonic platform.

In this work, we present direct experiments of optical trapping of a single streptavidin-coated quantum dot by an all-dielectric nanotweezer, that is, silicon (Si) nanoantenna with a Si substrate, via illumination with an infrared wavelength 1064 nm continuous wave (CW) trapping beam. The QD has a CdSe core and ZnS shell, and is further coated by a polymer shell and then streptavidin. According to the manufacturer, the QD has an overall diameter of ~ 15–20 nm. Our simulations indicate that the temperature rise of the nanoantenna due to the trapping laser illumination is negligible and we thus expect no thermal quenching of the QD emission. Employing fluorescence microscopy, we monitor the optical trapping and release of the QD when the trapping laser beam is turned on and off. We furthermore track the trapped QDs versus time, monitoring the fluorescent intensity and centroid position. We observe the fluorescence blinking of single QDs trapped by our silicon nanoantenna. We demonstrate that the illumination from the infrared laser not only results in the optical trapping of a QD, but also excite fluorescence from it via two-photon absorption (TPA). Finally, we quantify the optical trapping forces exerted on the QD using numerical simulations via the Maxwell stress tensor method. This paper illustrates that all-dielectric nanotweezers allow QDs to be trapped optically, without the challenges that can be associated with plasmonic approaches that include local heating and modification to the optical properties of the QDs.

2. Design and simulation

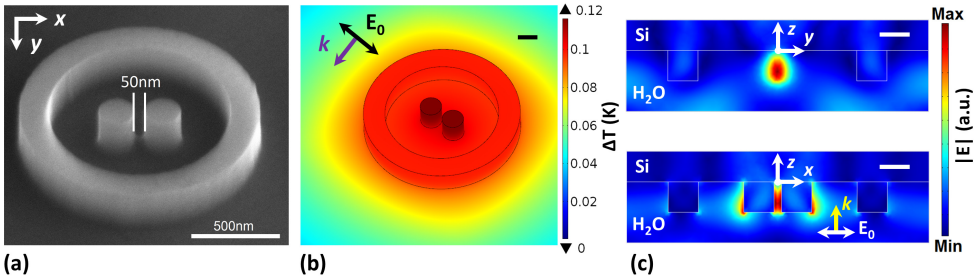

Fig. 1. (a) Scanning electron micrograph (SEM) picture (45° tilt) of a Si nanoantenna situated on a Si substrate. (b) Temperature rise profile (for steady state) around a Si nanoantenna, I_0 = 15 mW/μm^2. Scale bar: 200 nm. (c) Electric fields profile in the *yz*- and *xz*-cross section, for 1064 nm plane wave (*x*-polarization) at normal incidence. White dots represent the origin of coordinate system. Scale bar: 200 nm.

Our all-Si nanoantenna consists of two identical Si nanocylinders separated by a narrow gap (50 nm) and surrounded by a Si ring [Fig. 1(a)]. The two cylinders have diameters and heights of 200 nm. The ring has inner and outer radii of 525 nm and 725 nm, respectively (i.e., is 200 nm wide). The ring has a height of 200 nm. We fabricate the Si nanoantennas via electron beam lithography (EBL) and reactive ion etching methods [23]. We perform finite element method simulations (FEM; COMSOL Multiphysics) of our Si nanoantenna to understand its trapping behavior [23]. In these simulations, the nanoantenna is covered by water (n_{water} = 1.33) and illuminated at normal incidence by a plane wave (wavelength 1064 nm) with *x*-polarization from water side (travelling in +*z* axis). In Fig. 1(b), we plot the steady state temperature rise of the Si nanoantenna for an illumination trapping laser intensity of I_0 = 15 mW/μm^2, which is typical of the levels we employ in our QDs trapping experiments. It can be noticed that the temperature increase is below 0.12 K. This represents a small value, which originates from the fact that Si has a low imaginary permittivity component [40] and a high

thermal conductivity [6]. We thus do not expect to see the quenching or bleaching of the QD emission that can occur with large increases in temperature [19,21]. We next plot the simulated electric field distributions on two cross sections through the nanoantenna as Fig. 1(c). It can be seen that there is a hotspot in the gap between two cylinders, which we attribute to be associated with the coupling between the dipole modes of two Si cylinders [18]. We expect QDs to be trapped here, via the gradient forces accompanying these confined local fields [41,42]. It can be seen that there are also hotspots at the outer extremities of cylinders, but with the smaller electric field enhancement than the hotspot in the gap region between the cylinders.

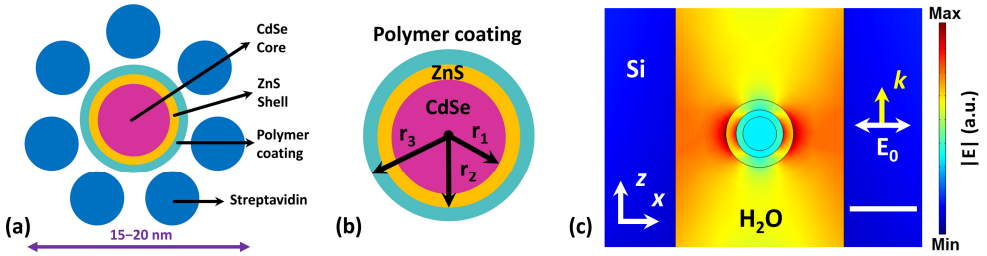

Fig. 2. (a) Schematic illustration of a streptavidin-coated QD structure. (b) Model of QDs used in near fields and optical forces simulations. (c) Electric fields distribution (y = 0 cross section) in the Si nanoantenna gap with a QD included (x_{center}, y_{center}, z_{center}) = (0, 0, −140 nm). Scale bar: 20 nm.

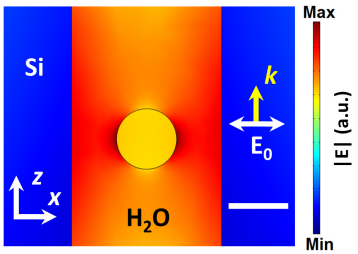

Fig. 3. Electric fields distribution (y = 0 cross section) in the Si nanoantenna gap with a 20 nm polystyrene NS included (x_{center}, y_{center}, z_{center}) = (0, 0, −140 nm). Scale bar: 20 nm.

Figure 2(a) schematically illustrates the structure of the QDs we use in experiments, based on information from the manufacturer (Life Technologies, Q10121MP, Qdot 655 Streptavidin Conjugate) [43]. The QD has a CdSe core and ZnS shell, and is further coated by a polymer layer and streptavidin, with typically 5–10 streptavidin molecules for each QD according to the manufacturer. The QD is ~ 15–20 nm in total diameter. We choose to trap these QDs because they represent a typical choice for biological experiments in which QDs are employed as labels [31,32]. As the QD structure is complex and not known precisely by us, approximations are made when modeling it. Specifically, as depicted in Fig. 2(b), the QD is modeled as consisting of a spherical core (CdSe) with two spherical shells (ZnS and polymer), that is, without streptavidin molecules. The radii of the core and two shells are taken as r_1 = 5 nm, r_2 = 7 nm, and r_3 = 10 nm. We take the refractive index of the outer shell to be 1.6, as this is a typical value for polymers. In Fig. 2(c), we depict the electric field profile on the xz-plane (y = 0 cross section) in which the QD is in the gap, centered at (x_{center} = y_{center} = 0, z_{center} = −140 nm). For comparison purposes, we provide the calculation for the situation of a single polystyrene nanosphere (NS) with a 20 nm diameter at the same position in Fig. 3. It can be seen that the presence of the QD modifies the fields distribution in the nanoantenna gap more strongly than the NS does. This is because the QD has a larger

Optics EXPRESS

refractive index (n_{CdSe} = 2.54, n_{ZnS} = 2.29) than the NS (n_{NS} = 1.6). As we discuss next, the associated optical forces are also enhanced.

The enhanced and spatially confined field distributions provided by the nanoantenna permit the efficient trapping of single nanoparticles. The general way of computing the optical forces applied to a small object is the Maxwell stress tensor (MST) method [41,42]. Here we determine the electric and magnetic fields distributions via FEM simulations and use the MST method to predict the optical forces [8,23] exerted on a single QD with the multi-layer structure (r_1 = 5 nm, r_2 = 7 nm, and r_3 = 10 nm). Optical forces are calculated on the polymer surface enclosing the QD. The results are displayed as Fig. 4. In Fig. 4(a), we show the force component F_z on the nanoparticle versus its center location along the z-axis. In addition to the QD, we also model a polystyrene NS (with a diameter of 20 nm) and a smaller QD (with r_1 = 3 nm, r_2 = 4 nm, and r_3 = 5 nm). It can be seen that these display similar characteristics, but with the optical force being largest for the QD, followed by the 20 nm NS and the smaller QD. In all cases, the force magnitude is maximum at the nanoantenna edge. It can be seen that when the particle is away from the nanoantenna (z_{center} < –200 nm), F_z is positive, meaning that it is pulled toward the nanoantenna. This continues when the particle enters the nanoantenna region (–200 nm < z_{center} < –140 nm) until the particle reaches roughly the nanoantenna midpoint, beyond which (i.e., z_{center} > –140 nm) F_z is negative. This location (z_{center} = –140 nm) thus represents an equilibrium position, that is, the particle will experience a restoring force if it displaced along the z-axis from this point, for example, by Brownian forces from water molecules. We then plot the horizontal components of optical forces applied to a single QD versus its center location along the x- [Fig. 4(b)] and y-axes [Fig. 4(c)]. It can be seen from Fig. 4(b) that F_x > 0 for x_{center} > 0, and F_x < 0 for x_{center} < 0. The QD is therefore predicted to have a tendency to be drawn to the sides of the gap. It can be seen that F_z is positive for the range of x-axis positions considered, meaning that the QD is drawn to the nanoantenna. This is also the case for the range of y-axis positions considered in Fig. 4(c). It also can be seen from Fig. 4(c) that the QD feels a restoring force for small displacements along the y-axis about (x_{center}, y_{center}, z_{center}) = (0, 0, –140 nm) and (0, 0, –200 nm). In other words, F_y is negative for y_{center} > 0, and positive for y_{center} < 0.

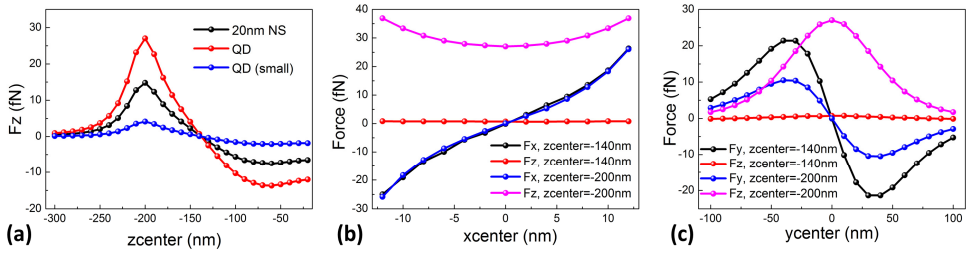

Fig. 4. MST optical forces exerted on a single QD (r_1 = 5 nm, r_2 = 7 nm, r_3 = 10 nm) for I_0 = 9.5 mW/μm^2. (a) F_z vs. vertical position (x_{center} = y_{center} = 0). NS: d = 20 nm, n_{NS} = 1.6; Small QD: r_1 = 3 nm, r_2 = 4 nm, r_3 = 5 nm. (b) F_x and F_z vs. QD position along x-axis at different vertical (z-axis) positions, all with y_{center} = 0. (c) F_y and F_z vs. QD position along y-axis at different vertical (z-axis) positions, all with x_{center} = 0.

3. Experimental methods

We next describe our experimental methods and results. The QDs (Life Technologies, Q10121MP) are homogeneously suspended in 1X PBS (phosphate-buffered saline, pH 7.4) solution. Tween 20 (0.05% v/v) has been added as surfactant to avoid aggregation. The concentration of QDs in the experiments is ~ 10^{-8} mol/L. Soon after being made, the suspension is ultrasonicated using a bath sonicator, filtered to remove aggregates, etc. and injected into a microfluidic chamber that is ~ 15 μm thick. The microfluidic chamber consists of the Si chip containing nanoantennas sealed to a glass coverslip on which a patterned

Optics EXPRESS

photoresist layer (~ 15 μm thick) has been formed [23]. Our setup includes an inverted optical microscope (Nikon TE2000), an oil immersion objective (Nikon, 100×, NA = 1.3), a green laser (wavelength 532 nm, for emission excitation), an *x*-polarized CW infrared laser (for optical trapping, spot diameter ~ 1.2 μm, wavelength 1064 nm), a set of filters, a sensitive electron multiplying camera (EM-CCD, frame rate of 30 fps, exposure time of ~ 30 ms) and a grating spectrometer [23]. This system allows us to observe an individual QD and to track its position as it interacts with the Si nanoantenna. Using this system, we readily observe the optical trapping of a single QD by our Si nanoantenna. Two example experiments are presented as Figs. 5 and 6. These are discussed in the paragraphs below. Illumination intensities of I_0 = 17.3 mW/μm^2 and I_0 = 16.1 mW/μm^2 are used for Figs. 5 and 6, respectively. Additional trapping experimental data are provided in Appendix (see Fig. 7). Our experiments confirm that the QDs are optically trapped when the trapping beam is switched on and that they are released from the Si nanoantenna when it is switched off. As shown in Appendix (see Fig. 8), QDs sometimes become stuck to the Si surface. These QDs are readily identified as they are not released from the antenna surface when the trapping beam is turned off. The permanently-adsorbed QDs also appear brighter in the fluorescence microscope images than the optically trapped QDs, making them easy to distinguish.

4. Results and analysis

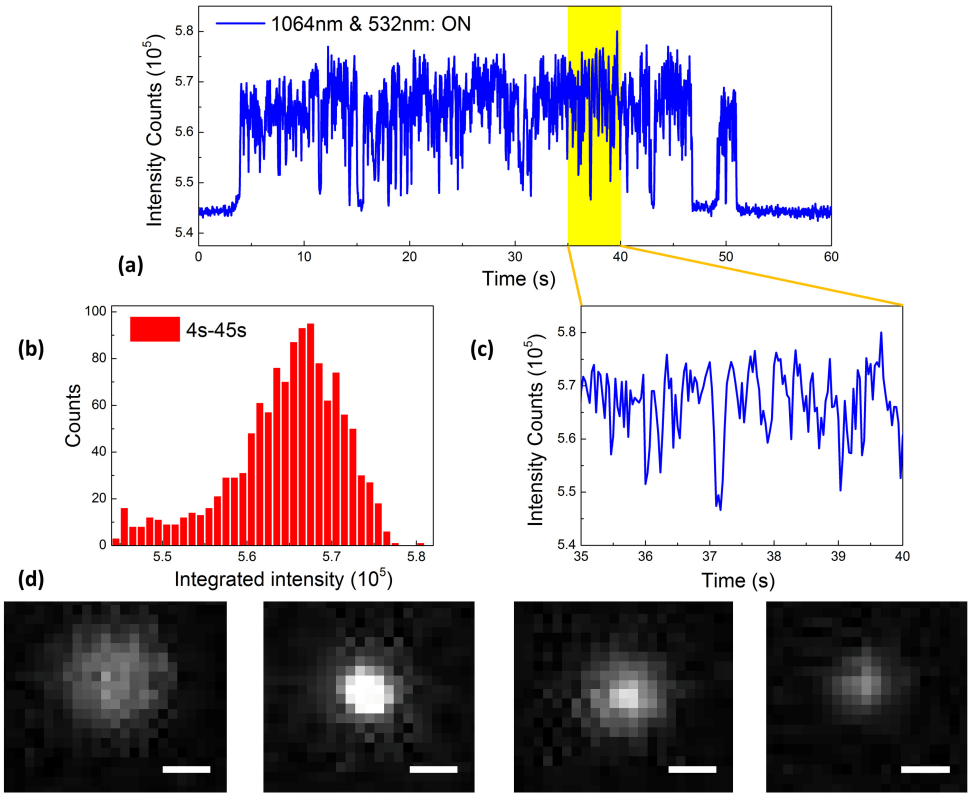

Fig. 5. (a) Fluorescent emission versus time for the trapping of a single QD (see also Visualization 1). (b) Corresponding emission counts histogram of optically trapped QD (from 4–45 s), collected from data of panel (a). (c) Zoom-in of (a) from 35–40 s showing the QD blinking. (d) Four selected EM-CCD images illustrating fluorescence blinking from single trapped QD. Scale bar: 800 nm. (Trapping laser intensity I_0 = 17.3 mW/μm^2)

Optics EXPRESS

Figure 5 represents one of the key findings of this paper, showing the direct observation of the trapping of a single QD via optical forces in PBS solution using an all-Si nanotweezer/nanoantenna (see Visualization 1). In Fig. 5(a), we depict the fluorescent intensity counts as a function of time, obtained by integrating over a cross section covering 30×30 pixels of each EM-CCD frame that is centered over the Si nanoantenna. It can be seen that there are large fluctuations in the fluorescence signal from the single QD trapped in Fig. 5(a). We attribute this to blinking of the QD [31,33], and note that this was not observed in previous works on the optical trapping of single fluorescent nanoparticles (i.e., polystyrene NSs) [8,23]. We do not observe any quenching or photobleaching of the QD emission [32,37]. This is reasonable because the Si nanoantennas produce ultra-low heat generation [19,23], so quenching or photobleaching associated with the temperature rise should be negligible. It can also be observed that QD fluorescence blinking occurs during the time interval over which the QD is optically trapped (i.e., ~ 4–47 s and ~ 49–51 s). Figure 5(b) plots an emission count histogram of the fluorescence blinking data (4–45 s) in Fig. 5(a). Further insight into the blinking phenomenon can be obtained from Fig. 5(c), which represents a zoom-in of the period of 35–40 s [from Fig. 5(a)]. It can be seen that the QD is cycling between emitting "on" and non-emitting "off" states. Four selected EM-CCD frames showing the single trapped QD is given as Fig. 5(d) to further illustrate the blinking process. For comparison, in Appendix (see Fig. 9), we plot fluorescent emission from a single freely-moving QD as a function of time, which again illustrates the blinking process. This is obtained by analyzing EM-CCD images gathered over five seconds of the moving QD and integrating intensity from each frame over a cross section (35×35 pixels), that is slightly larger than before to ensure that the (moving) QD is included. The blinking process is important to understand in applications of QDs. Here, we show that our Si nanoantenna enables us to trap QDs and monitor their blinking. This is might useful for future investigations of blinking from single QDs.

We next discuss our results on exciting fluorescence from individual QDs via two-photon absorption. Key results are shown as Fig. 6. Insight into the process can be obtained by examining EM-CCD images collected with both infrared and green lasers on [Fig. 6(a)-*i*], with only the infrared laser on [Fig. 6(a)-*ii*] and with only the green laser on [Fig. 6(a)-*iii*]. We note that the infrared 1064 nm trapping beam is focused by the objective to a small spot (~ 1.2 μm diameter) while the green laser illuminates a broad area that is comparable to the field-of-view of Fig. 6(a). When both the green and trapping lasers are switched on [Fig. 6(a)-*i*], therefore, fluorescence can be seen both from an optically trapped QD around the nanoantenna gap (red circle) as well as a stuck QD to another part of the Si surface (yellow circle). When only the infrared laser is on, fluorescence is only observed from the optically trapped QD [Fig. 6(a)-*ii*], which we conclude to originate from TPA [32,36,44]. Similarly, when only the green laser is on, fluorescence is only observed from the stuck QD, as there is no longer a QD optically trapped around the nanoantenna gap [Fig. 6(a)-*iii*]. In Fig. 6(b), fluorescence emission of the optically trapped QD versus time is plotted, again obtained by integrating over a cross section covering 30×30 pixels from each EM-CCD frame. Both infrared and green lasers are on for $0 < t < 35$ s, while only the infrared laser is on for $t > 35$ s. It can be seen that the QD blinking behavior occurs over the duration of the experiment. Emission spectra measured from the single optically-trapped QD when illumination is supplied by both lasers and by only the infrared laser are shown as Fig. 6(c). It can be seen that these have similar properties, peaking near the manufacturer's target wavelength (655 nm), with the intensity being larger when both lasers are used. For comparison we include a spectrum measured when only the infrared laser is on and there is no QD trapped by the Si nanoantenna. This spectrum represents the background. In Fig. 6(d), we show the scatter plots of the tracked centroid locations of a single trapped QD. These data sets are collected with both two beams (trapping and green) and with only the trapping beam switched on. These are obtained with 1000 frames per data set over a time interval of 33 s and processed frame by

Optics EXPRESS

frame using a tracking algorithm [45]. These scatter plots quantify the QD localization by our all-Si nanoantenna tweezers. The corresponding histograms are plotted in Fig. 6(e), obtained with illumination from the trapping laser only [red dots in Fig. 6(d)], i.e., with two-photon-excited fluorescence. The full widths at half maximum (FWHMs) of Gaussian fitting profiles are 128 nm and 347 nm along the *x*- and *y*-axes, respectively. We conclude that the QD is trapped around the gap center, with the distribution including the combined effects of the optical gradient force and steric hindrance from the nanoantenna surface [8]. Our results demonstrate the optical tracking of a single QD trapped by an all-Si nanoantenna with nonlinear absorption, for the first time to our knowledge. In these experiments, because of the large TPA cross-section (σ_{TPA}), QDs can not only be excited via linear absorption from the green excitation laser (at wavelength 532 nm) by absorbing one photon, but also via TPA from the infrared trapping laser (at wavelength 1064 nm) by absorbing two photons simultaneously. We notice however that at the comparatively weak trapping laser irradiation level applied here [31–33] (~ 16.1 mW/μm^2) and taking account of the electric field intensity enhancement produced by our all-Si nanoantenna (~ 5.39×5.39 = 29) [23], the nonlinear refractive index (γI_0, where γ is the nonlinear refractive index coefficient and I_0 is the light intensity) of CdSe is ~ -6.9×10^{-7} (<< n_0 = 2.54). This is extremely small, indicating insignificant modification to optical forces via the optical Kerr effect [42]. We note however that it has been reported that, in conventional optical tweezers with illumination from a femtosecond laser, the TPA process can enhance the trapping of QDs [30]. The use of femtosecond laser pulses with all-dielectric nanoantenna tweezers for the trapping of QDs and other nanomaterials might be an interesting topic for the future study. We also suggest that it may be fruitful to investigate the effect of the electric double layer coating on nanoparticles on trapping with optical nanotweezers, as recent work has shown it to be important with conventional optical tweezers [46].

Optics EXPRESS

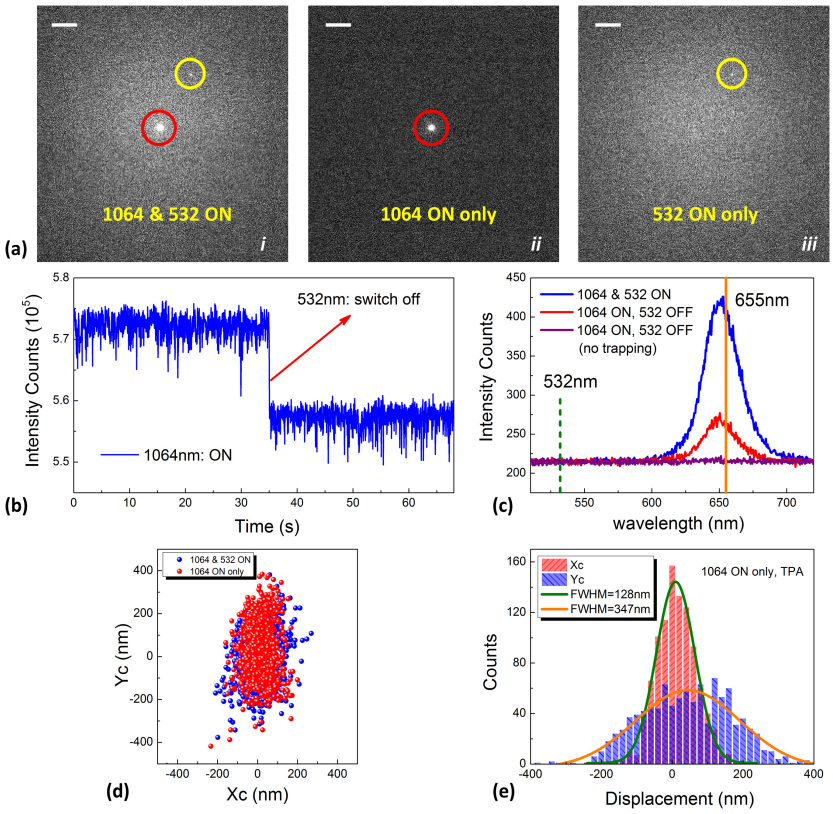

Fig. 6. (a) EM-CCD images of fluorescence showing optical trapping, TPA and linear absorption of QDs. Yellow circles indicate QD stuck to Si surface. Red circles indicate QD being optically trapped by Si nanoantenna. Scale bar: 8 μm. (b) Experimental fluorescence intensity versus time showing the trapping and two-photon excitation of QD. (c) Measured fluorescence emission spectra from QD (spectrometer integration time = 3 s). (d) Scatter plots of center positions of optically trapped QD. Red dots: only infrared laser is on. Blue dots: both green and infrared lasers are on. (e) Position histograms and corresponding Gaussian fits along the *x*- and *y*-directions, extracted from red dots data in panel (d). (Trapping laser intensity I_0 = 16.1 mW/μm^2)

5. Conclusion

In conclusion, we demonstrate that a single streptavidin-coated CdSe/ZnS quantum dot can be optically trapped by an all-Si nanoantenna and excited by the trapping beam via two-photon absorption. Our all-Si nanotweezers yield subwavelength light field confinement and enhancement with generating negligible local heating, which preserves the intrinsic properties of an individual QD and prevents photothermal effects including quenching and bleaching. We perform the tracking observation of the location and light emission of single trapped QDs by our all-Si nanoantenna, for the first time to our knowledge. The fluorescence behavior is visualized by an EM-CCD camera and analyzed with a spectrometer. Numerical simulations are also presented to calculate the optical forces applied to a single QD with the Maxwell stress tensor method. Future work could involve extending this platform by demonstrating the trapping of other nanomaterials such as single biological molecules.

Appendix

Optical trapping of single QDs

Single QDs can be optically trapped by Si nanoantennas via optical forces. In Fig. 7(a), both infrared and green lasers are on for $0 < t < 10$ s. At the beginning ($t = 0$), the QD is trapped by

Optics EXPRESS

an Si nanoantenna. This QD is only trapped for $0 < t < 4$ s and it is no longer trapped when $t > 4$ s. In Fig. 7(b), the green laser is switched on for $0 < t < 25$ s, and a single QD has been trapped at the beginning ($t = 0$). It can be seen from Fig. 7(b) that the QD is released from an Si nanoantenna when the trapping laser is switched off at $t \sim 12$ s. When the trapping laser is switched on again at $t \sim 18$ s, the QD cannot be re-trapped again because it moves far from the nanoantenna hotspots. This behavior is consistent with the short-range nature of the optical forces. In Fig. 7(c), the trapping laser is switched on for $0 < t < 90$ s and switched off thereafter ($t > 90$ s). The green laser is switched on always except for the time interval of 60 s to 80 s. As shown in Fig. 7(c), when the QD moves close to an illuminated Si nanoantenna, it will experience optical forces and can be trapped, resulting in an abrupt jump in fluorescence. At $t \sim 60$ s, the green laser is switched off and the optically trapped QD is excited only by TPA, with the emitted intensity being decreased. Turning the green laser on again at $t \sim 80$ s results in the emitted intensity reverting to the previous level. Switching the trapping laser off at $t \sim 90$ s results in the quick release of the QD from the hotspots. In Fig. 7(d), the trapping laser is switched on for $0 < t < 57$ s and switched off thereafter ($t > 57$ s). The green laser is switched on for $0 < t < 20$ s and $t > 45$ s and switched off for 20 s $< t <$ 45 s. Figure 7(d) shows the similar results as shown in Fig. 7(c), with the optical trapping by optical forces from $0 < t < 57$ s, being released after switching off the trapping laser at $t \sim 57$ s, and being excited by TPA only from the infrared (trapping) laser from 20 s $< t <$ 45 s. The trap-and-release behavior confirms the predominant role of optical forces in the trapping process and that the QD is not attached to Si surface.

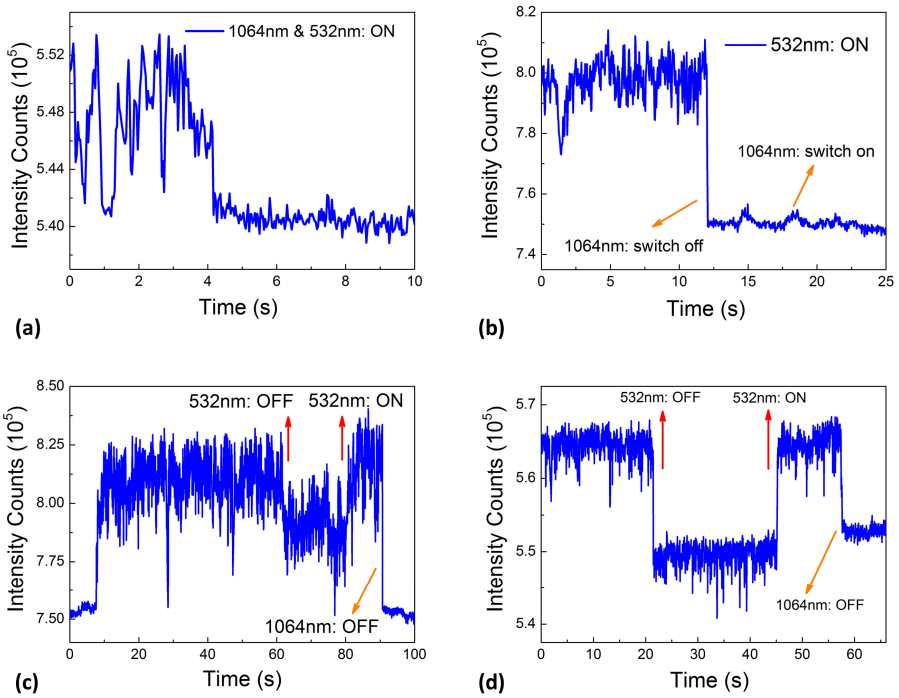

Fig. 7. Fluorescent intensity counts vs. time for trapping of a single QD. (a) $I_0 = 16.1$ mW/μm^2, 30×30 pixel cross section. (b) $I_0 = 17.3$ mW/μm^2, 35×35 pixel cross section. (c) $I_0 = 17$ mW/μm^2, 35×35 pixel cross section. (d) $I_0 = 12.7$ mW/μm^2, 30×30 pixel cross section. For (b)–(d), switching off the trapping laser results in the quick release of the QDs.

Optics EXPRESS

Trapping and sticking of QDs

In Fig. 8, we illustrate an occasion in which a QD is optically trapped by an Si nanoantenna but then becomes stuck to it. At the beginning [Fig. 8(a)], the QD moves randomly. The QD is then optically trapped by the nanoantenna and becomes stuck to Si surface by other forces [Fig. 8(b)]. It remains stuck thereafter [Figs. 8(c) and 8(d)], even after the trapping laser is switched off [Fig. 8(e)]. To illustrate the background level, an EM-CCD frame captured when both the green and infrared (trapping) lasers are switched off is shown as Fig. 8(f).

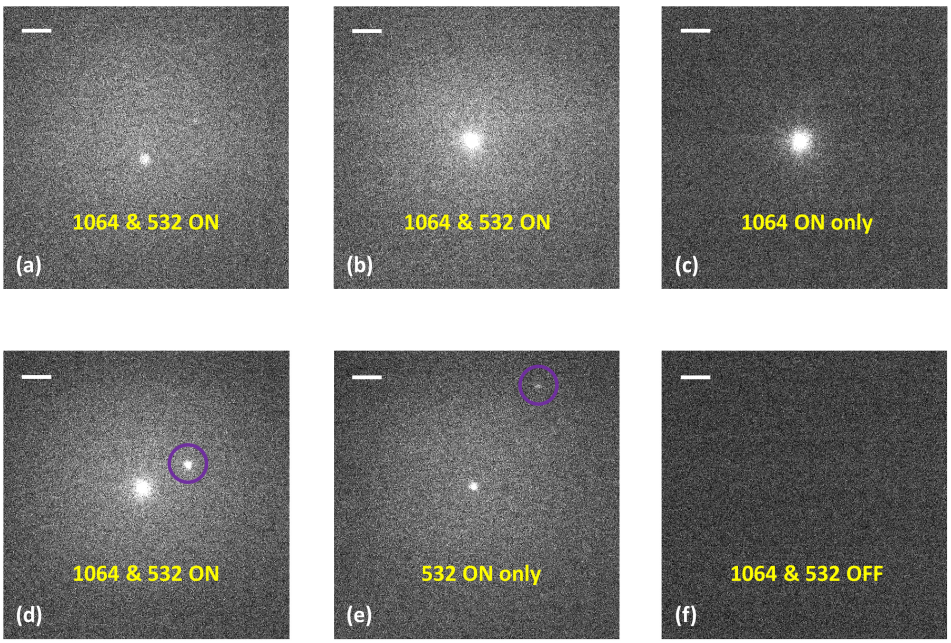

Fig. 8. EM-CCD frames showing optical trapping and sticking of a QD. (a) In this frame, QD is diffusing freely. (b)–(f) QD becomes stuck to Si surface. Purple circles in panels (d) and (e) indicate another suspended QD that moves freely by Brownian diffusion. The intensity of the infrared laser (1064 nm) is decreased in panel (d) [for (a)–(c): I_0 = 17.3 mW/μm^2; for (d): I_0 = 12.7 mW/μm^2]. Images are captured with auto-scaling of contrast, as provided by the EM-CCD camera and software. Scale bar: 8 μm.

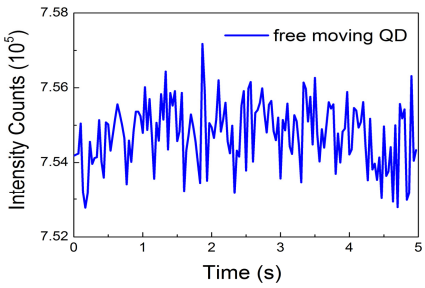

Fig. 9. Tracking of fluorescent emission with green laser only from a single non-trapped free moving QD in solution as a function of time (35×35 pixel cross section).

Funding

Australian Research Council (DP150103736, DP180104141, and FT140100577); Victorian Endowment for Science, Knowledge and Innovation (VESKI); Laby Foundation.

Optics EXPRESS

Acknowledgments

The authors thank Wuzhou Song (School of Materials Science and Engineering, Huazhong University of Science and Technology) for the SEM image and initial discussion.

References

1. S. A. Maier, *Plasmonics: fundamentals and applications* (Springer Science & Business Media, 2007).
2. A. Grigorenko, N. Roberts, M. Dickinson, and Y. Zhang, "Nanometric optical tweezers based on nanostructured substrates," Nat. Photonics **2**(6), 365–370 (2008).
3. M. L. Juan, R. Gordon, Y. Pang, F. Eftekhari, and R. Quidant, "Self-induced back-action optical trapping of dielectric nanoparticles," Nat. Phys. **5**(12), 915–919 (2009).
4. W. Zhang, L. Huang, C. Santschi, and O. J. Martin, "Trapping and sensing 10 nm metal nanoparticles using plasmonic dipole antennas," Nano Lett. **10**(3), 1006–1011 (2010).
5. M. L. Juan, M. Righini, and R. Quidant, "Plasmon nano-optical tweezers," Nat. Photonics **5**(6), 349–356 (2011).
6. K. Wang, E. Schonbrun, P. Steinvurzel, and K. B. Crozier, "Trapping and rotating nanoparticles using a plasmonic nano-tweezer with an integrated heat sink," Nat. Commun. **2**(1), 469 (2011).
7. Y. Pang and R. Gordon, "Optical trapping of 12 nm dielectric spheres using double-nanoholes in a gold film," Nano Lett. **11**(9), 3763–3767 (2011).
8. Z. Xu, W. Song, and K. B. Crozier, "Direct particle tracking observation and Brownian dynamics simulations of a single nanoparticle optically trapped by a plasmonic nanoaperture," ACS Photonics **5**(7), 2850–2859 (2018).
9. A. Ashkin, J. M. Dziedzic, J. E. Bjorkholm, and S. Chu, "Observation of a single-beam gradient force optical trap for dielectric particles," Opt. Lett. **11**(5), 288–290 (1986).
10. D. G. Grier, "A revolution in optical manipulation," Nature **424**(6950), 810–816 (2003).
11. K. C. Neuman and S. M. Block, "Optical trapping," Rev. Sci. Instrum. **75**(9), 2787–2809 (2004).
12. O. M. Maragò, P. H. Jones, P. G. Gucciardi, G. Volpe, and A. C. Ferrari, "Optical trapping and manipulation of nanostructures," Nat. Nanotechnol. **8**(11), 807–819 (2013).
13. S. E. S. Spesyvtseva and K. Dholakia, "Trapping in a material world," ACS Photonics **3**(5), 719–736 (2016).
14. G. Baffou and R. Quidant, "Thermo-plasmonics: using metallic nanostructures as nano-sources of heat," Laser Photonics Rev. **7**(2), 171–187 (2013).
15. K. Wang and K. B. Crozier, "Plasmonic trapping with a gold nanopillar," ChemPhysChem **13**(11), 2639–2648 (2012).
16. K. Svoboda and S. M. Block, "Biological applications of optical forces," Annu. Rev. Biophys. Biomol. Struct. **23**(1), 247–285 (1994).
17. A. E. Krasnok, A. E. Miroshnichenko, P. A. Belov, and Y. S. Kivshar, "All-dielectric optical nanoantennas," Opt. Express **20**(18), 20599–20604 (2012).
18. R. M. Bakker, D. Permyakov, Y. F. Yu, D. Markovich, R. Paniagua-Domínguez, L. Gonzaga, A. Samusev, Y. Kivshar, B. Luk'yanchuk, and A. I. Kuznetsov, "Magnetic and electric hotspots with silicon nanodimers," Nano Lett. **15**(3), 2137–2142 (2015).
19. M. Caldarola, P. Albella, E. Cortés, M. Rahmani, T. Roschuk, G. Grinblat, R. F. Oulton, A. V. Bragas, and S. A. Maier, "Non-plasmonic nanoantennas for surface enhanced spectroscopies with ultra-low heat conversion," Nat. Commun. **6**(1), 7915 (2015).
20. A. I. Kuznetsov, A. E. Miroshnichenko, M. L. Brongersma, Y. S. Kivshar, and B. Luk'yanchuk, "Optically resonant dielectric nanostructures," Science **354**(6314), aag2472 (2016).
21. R. Regmi, J. Berthelot, P. M. Winkler, M. Mivelle, J. Proust, F. Bedu, I. Ozerov, T. Begou, J. Lumeau, H. Rigneault, M. F. García-Parajó, S. Bidault, J. Wenger, and N. Bonod, "All-dielectric silicon nanogap antennas to enhance the fluorescence of single molecules," Nano Lett. **16**(8), 5143–5151 (2016).
22. Z. Xu, W. Song, and K. B. Crozier, "Direct observation of optical trapping of a single quantum dot with an all-silicon nanoantenna," in *Frontiers in Optics* (Optical Society of America, 2017), paper FM3B. 2.
23. Z. Xu, W. Song, and K. B. Crozier, "Optical Trapping of Nanoparticles Using All-Silicon Nanoantennas," ACS Photonics **5**(12), 4993–5001 (2018).
24. X. Michalet, F. Pinaud, T. D. Lacoste, M. Dahan, M. P. Bruchez, A. P. Alivisatos, and S. Weiss, "Properties of fluorescent semiconductor nanocrystals and their application to biological labeling," Single Mol. **2**(4), 261–276 (2001).
25. D. Bera, L. Qian, T. K. Tseng, and P. H. Holloway, "Quantum dots and their multimodal applications: a review," Materials (Basel) **3**(4), 2260–2345 (2010).
26. U. Resch-Genger, M. Grabolle, S. Cavaliere-Jaricot, R. Nitschke, and T. Nann, "Quantum dots versus organic dyes as fluorescent labels," Nat. Methods **5**(9), 763–775 (2008).
27. P. M. Bendix, L. Jauffred, K. Norregaard, and L. B. Oddershede, "Optical trapping of nanoparticles and quantum dots," IEEE J. Sel. Top. Quantum Electron. **20**(3), 15–26 (2014).
28. T. Iida and H. Ishihara, "Theoretical study of the optical manipulation of semiconductor nanoparticles under an excitonic resonance condition," Phys. Rev. Lett. **90**(5), 057403 (2003).
29. L. Pan, A. Ishikawa, and N. Tamai, "Detection of optical trapping of CdTe quantum dots by two-photon-induced luminescence," Phys. Rev. B Condens. Matter Mater. Phys. **75**(16), 161305 (2007).

Optics EXPRESS

30. W. Y. Chiang, T. Okuhata, A. Usman, N. Tamai, and H. Masuhara, "Efficient optical trapping of CdTe quantum dots by femtosecond laser pulses," J. Phys. Chem. B **118**(49), 14010–14016 (2014).
31. L. Jauffred, A. C. Richardson, and L. B. Oddershede, "Three-dimensional optical control of individual quantum dots," Nano Lett. **8**(10), 3376–3380 (2008).
32. L. Jauffred and L. B. Oddershede, "Two-photon quantum dot excitation during optical trapping," Nano Lett. **10**(5), 1927–1930 (2010).
33. L. Jauffred, A. Kyrsting, E. C. Arnspang, S. N. S. Reihani, and L. B. Oddershede, "Sub-diffraction positioning of a two-photon excited and optically trapped quantum dot," Nanoscale **6**(12), 6997–7003 (2014).
34. Y. F. Chen, X. Serey, R. Sarkar, P. Chen, and D. Erickson, "Controlled photonic manipulation of proteins and other nanomaterials," Nano Lett. **12**(3), 1633–1637 (2012).
35. A. Zehtabi-Oskuie, H. Jiang, B. R. Cyr, D. W. Rennehan, A. A. Al-Balushi, and R. Gordon, "Double nanohole optical trapping: dynamics and protein-antibody co-trapping," Lab Chip **13**(13), 2563–2568 (2013).
36. R. A. Jensen, I. C. Huang, O. Chen, J. T. Choy, T. S. Bischof, M. Lončar, and M. G. Bawendi, "Optical trapping and two-photon excitation of colloidal quantum dots using bowtie apertures," ACS Photonics **3**(3), 423–427 (2016).
37. Y. Tsuboi, T. Shoji, N. Kitamura, M. Takase, K. Murakoshi, Y. Mizumoto, and H. Ishihara, "Optical trapping of quantum dots based on gap-mode-excitation of localized surface plasmon," J. Phys. Chem. Lett. **1**(15), 2327–2333 (2010).
38. C. T. Yuan, P. Yu, H. C. Ko, J. Huang, and J. Tang, "Antibunching single-photon emission and blinking suppression of CdSe/ZnS quantum dots," ACS Nano **3**(10), 3051–3056 (2009).
39. S. Dey and J. Zhao, "Plasmonic Effect on Exciton and Multiexciton Emission of Single Quantum Dots," J. Phys. Chem. Lett. **7**(15), 2921–2929 (2016).
40. J. S. Donner, G. Baffou, D. McCloskey, and R. Quidant, "Plasmon-assisted optofluidics," ACS Nano **5**(7), 5457–5462 (2011).
41. M. Ploschner, M. Mazilu, T. F. Krauss, and K. Dholakia, "Optical forces near a nanoantenna," J. Nanophotonics **4**(1), 041570 (2010).
42. L. Novotny and B. Hecht, *Principles of Nano-Optics* (Cambridge University Press, 2012).
43. T. F. Scientific, "Qdot Streptavidin Conjugates," https://tools.thermofisher.com/content/sfs/manuals/mp19000.pdf.
44. R. L. Sutherland, *Handbook of nonlinear optics* (CRC Press, 2003).
45. R. Parthasarathy, "Rapid, accurate particle tracking by calculation of radial symmetry centers," Nat. Methods **9**(7), 724–726 (2012).
46. P. Rodríguez-Sevilla, K. Prorok, A. Bednarkiewicz, M. I. Marqués, A. García-Martín, J. García Solé, P. Haro-González, and D. Jaque, "Optical forces at the nanoscale: size and electrostatic effects," Nano Lett. **18**(1), 602–609 (2018).

CHAPTER 6

Summary and future work

6.1 Summary of results

In this dissertation, we focus on the direct observation of optical trapping and tracking of single nanoparticles using two different nanostructures, that is, a double nanohole (DNH) aperture in a gold film, and an all-dielectric (silicon) nanoantenna on a silicon substrate. Due to the high thermal conductivity of the materials employed (i.e., Au and Si) and the heat sink functionality (i.e., via Au film for DNH device and via Si substrate for Si nanoantenna), both nanostructures exhibit only modest localized heating. Optical forces acting on nanoparticles are determined from the rigorous Maxwell stress tensor method. Our results quantify the one-to-one interactions between single nanoparticles and single nanostructures.

In the first experiment (Chapter 3), we employ fluorescence microscopy to track the position of a single trapped polystyrene nanosphere with a diameter of 20 nm in the vicinity of a plasmonic DNH aperture. We furthermore perform Langevin equation simulations to model the trapped nanoparticle trajectories under the influence of the relevant forces, including the Stokes drag force, gravity force with buoyancy, optical trapping force and Brownian force (stochastic). This combination of experiments and simulations provides a powerful means for the better understanding of the fundamental mechanism that governs trapping behaviour in nanostructure-based optical tweezers. In the second experiment (Chapter 4), we experimentally demonstrate the optical trapping and transport of polystyrene nanospheres with diameters of 20 nm and 100 nm using a non-plasmonic all-dielectric (Si) nanoantenna. We observe that multiple nanoparticles

can be simultaneously trapped by a single all-Si nanoantenna. We also show that fluorescent emission from a single trapped NS can be excited via two-photon absorption with the CW infrared trapping laser. This work represents the first experimental realization of optical trapping using all-dielectric nanoantennas. With the ultralow heat generation in our Si nanoantennas, a number of interesting possibilities exist for extending trapping works. In the last experiment (Chapter 5), the optical trapping and direct tracking of a single streptavidin-coated CdSe/ZnS quantum dot using all-Si nanoantennas are successfully demonstrated. We also show that single trapped QDs can be excited by two-photon absorption from the same trapping laser at relatively low input power due to near-field enhancement. This work presents an example of all-dielectric nanotweezers for achieving optical trapping and manipulation of nanomaterials for biosensing.

6.2 Suggestions for future work

The following are some suggestions for future research on the optical trapping of nanoparticles. These represent open and unsolved problems.

Brownian motion simulations: In our Brownian dynamics simulations, due to the very short solver time step, our theoretical modelling predicts nanoparticle trajectories over time intervals of 100 μs or shorter. Such a simulation (of 100 μs) however takes three days to carry out on a standard desktop computer at the time of writing. Ideally, future work would extend the modelling time interval to be ~ tens of seconds, would enable direct comparison with experiment data. In addition, it would be ideal to include additional forces and interactions to accurately describe the trapped nanoparticle

dynamics in the water flow, for example, van der Waals forces, thermophoretic forces, electric double layer forces, fluid-particle interactions, and particle-particle interactions.

Optical trapping and manipulation of nanomaterials for sensing: Our results demonstrate that Si nanoantennas are robust as optical nanotweezers for the trapping of nanoparticles with negligible local heating. It would be interesting to develop other sorts of dielectric nanotweezers (and not just silicon) for the optical trapping and manipulation (e.g., rotation) of various nanomaterials, such as molecules, DNA, nanodiamonds (with nitrogen-vacancy centres), silk-coated nanoparticles, semiconductor nanowires, upconverting fluorescent nanoparticles and chiral nanoparticles. Furthermore, all-dielectric nanoantennas used with picosecond or femtosecond pulsed lasers and applied alternating current (AC) or direct current (DC) electric fields may provide other interesting phenomena.

In the experiments, we trap single QDs using a Si nanoantenna for several minutes. Our experiments record the blinking process of the QDs. However, it would also be interesting to measure other QD properties at the single QD level, such as fluorescence lifetime and quantum yield. Moreover, using fluorescence microscopy, we track particle centre locations in *x*- and *y*-axes. In the future, we can use other techniques to observe the vertical positions of trapped nanoparticles along the *z*-axis.

All-dielectric nanoantennas can feature strong magnetic field resonant modes ("magnetic hotspots"), excited by appropriate choice of the polarization of the incident light. It may be interesting to consider whether nanoparticles with magnetic dipole (MD) resonances could be optically trapped in these magnetic field hotspots. This might have applications in particle sorting, for example.

With the significantly reduced local heating behaviour, all-dielectric nanoantennas are very suitable for the trapping of single molecules for biological sensing, where small thermal changes are critical. I have done some preliminary experiments on the optical trapping of fluorescent proteins using our all-Si nanoantennas (Figure 6.1). Due to the weak fluorescence and very small size, I find it is difficult to directly observe a single Alexa Fluor 594-labeled streptavidin (Life Technologies, S32356, average molecular weight ~ 60 kDa) through fluorescence microscopy. The proteins are suspended in a 1:1 glycerol/PBS buffer (1X, pH 7.4) mix with Tween 20 added (0.1% v/v) with a final concentration of ~ 20 ng/μL. EM-CCD camera however can detect the trapping process from the step-like increase of the fluorescence signal. My future work will extend this direction for the direct observation of optical trapping of a single molecule (maybe for large proteins), although it presents a big challenge. As shown in Figure 6.1a–c, single proteins are trapped by all-silicon nanoantennas, resulting in the step-like increases in fluorescence. Switching the trapping laser off in Figure 6.1a,b results in the quick release of proteins. In Figure 6.1d, we also include another example with both infrared and green lasers on and there is no protein trapped.

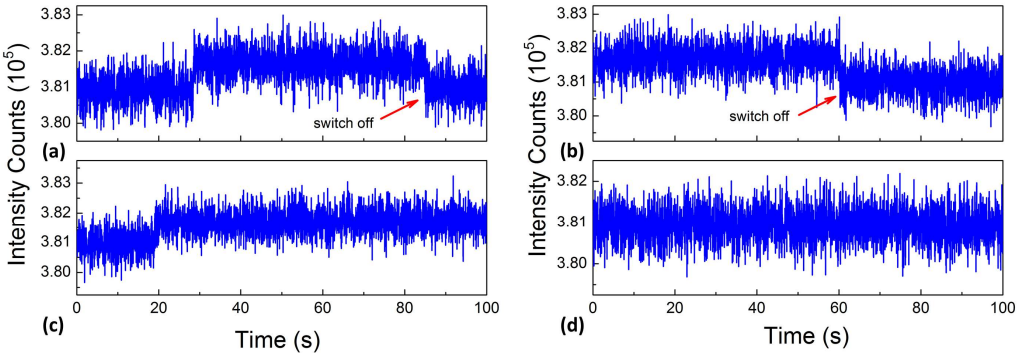

Figure 6.1. Optical trapping of single proteins (Alexa Fluor 594-labeled streptavidin, Life Technologies) as sudden discrete jumps in fluorescence counts (I_0 = 12 mW/μm^2, 25×25 pixel cross section). Red arrow: trapping laser is switched off.

Optical forces determination at the nanoscale: More recently, based on the investigation with conventional optical tweezers, it has been suggested that the electric double layer (EDL) coating and zeta potential of nanoparticles (for sub-100 nm) may play an important role in determining their optical trapping behaviour.[1, 2] As such, understanding the generation of optical forces at the nanoscale is not only important for the complete description of the optical trapping mechanism but is highly attractive for a wide range of subjects. On the basis of our trapping results as well as numerical calculations, optical trapping of NPs is observed even when the trapping energy is smaller than the thermal energy. To have a better understanding of the trapping process of conventional and near-field optical tweezers in a complete fashion, it may be interesting to develop a deeper understanding of the effect of the EDL and zeta potential upon the optical forces exerted on nanoparticles.

References

1. Rodríguez-Rodríguez, H.; Rodriguez Sevilla, P.; Martin Rodriguez, E.; Ortgies, D. H.; Pedroni, M.; Speghini, A.; Bettinelli, M.; Jaque, D.; Haro-González, P. Enhancing Optical Forces on Fluorescent Up-Converting Nanoparticles by Surface Charge Tailoring. *Small* 2015, 11, 1555-1561.

2. Rodríguez-Sevilla, P.; Prorok, K.; Bednarkiewicz, A.; Marqués, M. I.; García-Martín, A.; García Solé, J.; Haro-González, P.; Jaque, D. Optical forces at the nanoscale: size and electrostatic effects. *Nano Letters* 2017, 18, 602-609.